Carbon Nanotube Microarchitectures for Mechanical Metamaterials

by

Sei Jin Park

A dissertation submitted in partial fulfillment
of the requirements for the degree of
Doctor of Philosophy
(Mechanical Engineering)
in The University of Michigan
2014

Doctoral Committee:

Associate Professor A. John Hart, Co-Chair, Massachusetts Institute of Technology
Professor Wei Lu, Co-Chair
Assistant Professor Xiaogan Liang
Professor Anthony M. Waas

DEDICATION

to

Joyful smile,

Unwavering character,

Life, youthfulness,

Love, peace and happiness,

I dedicate this thesis

And myself.

ACKNOWLEDGEMENTS

I arrived in Ann Arbor in the fall of 2005 as a naïve college freshman. Nine years later, I bid goodbye as a Doctor of Mechanical Engineering. So much has happened in that duration, and I am truly thankful for all the experiences that have led to this academic milestone.

I would like to express my respect and deepest gratitude to my advisor Professor John Hart. It has been a great honor and privilege working with him. Without his guidance, I would not have dreamed of achieving a doctoral degree. His enthusiasm, insight, and drive are truly exceptional and have inspired me to become a better researcher. One of John's admirable qualities as an advisor is that he always made time for his students despite his busy schedule. His devotion to his students is a testament to his mentorship and passion for training future scientists.

I extend my appreciation to my doctoral committee members Professor Wei Lu, Professor Anthony Waas, and Professor Xiaogan Liang for their time and continuous support. They have offered invaluable advice throughout my graduate career. I've also had the privilege of working with them on projects that had a large impact on my thesis work.

I would also like to acknowledge collaborators I have worked with during my Ph.D. career. In no particular order, I would like to thank:

Dr. Michael De Volder (IMEC), Anna Brieland-Shoultz, Dr. Sameh Tawfick, Dr. Mostafa Bedewy, Dr. Matthew Maschmann (AFRL), Dr. Jeffery Baur (AFRL), Dr. Julien Meaud, Dr. Trisha Sain, Dr. Bongjun Yeom, Professor Gregory Hulbert, Professor Ellen Arruda, Professor Nicholas Kotov, Dr. Zheng-Dong Ma, Adam Paxson (MIT), Professor Kripa Varanasi (MIT), and Dr. Jong G. Ok for conducting research with me; and Dr. Eric Meshot, Dr. Erik Polsen, Dr. Davor Copic, Dr. Daniel McNerny,

Keqin Cao, Dr. Sanha Kim (MIT), Hangbo Zhao (MIT), and Christine Jacob (MIT) for training me on various software, equipment, and helping out with experiments.

I have spent many hours at fabrication and characterization facilities, such as Lurie Nanofabrication Facility (LNF), Electron Microscopy Analysis Lab (EMAL), Center for Material Science and Engineering (CMSE, MIT) and Institute for Soldier Nanotechnology (ISN, MIT), and I would like to express my appreciation for the staff members who maintain these facilities.

I would also like to recognize the financial sponsors that have enabled the research presented in this thesis. National Science Foundation (NSF), Defense Advanced Research Project Agency (DARPA), and Air Force Office of Scientific Research (AFOSR) have generously supported this work through various grants. I would like to also thank University of Michigan Department of Mechanical Engineering for a departmental fellowship and Rackham Graduate School for travel support.

To my fellow Mechanosynthesizers, thank you for facilitating a creative, enthusiastic, friendly, and constructive research environment and for challenging me to become a better researcher.

To my friends who have crossed paths with me during my stay, I will always treasure the moments we have shared, and I will miss you dearly and sorely…

And finally, I am most grateful to my family, whose unconditional love and support have enabled me to see this through.

TABLE OF CONTENTS

LIST OF TABLES

LIST OF FIGURES

ABSTRACT

Metamaterials use ordered internal structure, typically at the micro- and nanoscales, to exhibit properties uncommon or nonexistent in natural materials. To design a metamaterial with target performance, hierarchical specification of geometry and properties of the constituent elements is essential. Vertically aligned growth of carbon nanotubes (CNTs) is a potentially attractive means to achieve such control because it is a scalable fabrication technique that can produce bulk thick films and patterned microstructures over a large area. CNTs also possess attractive properties such as high stiffness, strength, and electrical and thermal conductivities at low mass density. Therefore, the motivation of this dissertation is to create new methods to manipulate CNT growth and modification at the nano- and microscales, toward the realization of scalable CNT mechanical metamaterials.

First, it is shown that CNT microstructures having complex three-dimensional (3-D) shapes can be manufactured by controlling the CNT growth rate locally within each microstructure using a growth retardant layer patterned underneath the CNT growth catalyst film. Microstructures with trajectories in-plane and out-of-plane are achieved by understanding the mechanical coupling among CNTs and designing the catalyst and offset patterns accordingly. The geometry of the strain-engineered microstructures is predicted using both an analytical model and the finite element method.

Next, it is shown that the mechanics of CNT microstructures can be tuned by conformal coating at the nanoscale, via atomic layer deposition (ALD) of Al_2O_3. Using vertical cylindrical CNT micropillars, a stiffness tuning from 7 MPa to 50 GPa (almost 4 orders of magnitude) is demonstrated. The coating thickness also changes the dominant deformation behavior of the CNT microstructures, from buckling to brittle fracture. In the buckling regime, the coated CNT forests can withstand and fully recover compressive strain of up to 75%.

Last, fabrication methods are developed toward application of the 3-D CNT microarchitectures. ALD coating, polymer infiltration, and lamination are used to fabricate a CNT microtruss nanocomposite laminate having simultaneously high stiffness and damping. Then, microstructure arrays with geometry mimicking the scales of a butterfly wing are fabricated and determined to exhibit superhydrophobic and directional wetting behaviors. Further work on 3-D CNT microarchitectures with engineered geometry, mechanics, and surface functionality may realize multifunctional materials with targeted combinations of mechanical, electrical, thermal, and/or optical properties.

CHAPTER 1

INTRODUCTION

1.1 Motivation

Controlling structures at the microscale is gaining increasing importance, not only for efficient placement of constituent materials to achieve a greater degree of property tuning [1], but also due to unique and unconventional properties arising from such ordered micro- and nanostructures [2]. The microscale structural manipulation has a long history; blacksmiths were introducing anisotropic nanostructures to forged steels as early as the 3rd century to improve their toughness, resilience and sharpness, namely the Damascus steel [3].

Materials with deliberately controlled microscale structures have been fabricated out of many materials, such as silicon [4, 5], metals [6] and polymers [7] using a multitude of fabrication techniques. These fabrication techniques include stacking of two-dimensional (2-D) layers [8], angled exposure [9], interference lithography [10], direct write lithography [11] and self-assembly [12]. These techniques either suffer from lack of spatial structural variability (angled exposure, interference lithography), dimensional control of defects (self-assembly), or low throughput (stacking of 2-D layers, direct write lithography), as well as limitations in tuning the properties of the final structures as the processes are only suited to certain classes of materials.

Bottom-up fabrication approaches have a potential to create a spatially varied three-dimensional (3-D) microstructure arrays in a single step if the growth, assembly, or deposition rates of the structures can be controlled locally, both within individual structures, and between different structures. Carbon nanotubes (CNTs) are an attractive system for this concept as CNTs have many unique properties, such as high stiffness, electrical and thermal conductivities at low mass densities. CNTs can be grown to create

arrays of high aspect ratio vertically aligned CNT (VACNT) structures using only a single lithography step that patterns the catalyst layer [13, 14]. However, the resulting array is a simple extrusion of the catalyst patterns, with straight trajectories. Post processing techniques using capillary forces have been developed to create variations in the third dimension in the arrays of CNT microstructures [15], however, the resultant shapes are limited by catalyst pattern design, capillary bridges between structures, or between structure and substrate, and the array is limited in the volume fraction as the structures shrink during forming.

1.2 Thesis scope

This dissertation presents **a novel method to produce 3-D microarchitectures by modifying vertically aligned growth of CNT microstructures, with tuning of the mechanics via conformal coating to produce multifunctional mechanical metamaterials.** To achieve this goal, a novel catalyst stack to control the growth rates of CNTs is developed and the CNT growth is characterized and modeled on this catalyst stack. The tuning of mechanics is achieved using a conformal coating via atomic layer deposition (ALD) of Al_2O_3. Then integration of the novel 3-D CNT microarchitectures into multifunctional composite materials is demonstrated. Finally the outlook and possibility of scaling down to nanoscale architectures is discussed.

The advances presented in this thesis can be categorized into three axes of pursuits (Figure 1.1):

1. Architecture – The microarchitectures enabled by rate modulated growth of CNT microstructures is demonstrated. A portfolio of characterizations of the resulting CNT forests is presented. Then an analytical model and a 3-D finite element methods (FEM) model are developed to predict the effect of process parameters on the resulting microstructure geometry. Lastly, a possibility of scaling down to nanoarchitecture regime is considered.
2. Mechanics – While preserving the architecture, the stiffness and deformation behavior of CNT microstructures are tuned via a conformal coating of Al_2O_3 by ALD. Stiffness and deformation behavior characterizations are performed

on CNT microstructures reinforced with Al_2O_3 and the mechanics tuning achieved is related to the observed coated CNT morphology.

3. Multifunctionality – The 3-D CNT microarchitectures whose structures and properties are demonstrated to be tunable are incorporated in multifunctional materials. Two applications are presented; a simultaneously high stiffness and damping composite materials for blast load dissipation, and a simultaneously superhydrophobic and directionally wetting surface mimicking butterfly scales for directed droplet rolling.

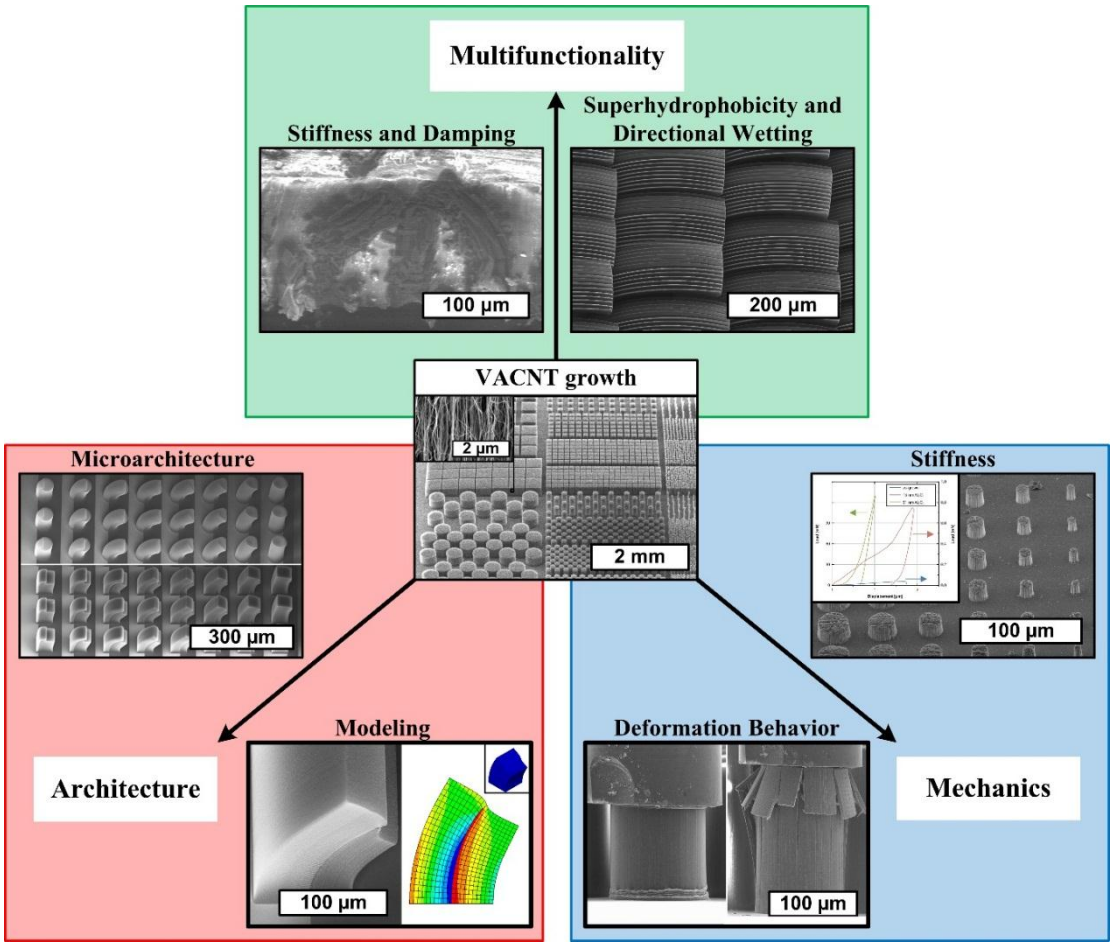

Figure 1.1 Three axes of pursuits presented in this dissertation: 1. Architecture, 2. Mechanics, and 3. Multifunctionality.

1.3 Thesis outline

This dissertation is presented in the following organization:

Chapter 2 presents a background on material manipulation at the microscale. The state-of-the-art techniques for fabricating microarchitectures are overviewed and classified according to their principles. It presents a comparison of identified classes of microfabrication methods and notes the currently available design space for microarchitectures and emphasizes the need for a scalable complex 3-D microarchitecture manufacturing technique.

Chapter 3 presents the strain-engineered 3-D CNT microarchitectures. A novel catalyst stack is introduced to control the growth rate locally within microstructures and globally across microstructures. A comprehensive characterization of the resulting CNT forests on catalyst stacks and a library of complex microstructures fabricated are presented.

Chapter 4 presents simulations of the strain-engineered growth of CNT microarchitectures. A 2-D analytical model as well as a 3-D finite element method (FEM) model are developed to understand the mechanical coupling of segments that grow at different rates, and simulate the effects of process parameters on the resulting microstructure geometry.

Chapter 5 presents a method for tuning the mechanics of CNT microstructures via conformal coating method while preserving the shape of the microstructures. A large range of stiffness tuning is achieved and the deformation behavior change from buckling to brittle fracture is related to the thickness of the conformal coating.

Chapter 6 presents a demonstration of 3-D CNT microarchitecture application in simultaneously high stiffness and damping composite material. A process for integration of 3-D CNT microarchitectures into polymer embedded hard/soft phase composite material is developed. The composite material is tested for stiffness and damping capacity and compared to state-of-the-art materials on the stiffness-damping map.

Chapter 7 presents a demonstration of 3-D CNT microarchitecture application in simultaneously superhydrophobic and directionally wetting surface. The structural similarity to actual butterfly scales is noted and the superhydrophobicity and directional wetting is demonstrated by measuring the contact angle hysteresis.

Chapter 8 presents a summary of the contributions of this dissertation and outlook toward future advances, hoping that impactful technological transition would occur that harness the properties of the micro- and nanoarchitectured materials.

CHAPTER 2

ARCHITECTURE AT THE MICROSCALE

This chapter overviews the importance of precise manipulation of matter at small scales for the purposes of building metamaterials, and defines the term ‘microarchitecture’. Then principles of shaping operations are introduced and microfabrication methods are classified according to their principles. Next, Carbon Nanotube (CNT) microstructure growth by Chemical Vapor Deposition (CVD) as a microfabrication method is described. Finally, a microstructure classification by their geometrical complexities is introduced and traits of microfabrication classes are compared to highlight presently available design space for microarchitectures and emphasize the need for a scalable complex microarchitecture fabrication technique.

2.1 Background

2.1.1 Metamaterials

One of the advances that Nanotechnology has brought on is the development of metamaterials. Metamaterials are artificially structured materials engineered to have properties that are not found in nature. The idea of engineering the properties by careful manipulation of structures was first introduced in the field of electromagnetic waves [16-18], and later expanded to mechanical waves [19], demonstrating examples such as phononic crystals [20-23], sonic crystals [24], thermal diodes [25], ultrasonic lenses [26] and broadband acoustic cloaks [27]. The concept has further expanded and generalized to include tuning of a wide range of properties by engineering the structure of the materials [2], such as negative Poisson’s ratio (auxetic) materials [28], superhydrophobic surfaces [29] and self-repairing slippery surfaces [30]. Recently, a hybrid metamaterial operating in both optical and mechanical realm was reported [31].

The key to the performance of metamaterials is their precisely defined structures and hence their production requires material manipulation techniques that can create the engineered structure with high precision.

These developments were enabled by a rapidly expanding portfolio of techniques available to manipulate matters at very small scales. Processes are being developed to manipulate wider range of materials, into larger range of feature sizes with more and more precise control over the geometry and placement. From here the notion of microarchitecture arises; in order to create metamaterials, one should not stop short at building microstructures, but needs to architect the microscopic scenery with deliberate design.

2.1.2 Microstructure, microarchitecture and surface

The definitions of the terms microstructure [2], microarchitecture [1] and surface [32] are vague in literature, and the terms are often used broadly and sometimes interchangeably. Therefore, it will be helpful to clearly define and distinguish these terms, in order to eliminate confusion over terminology. The distinction between the terms primarily lie in their relative scales. Let us examine a simple macroscopic example. A building by itself can be referred to as a 'structure' (Figure 2.1a), whereas a city which contains many buildings of various height, shape and sizes can be referred to as an 'architecture' (Figure 2.1b). When we take another step back and look at an even larger area, for instance an entire nation, the features of buildings and architectures will look miniscule, and one might refer to a large area containing a multitude of architectures and structures a 'surface' (Figure 2.1c) of the earth.

Architecture is the product and the practice of shaping a space with functional considerations. This includes careful design and placement of structures as well as the open areas. The key notion is that deliberate design and construction of structures (with unified overall goal) make up architectures. The term 'surface' is used in the context of much larger perspective compared to 'structure' and 'architecture', and refers to a relatively very large area which contains many structures and architectures.

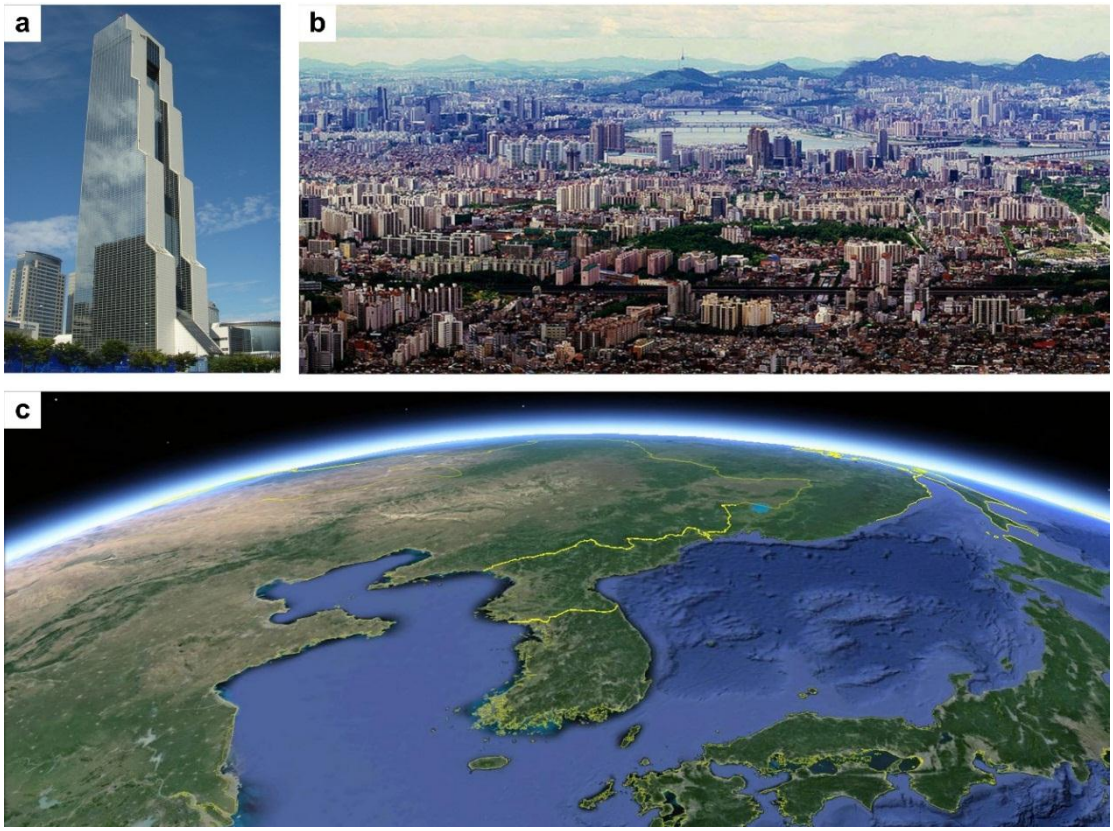

Figure 2.1 Proposed distinction between structure, architecture and surface: a) Trade Tower in Seoul, Korea as an example ‘structure’, b) a panoramic view of Seoul, Korea[1] as an example ‘architecture’, and c) a satellite view of Korea[2] as an example ‘surface’.

Inspired by this example, the definitions of ‘microstructure’, ‘microarchitecture’ and ‘surface’ are proposed as follows:

> Microstructure – A microstructure is an individual structure with its dimensions in the micrometer range.
>
> Microarchitecture – A group of microstructures that are precisely defined and placed relative to each other (usually to imbue collective functions/properties that differ from simple sums of those of individual microstructures).
>
> Surface – A very large area containing multitude of microarchitectures. The collective properties of microarchitectures are preserved. Depending on the homogeneity and placement of the microstructures and microarchitectures, the surface property may vary spatially.

[1] Image adapted from: http://blog.daum.net/pillaree/30, Accessed in 2014

[2] Image adapted from: Google Earth (2013) Version 7.1.2.2041, Accessed in 2014

2.2 Architecting methods

2.2.1 Principles of shaping operations

Shaping is an act of realizing a deliberate distribution of materials in a given space. There are two intuitive methods of shaping. One way is to start with a big block of the material and remove unwanted parts (for example, a sculpture), and another way is to start with nothing and pile up the material until the desired shape is achieved (for example, a snowman). The former approach is called ‘Removal’ while the latter is called ‘Addition’.

Further, there are more complex ways of achieving desired shape with a material, such as starting with the desired material in a different shape, then moving the material around until the desired shape is achieved (for example, glass blowing), and starting with another material in the desired shape and changing the material into the desired material (for example, pottery). The former method will be referred to as ‘Transformation’ and the latter as ‘Conversion’. These methods offer unique advantages over the previously discussed methods, as Transformation reduces wasted material and Conversion enables fabrication of structures consisting of materials that are hard to shape otherwise.

Finally, perhaps the most counterintuitive method for shaping, is ‘Growth’. This method relies on chemical/biological processes to create desired material from raw materials. A ‘seed’ is needed to convert the raw materials and the target material is added as it is being produced. The created material can be added in a preferential direction, allowing opportunities for shaping. An example of this is shrubs or trees planted in a perimeter to serve as walls when they grow.

Then, there are combinations of the aforementioned 5 methods. For instance, building a pyramid involves first carving the stones into blocks (Removal) and then piling them up to achieve desired height (Addition), then finally carving out the unwanted parts to smooth out the outer surfaces (Removal). In pottery, the clay is first shaped (Transformation), then fired to become ceramic (Conversion). Bonsai trees are potted (Growth) and pruned (Removal) for aesthetic pleasure.

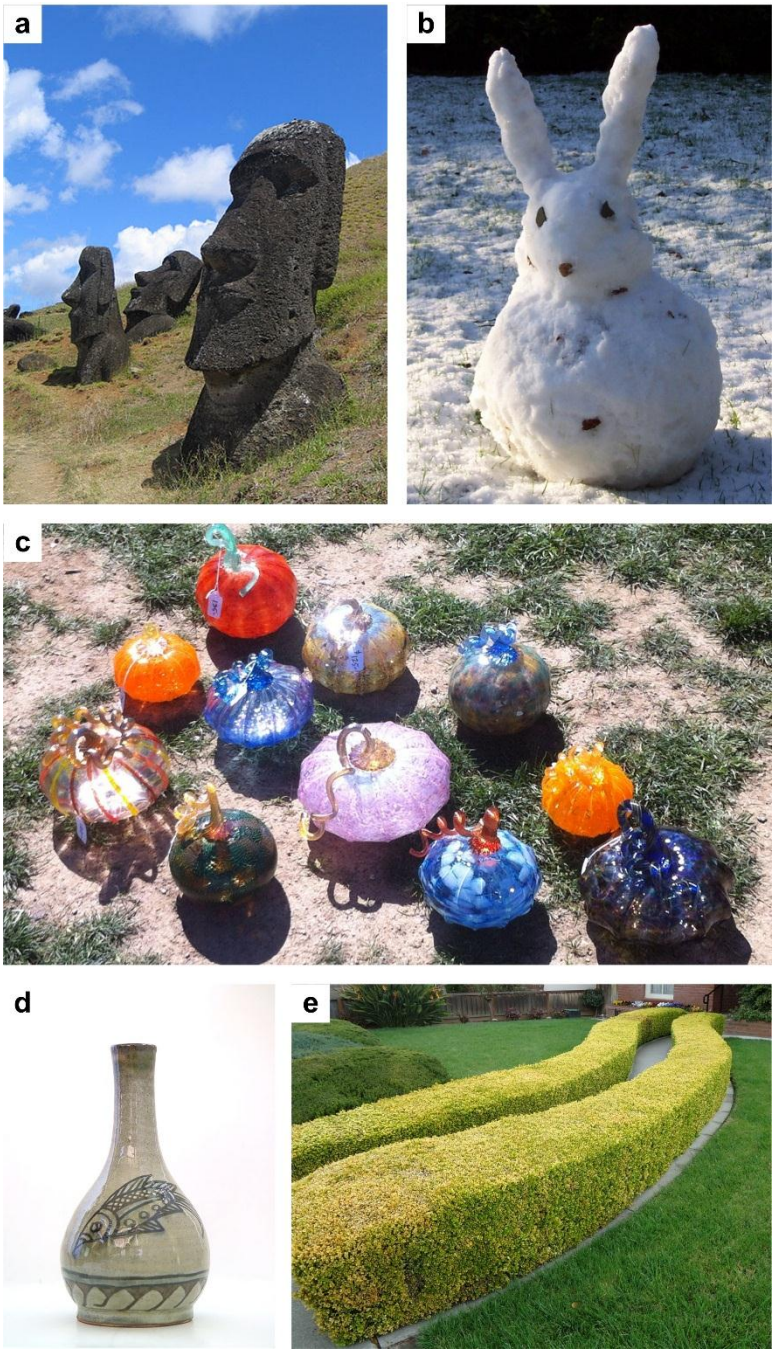

Figure 2.2 Example structures for each shaping principle: a) Moai sculptures (Removal), b) a snow rabbit (Addition), c) glass pumpkins (Transformation), d) pottery (Conversion), and e) hedges (Growth).

2.2.2 Microfabrication methods

With the advent of nanotechnology, the desired structural size has gone down in scale into nanometer and micrometer regime, and hence new shaping methods have been developed to deal with these sizes; these are called microfabrication methods. However, the principles behind these methods remain the same. Various microfabrication techniques exist today, and hybridization of the principles is common to achieve resolution and control needed to create microarchitectures of ever increasing complexity.

A few example microfabrication techniques for each principle are listed and representative architectures are shown in Figure 2.3.

Romoval – Angled reactive ion etching (RIE) has been used to remove material in a woodpile pattern to create three-dimensional (3-D) photonic crystals out of silicon [33]. Metal-assisted chemical etching (MACE) has been used to create angled arrays of silicon nanowires [34].

Addition – Glancing angle deposition (GAD) has been used to deposit nanowires that are vertical, angled, or helical [35]. Gold nanohelices were fabricated by electroplating using a template created by direct laser writing (DLW) [36] and 3-D nickel microlattices was produced by electroless nickel plating using a self-propagating photopolymer waveguide (SPPW) [6].

Transformation – Directed mechanical deformation and elastocapillary densification have been used to transform silicon nanowires [37], polymer microstructures [38-40] and CNT microstructures [15, 41, 42]. Self-assembly [43, 44] has been used to organize nanoparticles in two-dimensional (2-D) [45] or 3-D [46] configurations.

Conversion – Photolithography was used to create polymer structures with negative poisson's ratio [28], and interference lithography (IL) was used to create 3-D polymer networks [10]. More recently, a SPPW [47] and DRW [48, 49] were used to create 3-D polymer microlattices. Pyrolysis (also known as carbonization) of polymer structures [28, 50, 51] is another example conversion technique.

Growth – CNT growth has been performed on patterned catalyst layer to create

vertical arrays of CNT microstructures [14, 52]. Kinked silicon nanowires have been grown using pulsed reactant introduction [53] and lead sulfide pine tree nanowires using dislocation motion [54]. Silica based nanowires were grown using gold catalyst [55].

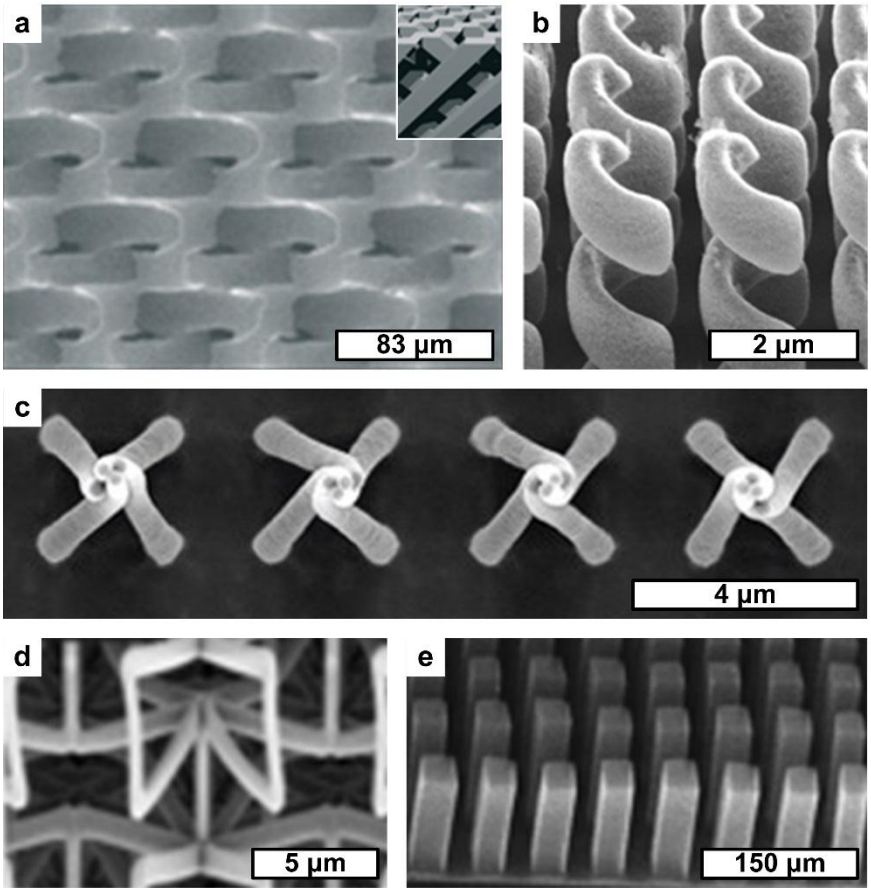

Figure 2.3 Representative structures fabricated for each class of microfabrication techniques: a) a 3-D photonic crystal fabricated by 'Removal' [33] (inset shows the design of the material), b) a broadband circular polarizer fabricated by 'Addition' [36], c) helically arranged polymer nanobristles by 'Transformation' [38], d) a 3-D auxetic microlattice fabricated by 'Conversion' [49], and e) vertical array of CNT microstructures fabricated by 'Growth' [14]. Images are adapted from each reference.

Complex hybrid processes were also developed such as layer-by-layer stacking [4, 5, 7, 56] (Removal and Addition), replica molding [57, 58] (Transformation and Conversion), and nanoimprint lithography [59, 60] (Transformation, Conversion and Removal).

2.3 CNT growth as a microfabrication method

2.3.1 Structure and exceptional properties of CNTs

Since their discovery in the early 90's [61], CNTs have been studied extensively for their unique and exceptional properties. CNTs are hollow, tubular molecules composed of carbon atoms entirely. They are, in essence, seamlessly rolled up graphene sheets. CNTs can be classified by the number of concentric walls in their structure; a CNT with one wall is called a single-walled CNT (SWNT), one with two walls is called a double-walled CNT (DWNT), and one with more than two walls is called a multi-walled CNT (MWNT). Their diameters can vary from just a few angstroms [62-64] to a few hundred nanometers [65], and their lengths can reach up to tens of centimeters [66] in the case of horizontally aligned CNTs (HACNTs) and several millimeters in the case of vertically aligned CNTs (VACNTs) [67]. Owing to their one-dimensional (1-D) structure, their properties are highly anisotropic.

Carbon atoms in CNTs are bonded by sp^2 hybridized bonds. The dissociation energy of the carbon-carbon bond is quite large, leading to exceptional mechanical properties. CNTs have outstanding elastic modulus, experimentally measured to be as high as 4 TPa [68] and predicted to be even higher [69-71], as well as tensile strength, experimentally measured to be as high as 150 GPa [72] and predicted to be higher [73], in the axial direction. In the radial direction, CNTs are soft, succumbing to even Van der Waal's forces [74]. Indeed, the elastic modulus of CNTs in the radial direction is limited to several hundreds of GPa and are typically on the order of tens of GPa [75-77]. The anisotropy appears in their thermal properties as well. Thermal conductivity of CNTs can be up to 3500 W/mk [78] in the axial direction but only 1.52 W/mk in the radial direction [79]. Electrical properties of CNTs are even more dependent on their structure. CNTs can exhibit metallic (conducting), insulating, or semiconducting behavior depending on their chirality, which is the orientation of the hexagonal graphene lattice in the tube. More convolution is introduced by sharp curvature at smaller diameters; semiconducting CNTs can become metallic, and metallic CNTs can become semiconducting [80-88]. When they do conduct, CNTs are good electrical conductors, with current carrying capacity of up to 4×10^9 A/cm^2 [89] and some

evidence of superconductivity [90-92]. Optically, CNTs are very good absorbers [93, 94], and high quality and defect free CNT surfaces can be used as almost frictionless surface, and is chemically very inert. Defects can be intentionally introduced to functionalize the CNTs with various dopants and chemicals to imbue desired properties [95], such as improved solvation [96], purity [97], and electronic structures [98, 99].

2.3.2 CNT growth process

Recent advances in high density CNT growth methods via CVD have enabled growth of VACNTs [13] (Tall VACNTs that span a large area are called 'CNT forests'). Transition metals (for example, nickel [100], iron [101], cobalt and molybdenum [102]) and their alloys are often used as catalysts. In conjunction with lithographic techniques that define catalyst outlines, deliberately defined 3-D VACNT microstructures can be grown [14, 52]. The basic process used in this thesis to grow CNT microstructures is outlined below.

CNT growth catalyst material used in this thesis is a thin film of iron (1 nm), with Al_2O_3 support layer (10 nm). The substrate is (100) silicon wafer with a 3000 Å of thermally grown SiO_2 layer. The catalyst pattern is defined by photolithography, and Al_2O_3 layer followed by iron layer is deposited by electron beam evaporation or sputtering. Once the thin film depositions is complete, the wafer is diced to an appropriate size, and lift off is performed by agitation in sonic bath in acetone. Two consecutive sonic agitations is performed with fresh acetone each time, and the wafer pieces are rinsed in isopropanol twice and then blow dried using dry air in a fume hood. This prepares the wafer pieces for CNT growth, which happens in a CVD furnace system via thermal CVD (Figure 2.4).

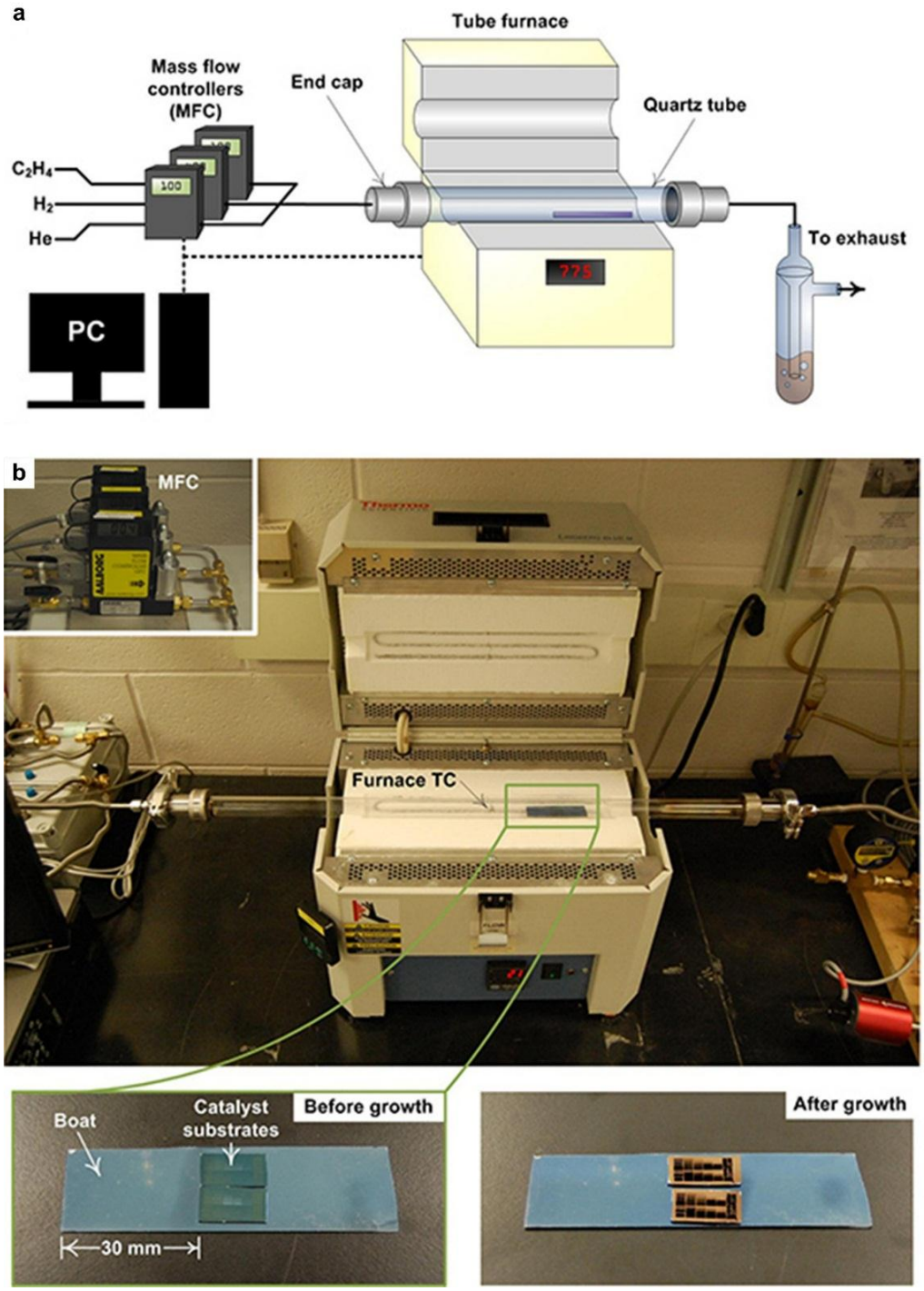

Figure 2.4 Hot-walled quartz tube CVD furnace system used to grow CNTs. a) Schematic representation of the system. Mass flow controllers are used to control the flow rates of the gasses that flow through a quartz tube in the heated zone of the furnace then to the exhaust bubbler. The mass flow controllers and temperature controller on the furnace is controlled synchronously by a computer. b) A digital photograph of the CVD furnace system showing the quartz tube sealed with end caps and a silicon boat that holds the CNT catalyst wafer pieces during the CVD procedure. Insets show the arrangement of the CNT catalyst wafer pieces on the boat before and after the growth procedure. Images are adapted from [58].

The CVD furnace system consists of Mass Flow Controllers (MFCs) that control the flow rate of gasses used in the reaction, a heated coil furnace (Lindberg Blue M Mini-Mite tube furnace from Thermo Fisher Scientific, Inc.), a quartz tube (outer diameter (O.D.) = 25mm, inner diameter (I.D.) = 22mm) with two end caps and an exhaust bubbler filled with mineral oil. The reaction gasses used are hydrogen (H_2), helium (He), helium with 100 parts per million (PPM) water vapor (He-H_2O), and ethylene (C_2H_4) as the carbon source.

Before each CNT growth run, the quartz tube is baked at 875°C for 20 minutes while flowing air through, to remove any carbonaceous deposits that may have occurred during the previous run. The CNT catalyst wafer pieces that have gone through lift off procedure and rinsed are placed on a silicon boat, then the boat is moved into the quartz tube. Two end caps seal either side of the quartz tube to prevent leakage of reaction gasses into the ambient or ambient air into the reaction environment. The MFCs and the furnace are both controlled by a computer synchronously. Once the growth run is started, the growth gasses flow into the quartz tube according to a pre-programmed recipe and the CNT synthesis occurs on the catalyst wafer pieces sitting on the boat inside the quartz tube. The temporal profiles of temperature and flow rates of reaction gasses are shown in Figure 2.5 below. The temperature during the growth step is 775°C. After the cool down step, once the furnace temperature drops below 200°C, the catalyst wafer pieces are retrieved.

The resulting CNT microstructures are made of VACNTs and their shape is a vertical extrusion of the catalyst pattern defined by photolithography (Figure 2.6). Their heights will depend on the growth step duration and their typical growth rate is 50-100 μm/min.

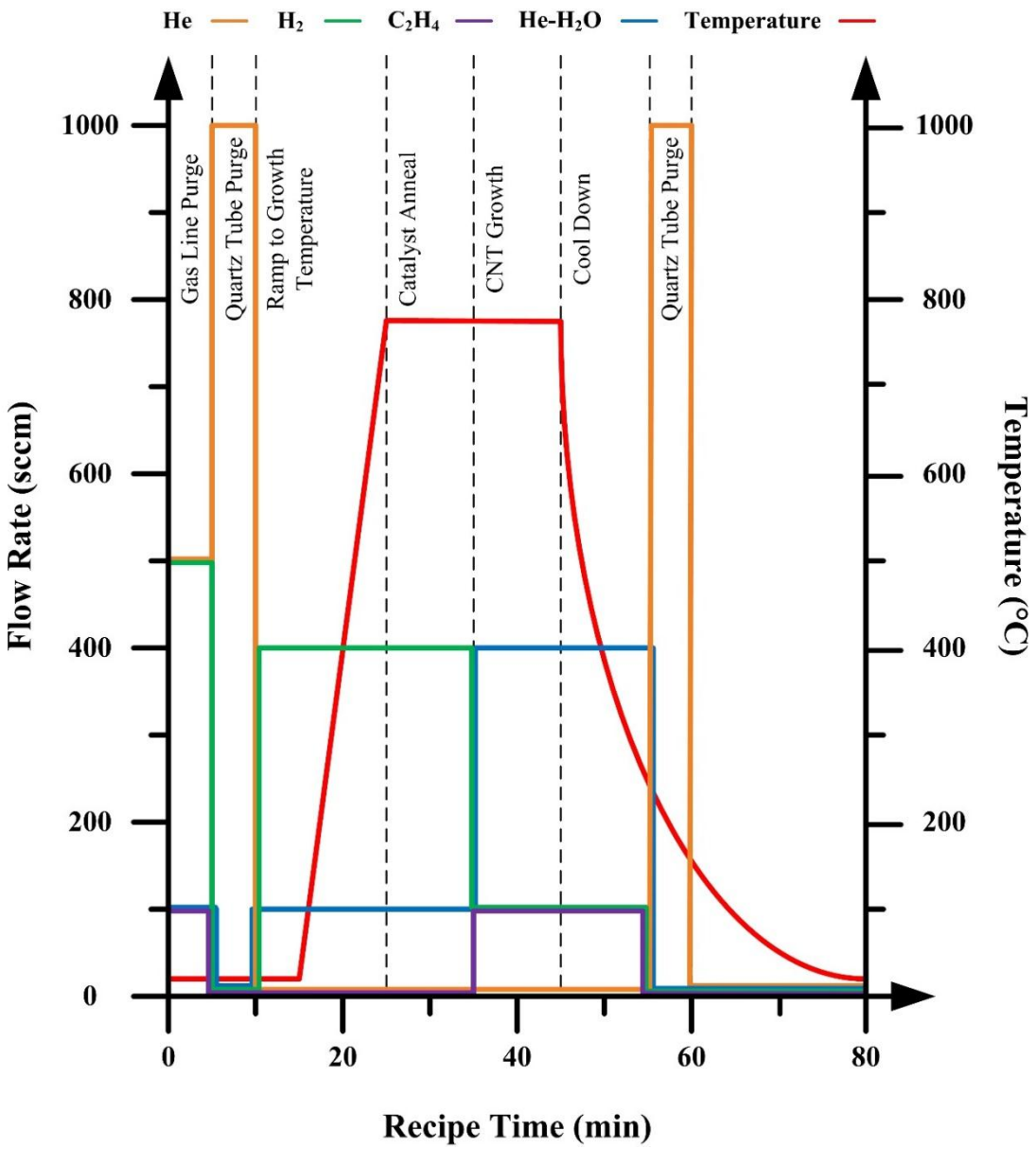

Figure 2.5 A typical CNT growth recipe used with CVD furnace system. Note that the CNT growth step can have variable duration depending on the desired CNT heights.

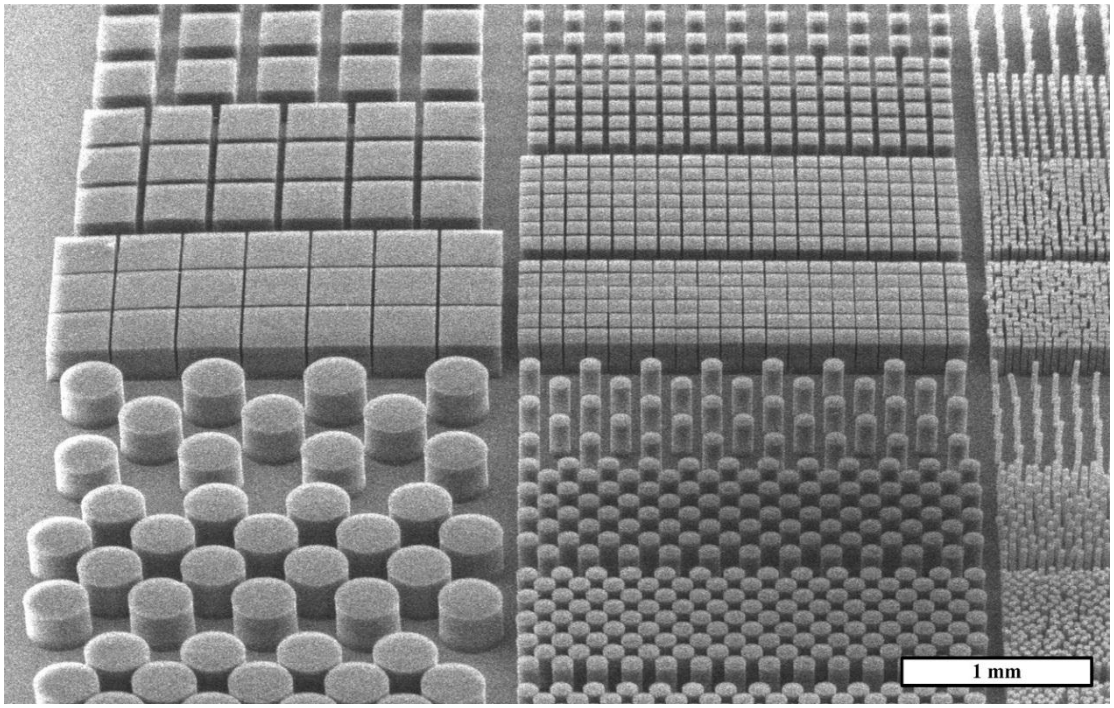

Figure 2.6 Typical CNT microstructures fabricated using the CVD furnace system.

2.4 Comparison of microfabrication techniques

A microarchitecture is a deliberately designed collection of microstructures for functional considerations, hence the fabrication techniques of microstructures is used to fabricate microarchitectures. However, there is an added requirement of relative design and placement of multiple homogeneous or heterogeneous microstructures for microarchitectures. This may render simple scaling up via serial or parallel processing unsuitable or uneconomical, and there are opportunities for entirely novel concepts to create/define a microarchitecture in one processing step.

Each microfabrication technique has different traits. In view of versatility, ability to create more geometrically complex structures is desirable. Throughput of the technique is also an important attribute to be economical. To design a microarchitecture, techniques that can achieve a large range of properties as well as large range of structure sizes will be preferred. In the following subsections, the microfabrication classes will be compared for their throughput, structural complexity, range of properties (Elastic modulus is used as a representative property) and structural dimensions achieved. For the purpose of comparison, CNT growth is used as a representative technique in the

‘Growth’ class, and ‘Transformation’ will be presented in the form of post processing that builds on other processes.

2.4.1 Complexity of microstructure geometry

Microstructures can have varying degree of geometrical complexities. For instance, straight pillars are less complex than curved pillars, which are in turn less complex than helices. Geometrically more complex structures are favorable, since it signifies the ability to control the properties/functions in more dimensions and more complex structures are often essential to building metamaterials. In this thesis, the geometry of microstructures will be classified into the following 3 categories of increasing complexity:

1. Straight – The trajectory of the microstructure is linear. Microstructures with vertical geometries from the substrate as well as inclined geometries fall under this category.

2. In-plane – The trajectory of the microstructure is described by a non-straight line. There exists a plane in which the line lies completely on. Simple curved and zigzag structures fall under this category.

3. Out-of-plane – The trajectory of the microstructures is described by a non-straight line. There does not exist a plane in which the line lies completely on. Helical structures as well as structures that have multi-directional curvatures fall under this category.

Example structures belonging in these categories are shown below in Figure 2.4.

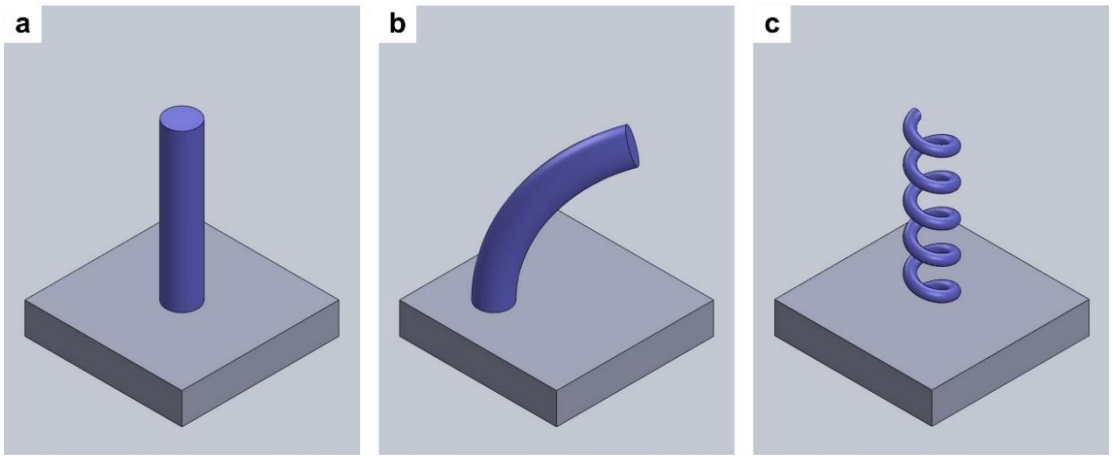

Figure 2.7 Complexity of microstructure geometries: a) straight b) in-plane, and c) out-of-plane.

2.4.2 Throughput and structural complexity

For each class of microfabrication techniques, a typical fabrication throughput is calculated in terms of volume per time and plotted against achievable microstructure complexity (Figure 2.8). CNT growth can produce straight structures at high throughput, and can be extended to produce structures with in-plane geometry via post processing. 'Conversion' techniques have similar traits, and has added possibility of achieving microstructures with out-of-plane geometries, albeit at a very low throughput. 'Addition' techniques can produce microstructures with out-of-plane geometries but are limited to medium throughput. 'Removal' techniques are limited to straight geometries and medium throughput. Currently no fabrication technique can achieve out-of-plane microstructure geometries at high throughput.

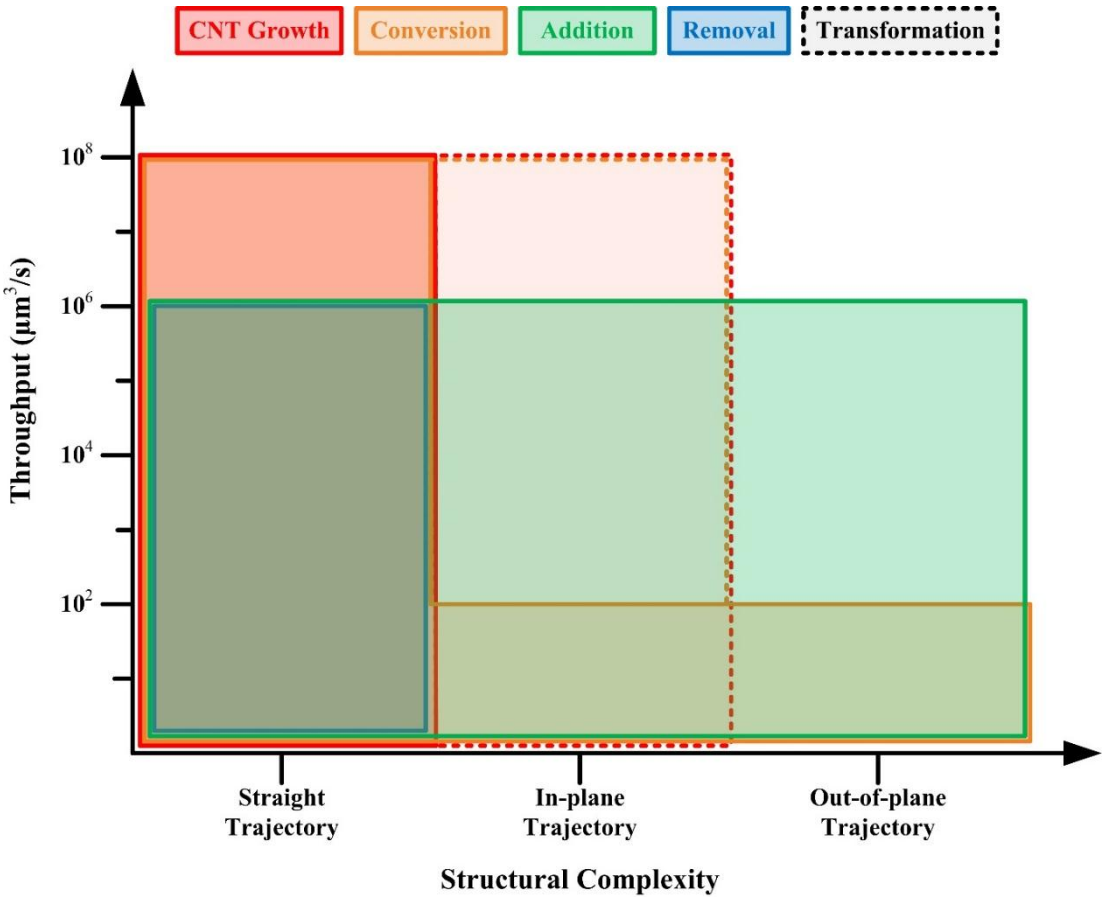

Figure 2.8 An order of magnitude comparison of throughput and microstructure complexity achieved by each class of microfabrication techniques.

2.4.3 Elastic modulus and structural dimension

The range of elastic modulus of resulting microstructures is plotted against the range of feature sizes achieved with each class of microfabrication techniques (Figure 2.9). Horizontal lines indicate material specific processing, where only the microstructure sizes can be varied. CNT growth is limited to larger microstructure sizes and lower elastic modulus. 'Conversion' can achieve microstructures with sizes down to 10s of nanometers, but are limited to mid-range elastic modulus. Other 'Conversion' techniques can convert the polymer into amorphous carbon to increase the elastic modulus slightly. 'Addition' and 'Removal' techniques can achieve higher elastic modulus, but share the limitation of material specific processing. If other values of elastic modulus are desired, the material needs to be changed and compatible processes need to be developed. CNT microstructures have the flexibility of being able to achieve

a range of elastic modulus albeit on the lower side. This stems from the fact that CNT microstructures consist of collection of VACNTs and behave like foams [103] whose properties depend on morphological characteristics such as diameter and alignment [104-107]. 'Transformation' techniques can be utilized to reduce the structure size and increase the elastic modulus slightly. Currently, a continuous tuning of elastic modulus at higher ranges is unavailable as well as at lower ranges with structure dimensions in the sub-micrometer range.

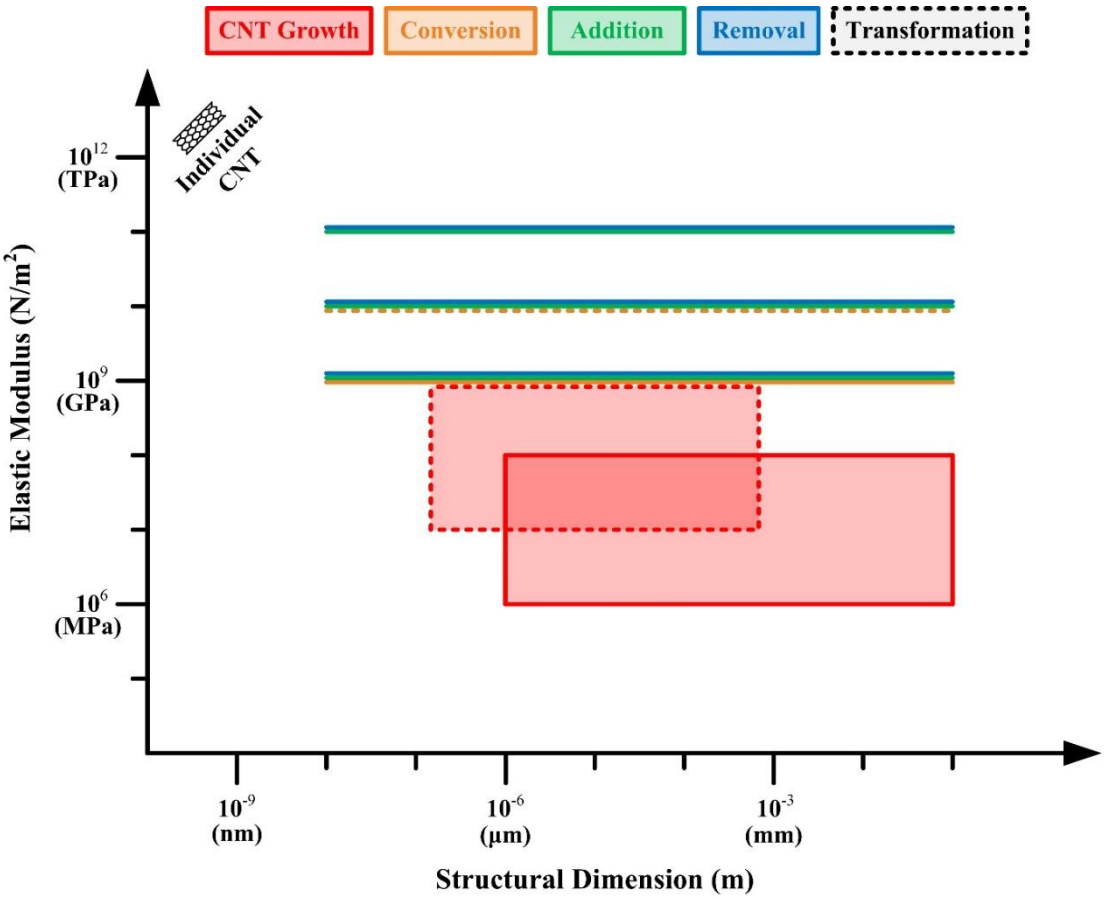

Figure 2.9 An order of magnitude comparison of elastic modulus and structure sizes achieved by each class of microfabrication techniques.

CHAPTER 3

STRAIN-ENGINEERED GROWTH OF CNT MICROARCHITECTURES

Significant portions of this chapter with additional editing are published in: De Volder M., Park S.J.* (*equal contributions), Tawfick S.H. & Hart A.J., Strain-Engineered Manufacturing of Freeform Carbon Nanotube Microstructures. Nature Communications, 2014; 5.*

This chapter describes a novel method to fabricate geometrically complex three-dimensional (3-D) microstructures using carbon nanotube (CNT) growth by engineering the growth rates of the microstructures. First, modulation of CNT growth rate by engineered catalyst stack is presented. Then a comprehensive characterization of CNTs grown on the engineered catalyst stack is presented. Then, a strain-engineering concept to produce unidirectionally deflected CNT microstructures is demonstrated. Finally, a collection of microarchitectures comprising of complex 3-D structures as small in dimensions as 5 μm in large arrays spanning more than 100 by 100 structures that are enabled by the developed method is showcased.

3.1 Modulation of CNT growth rates via engineered catalyst film stack

Strain mismatch in thin film stacks has been exploited in semiconductor industry to tune the electrical properties of the films [108], to deflect microcantilevers [109-111] for applications in micro-electromechanical systems (MEMS) and even to perform microscale origami using induced plastic strains [112]. A strain mismatch can be applied to CNT microstructures as they grow (in the direction normal to the substrate)

via modulation of local CNT growth rate [113] spatially within the bounds of the patterned catalyst. This enables the growth of closely packed heterogeneous complex microstructure arrays.

It was first observed that the density and growth rate of CNT forests can vary depending on the material beneath the catalyst support layer (Al_2O_3 in Fe/Al_2O_3 catalyst stack). Introduction of TiN film under the catalyst stack retards the CNT growth rate, as shown in Figure 3.1. Patterning of the CNT growth catalyst (Fe/Al_2O_3) on a TiN "checkerboard" followed by a standard CNT growth run (described in Section 2.3.2) results in a "bi-level" CNT microstructure array. The catalyst patterns directly on SiO_2 grow CNTs to ~100 µm (in < 2 minutes), whereas the patterns on TiN (upon SiO_2) grow CNTs to 50 µm in the same time span (Figure 3.1a). In Figure 3.1b, "tri-level" CNT forests are grown by arranging patches of catalyst on SiO2, 70 nm TiN, and 140 nm TiN. This principle could be extended to an arbitrary number of levels or even continuous height gradients via additional lithography and underlayer deposition steps that modulate the growth rate via catalyst/underlayer interactions.

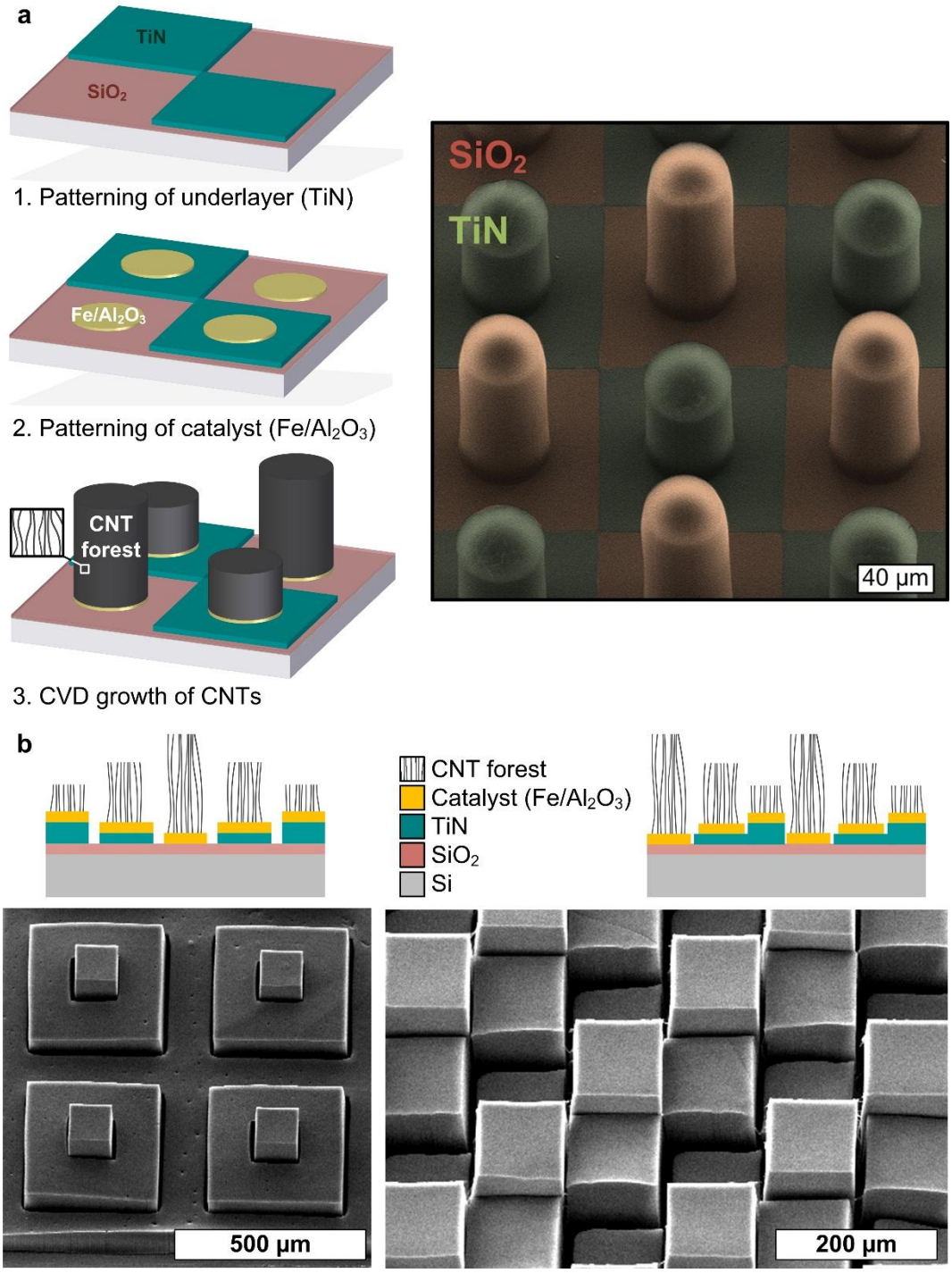

Figure 3.1 Schematic representation of multi-height CNT microstructure growth by introduction of growth retardant layers. a) Introduction of growth modulating TiN layer for dual height-scale microstructures b) Extension of the concept to triple height-scale structures.

3.2 Growth characteristics of CNT forests on Fe/Al_2O_3 and $Fe/Al_2O_3/TiN$

In order to controllably fabricate complex CNT microstructures using this technique, characteristics of the resulting material need to be known. CNT growth process is a complex chemical reaction and the conditions used in the process can alter their properties drastically. Therefore a matrix of growth conditions was explored and the resulting CNT forest materials were characterized for their growth rate, growth kinetics, density, alignment, quality, catalyst particle morphology and elastic modulus (in compression). The growth conditions were varied as shown in Table 3.1.

Table 3.1 A list of parameters varied for growth and subsequent characterization of CNT microstructures grown on the engineered catalyst stack.

Reaction parameters	**Parameter values used**
CNT growth temperature (°C)	755, 770, 785, 800
CNT catalyst annealing time (min)	10, 30
TiN underlayer thickness (nm)	0,50,100

CNT growth temperature affects the breakdown of the carbon source gas in the reactor and the intrinsic growth kinetics of CNTs at the catalyst, CNT catalyst annealing time affects the catalyst morphology, and TiN underlayer thickness will affect the CNT growth rate. The growth temperatures were chosen to represent a typical range of temperatures used in CVD synthesis of CNTs. The growth step duration used for all experiments was 5 minutes and the substrate dimensions were 5 mm by 5 mm.

3.2.1 Growth rate and kinetics

First, the heights of the samples were characterized by optical microscopy (Zeiss Axio Imager Z1m) using a dark field filter. The CNT forest is placed on the microscope stage and the stage is translated in z-direction until the top of the CNT forest is in focus. The z position is noted, and the microscope stage is translated until the substrate is in focus. The z position is noted again, and the difference between the z positions of the top of CNT forest and the substrate is used as the height of CNT forests.

CNT forests are ideally very uniform, with flat top surface (Figure 3.2a), however in reality, due to spatially varying chemical potential [114], the CNT forest top surface can either be convex (Figure 3.2b) or concave (Figure 3.2c). In order to provide a better understanding of the CNT forest morphology, the height was measured at 9 different locations. The average of 9 measurements is considered to be the representative height of the CNT forest. The locations at which the height measurements were performed is shown in Figure 3.2d.

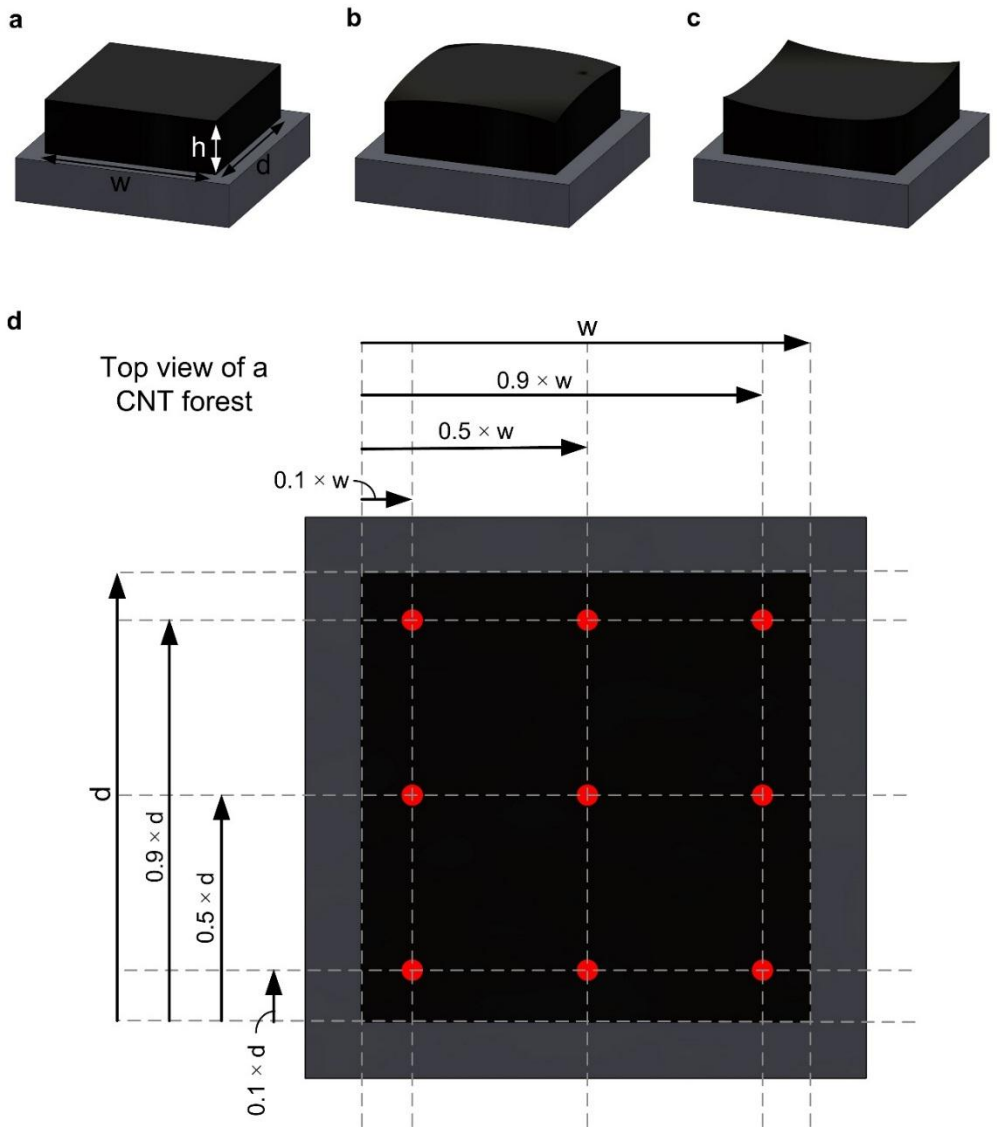

Figure 3.2 Schematic representation of possible CNT forest top surface morphologies. Top surface of CNT forests can be: a) ideally uniform, b) convex, or c) concave. d) Optical height characterizations are done at multiple locations to better map the top surface curvature.

The heights of CNT forests produced after 5 minutes of growth step are shown in Figure 3.3. At low temperatures, CNTs grow slower and as the temperature is increased, the CNT forests grow faster and faster, until at a threshold temperature, the growth rate peaks and beyond that the CNT growth rate becomes slower. The growth rate decrease at higher temperatures may be due to excessive gas decomposition and/or the catalyst deactivation [67]. For $Fe/Al_2O_3/SiO_2$ the peak does not appear within the temperature ranges tested, whereas for those on TiN the peak temperature is around 785 °C.

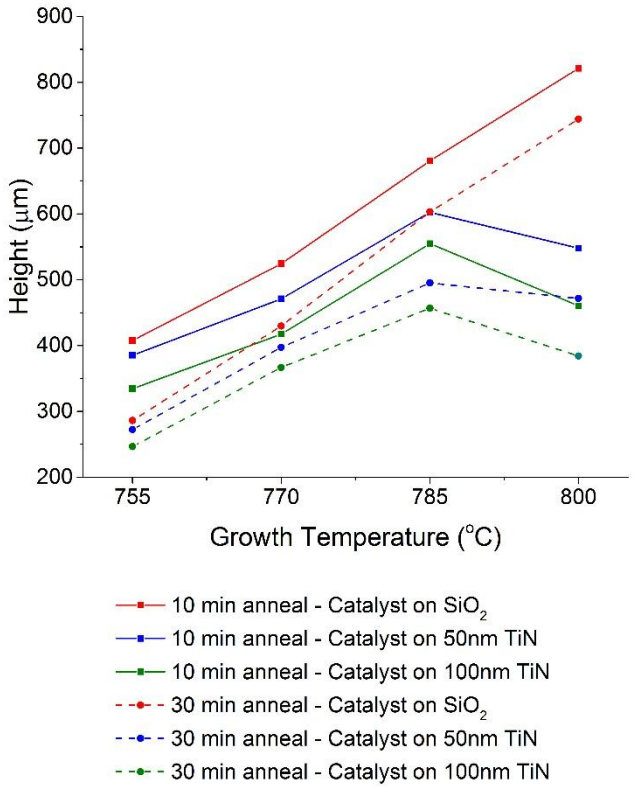

Figure 3.3 Heights of CNT forests on engineered catalyst stacks.

A notable trend is that the CNT growth rates is negatively correlated to TiN underlayer thickness, ranging from tallest CNTs when there is no TiN underlayer to shortest CNTs when the TiN thickness is 100 nm, across the entire growth temperature range tested. Comparing results from 10 minute annealing and 30 minute annealing, longer catalyst annealing time reduces the CNT growth rate at all growth temperatures and TiN underlayer thicknesses by 9-30 %.

Calibrating the relative growth rates of CNTs on Fe/Al_2O_3 and Fe/Al_2O_3/TiN will enable design of multi-height structures with precisely tuned heights. CNT growth rates normalized to CNTs on Fe/Al_2O_3 are presented in Figure 3.4. Relative growth rate of CNTs on Fe/Al_2O_3/TiN decreases as growth temperature increases, regardless of TiN underlayer thickness or the catalyst annealing time. CNTs grown on thicker TiN underlayers are consistently shorter than those grown on thinner TiN underlayer.

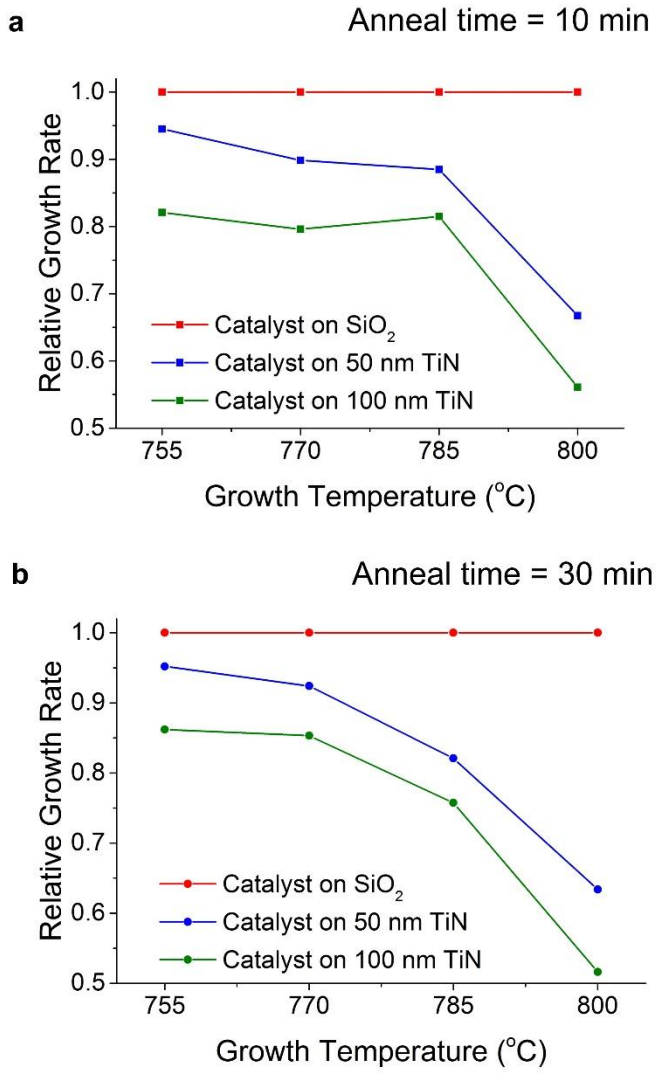

Figure 3.4 Normalized CNT growth rates on Fe/Al_2O_3/TiN relative to those on Fe/Al_2O_3: a) 10 minute annealing time, and b) 30minute annealing time.

Then the uniformity of the CNT forest growth was characterized by comparing the variations between the 9 height measurements for each forest as a fraction of the

average height. The uniformities of the forests were assessed by calculating coefficient of variation (C_v) by the following formula:

$$C_v = \frac{\sigma_h}{\mu_h} \quad (1)$$

where σ_h is the standard deviation and μ_h is the mean of height measurements. When the coefficient of variation is less than 0.05, the CNT forest is classified to be 'uniform'. When CNT forests are not uniform, the morphology can be determined by quantifying center elevation (C_e), by the following formula:

$$C_e = h_{center} - \mu_{h,corners} \quad (2)$$

where h_{center} is the height measurement at the center and $\mu_{h,corners}$ is the mean of the corner heights. The sign of this term determines if the center is raised or recessed compared to the corners. When the sign is positive, the center is raised compared to the corners, hence the top surface is convex, and when it is negative, the top is concave. The C_v values are plotted in Figure 3.5.

At the minimum and maximum of CNT growth temperatures, the resulting CNT forests have non-uniform top surfaces; at lower end, the top is concave, at higher end the top is convex. In the mid-range temperatures CNT microstructures are uniform. For forests grown at 770°C and below, the C_v values are lower as TiN underlayer thickness increases, and longer catalyst anneal time generally increases C_v value. Forests grown at 785°C and above show the exact opposite trend; C_v is lower for thicker TiN underlayers, and for shorter catalyst anneal times. In summary, transition of uniformity trend happens between 770°C and 785°C and longer anneal time increases the non-uniformity.

Finally, temporal evolution of relative growth rates and morphology is characterized by a series of growths with constant reaction conditions and varying growth times. CNT

growth at 800°C with 10 minute of catalyst annealing was chosen as this condition has largest relative growth difference. The temporal CNT forest height and relative growth rates at this growth condition is shown in Figures 3.6a and b with error bars showing 1 standard deviation of 9 measurements outlined in Figure 3.2a. The height evolution of CNT forests observed in this study is consistent with a previous study on growth height kinetics [115].

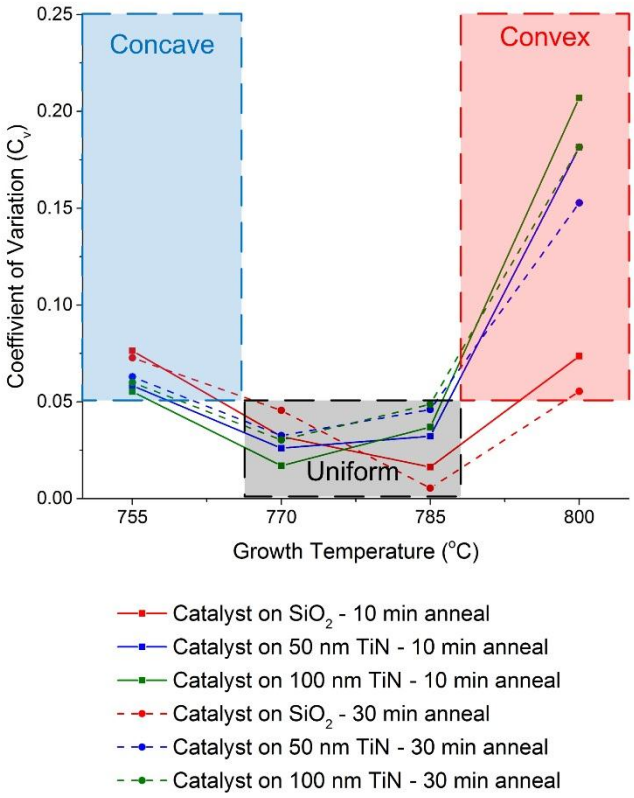

Figure 3.5 Top surface morphology of CNTs grown on SiO_2 and TiN.

The growth of CNT forests terminates after 10 minutes at this condition, beyond this time the CNT forest heights do not increase. The heights of CNT forests from 10 minute growth run is slightly taller than those produced from to 15 minutes, reflecting the fact that the run to run variations still exist. The growth rates of CNTs on TiN trail off faster than that on SiO_2, hence the relative growth rates evolve temporally, decreasing as the growth time is extended.

Finally, the CNT forest uniformity evolution is considered. Figure 3.7 summarizes the C_v values for this time series. The forests are mostly convex and the C_v values do not correspond to the growth times.

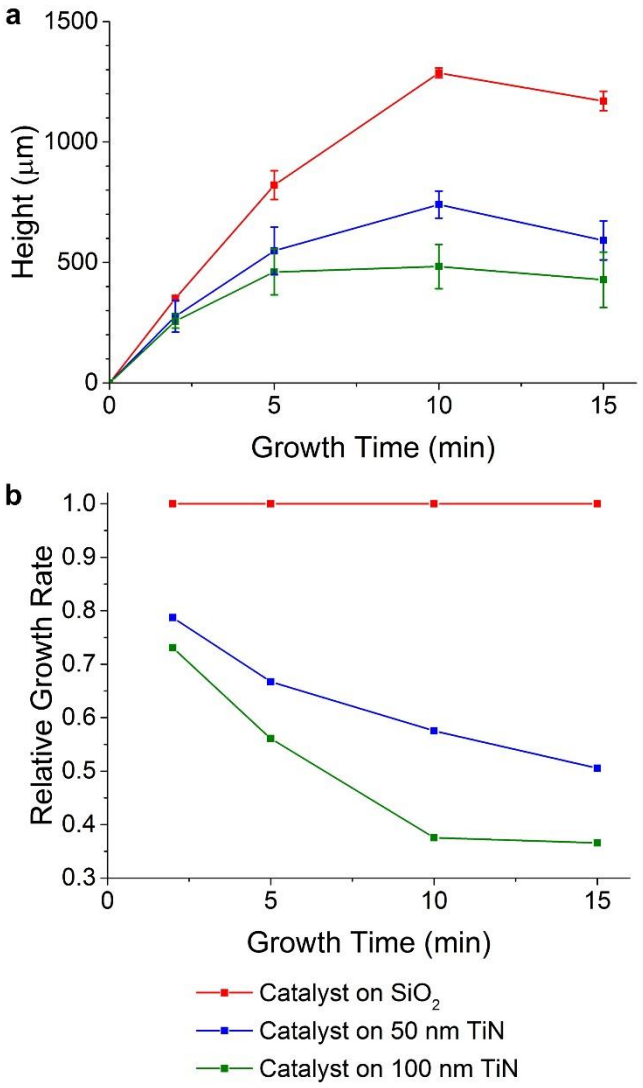

Figure 3.6 Temporal height evolution of CNT forest grown at 800°C with 10 minute of catalyst annealing: a) absolute height measurements, and b) relative growth rate.

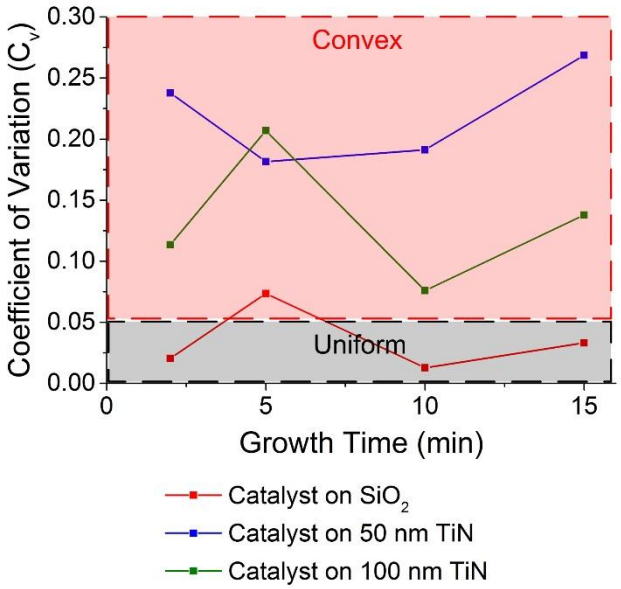

Figure 3.7 Coefficient of variation for CNT forests grown at 800°C with 10 minute of catalyst annealing.

3.2.2 CNT mass density and alignment

The mass of the CNT forests were measured using a microbalance. Both the areal density (Figure 3.8a) and the volumetric density (Figure 3.8b) were calculated. The areal density can be related to the efficiency of the reaction, showing how much carbon has been turned into CNTs per unit catalyst area. The areal density of CNT forests decreases slightly over the growth temperature range tested with slight decrease in the mid-range; 770°C and 785°C. Longer annealing time generally decreases the density of the resulting forests, and causes the areal density in the 770-785°C range to be lower than at 800°C. The areal density is higher for CNT forests grown on TiN underlayer than those on SiO_2.

The volumetric density relates the areal density to the height of the CNT forests, and consequently relates to the alignment of CNTs within a forest assuming all other factors remain the same. In reality, the different catalyst stacks are expected to produce CNTs with varying diameters, hence the relationship may not be as straight forward. The volumetric density is the highest at 755°C and decrease as the temperature is increased, and hits the minimum at 785°C and increases again at 800°C. Again, longer anneal time

generally increases the volumetric density variation, leading to higher densities at 755°C and 800°C and but lower densities in the mid-range. The CNTs grown from catalyst stack on SiO_2 have lower volumetric density than those grown on TiN, suggesting that the CNTs are more aligned in absence of TiN underlayer.

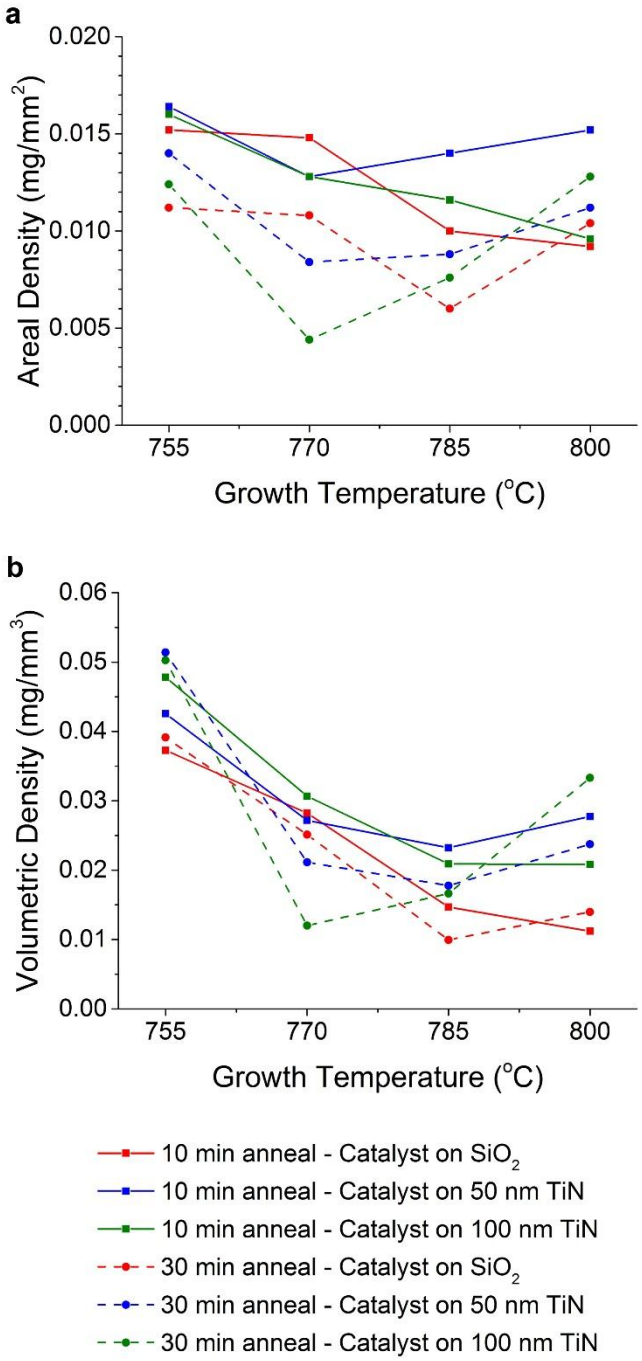

Figure 3.8 CNT forest mass density: a) areal density, and b) volumetric density.

Small angle X-ray scattering (SAXS) was used to further investigate the CNT forest morphology [116, 117]. The experimental setup is shown in Figure 3.9. For this experiment, CNTs were grown for 10 minutes on SiO_2, and on 40 nm, and 80 nm TiN layers at 775°C; these samples reached lengths of 800, 500, and 400 µm respectively. The scattered X-ray intensities were fitted to a mathematical form factor model for hollow cylinders [115] to calculate the Herman's orientation parameter, which is a measure of alignment. The Herman's orientation parameter increases from the top of the forest (the initial growth), then reaches a maximum, and then decreases toward the bottom of the forest (Figure 3.10). This trend is typically observed for CNT forests grown by CVD, and has been attributed to density variation due to collective activation and deactivation of the growing CNT population [116].

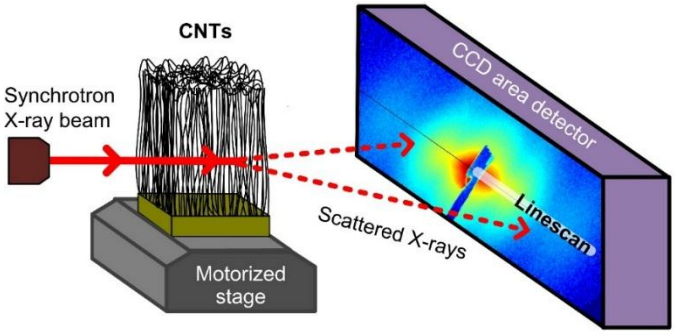

Figure 3.9 SAXS measurement setup. (Figure adapted from [116])

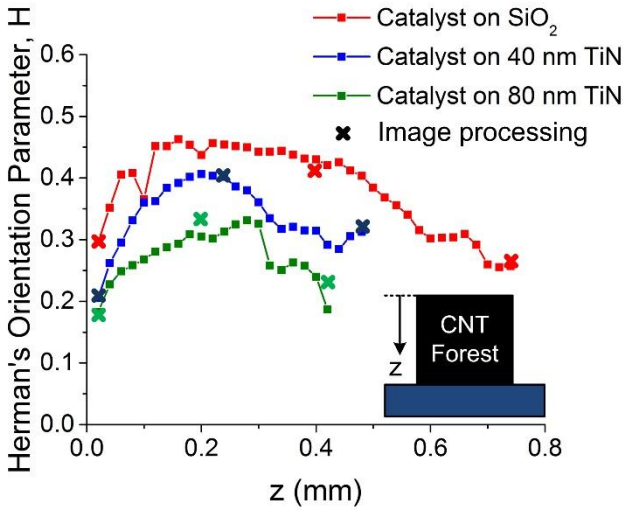

Figure 3.10 Herman's orientation parameter measured by SAXS.

However, SAXS is time consuming and requires an X-ray synchrotron source, therefore an alternate method for characterizing the Herman's orientation parameter using a high resolution scanning electron microscopy (SEM) imaging was used [118]. The SEM images were taken at the middle of the forests to represent the entire sample. The SEM images were first passed through a threshold to highlight CNTs from the background (Figure 3.11a and b), then analyzed by taking a fast Fourier transform (FFT) of the image (Figure 3.11c) and integrating the magnitude in the azimuthal direction for frequencies corresponding to 100-200 nm physical spacing (Figure 3.11d). These values were relevant as the previous calculations of CNT areal density with SAXS determined average spacing between the CNTs to be in this range [116]. The angle range from axis perpendicular to CNT axis to 90 degrees clockwise was used for integration. The image processing technique was compared to SAXS using the same samples, and were found to produce comparable values (crosses in Figure 3.10).

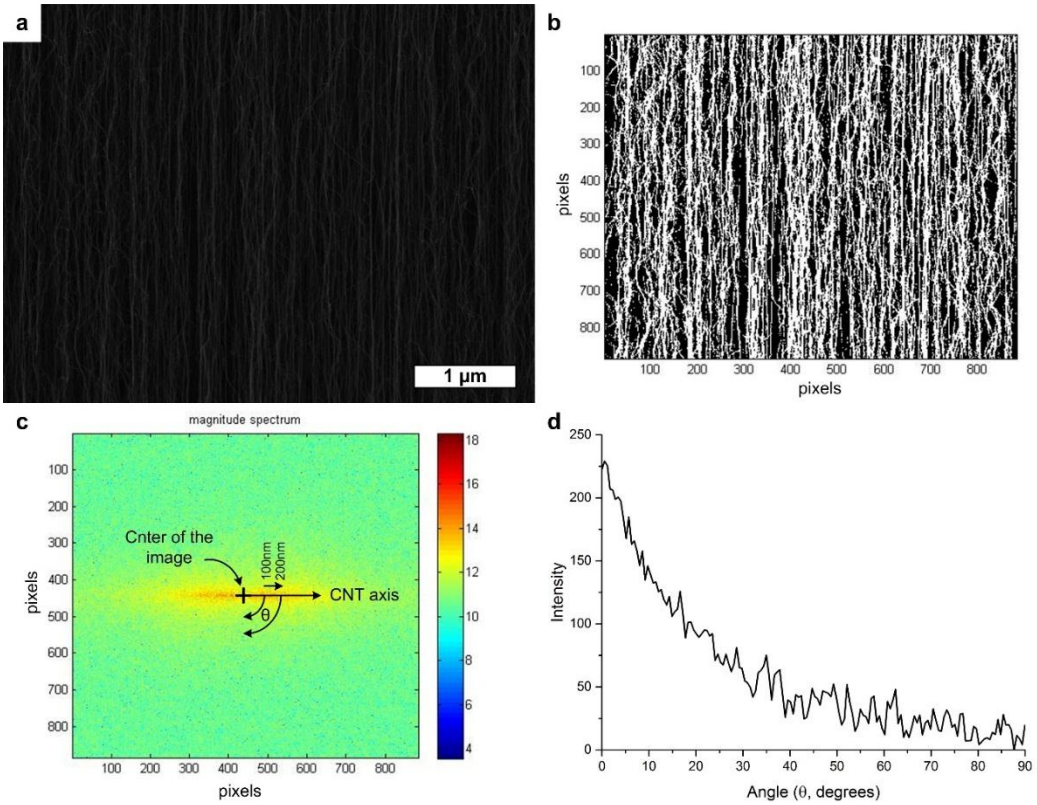

Figure 3.11 Herman's orientation parameter calculation by FFT of high resolution SEM images. a) Original SEM image, b) CNTs highlighted by applying a threshold, c) FFT of the image with CNTs highlighted, d) Integration of the data for Herman's orientation parameter calculations.

From the integrated magnitude intensity over angle, Herman's orientation parameter (H) is calculated using the following formulae.

$$H = \frac{1}{2}\left(3\langle cos^2\emptyset\rangle - 1\right) \quad (3)$$

and

$$\langle cos^2\emptyset\rangle = \frac{\int_0^{\pi/2}(I(\emptyset)\, sin\emptyset\, cos^2\emptyset)d\emptyset}{\int_0^{\pi/2}(I(\emptyset)\, sin\emptyset\,)d\emptyset} \quad (4)$$

where $\emptyset$ is the angle from the CNT axis and I is the azimuthal integration of magnitude phase of the transformed image. The Herman's orientation parameter of the CNT forests calculated by image processing is shown in Figure 3.12 below.

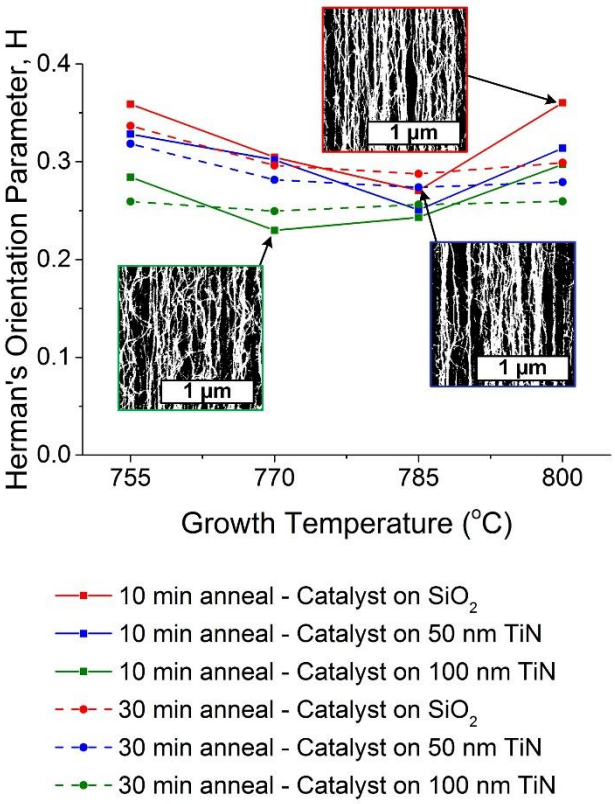

Figure 3.12 Herman's orientation parameter of CNT forests calculated by FFT of high resolution SEM images.

Herman's orientation parameter generally decreases as the growth temperature is increased, although at 800°C it increases slightly. Thicker TiN underlayers generally produced worse alignment in CNT forests. The correlation between density and Herman's orientation parameter is shown in Figure 3.13. It is shown that thicker TiN underlayer reduces the slope of the linear correlation between density and alignment.

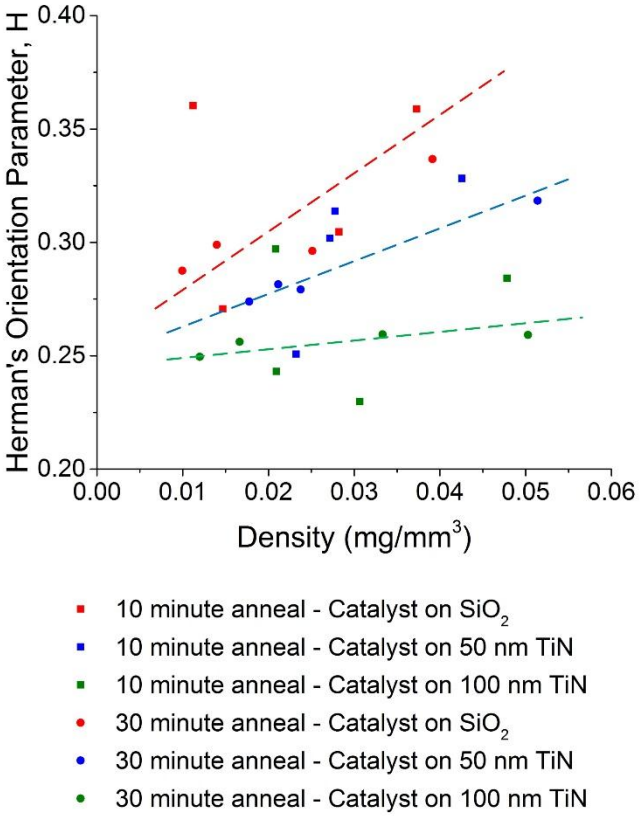

Figure 3.13 Correlation between Herman's orientation parameter and density of CNT forests.

CNT forests grown from Fe/Al_2O_3/TiN layer have lower slope on density-alignment (i.e. the density increases without much increase in alignment) map than those grown on Fe/Al_2O_3 and thicker TiN layer causes this slope to be further reduced suggesting that the TiN underlayer causes CNT diameters to be smaller [118]. High resolution SEM images show that CNTs are prone to bundling, and growing in a wave-like arrangements. CNTs with smaller diameter have lower bending stiffness and hence are more likely to bend and curve within the CNTs forests during growth which causes complicated mechanical coupling of neighboring CNTs, leading to lower alignment at

a given number density. Characterization of CNT diameters on Fe/Al_2O_3 and $Fe/Al_2O_3/TiN$ are presented in section 3.2.4.

3.2.3 CNT quality

CNTs can have various structural imperfections, such as atomic vacancy and rotated bond called stone-wale defect [119]. The defect density can be used to quantify the quality of CNTs, and can be derived from the Raman spectra of the CNT samples [120-122]. The relative peak intensities of the G band (characteristic of sp^2 hybridized carbon-carbon bond) to the D band (arising from amorphous carbon and structural defects in CNTs) is used as a measure of CNT quality. CNTs with higher quality will have better structural integrity, leading to more idealized properties such as higher stiffness, strength, electrical and thermal conductivities [123] whereas those with lower quality can be used to exploit the defects for functionalization or nucleation [124]. An example Raman spectrum of a CNT forest is shown below in Figure 3.14.

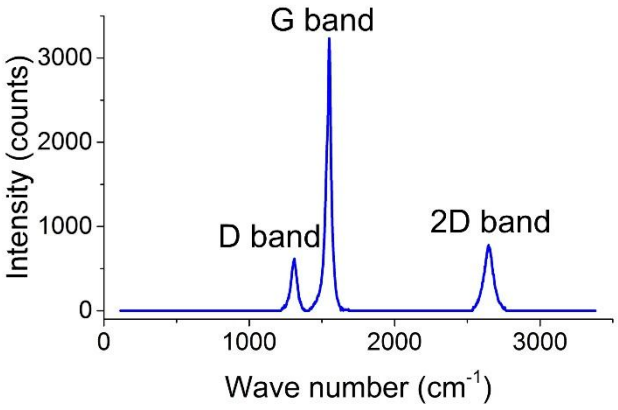

Figure 3.14 An example Raman spectrum of a CNT forest.

The G/D ratio of measured (Dimension P2, Lambda Solutions, λ = 533 nm) from the top of CNT forests are plotted in Figure 3.15. Increasing the TiN underlayer thickness negatively impacts the G/D ratio, as do longer annealing times. This effect is more pronounced at lower growth temperatures, and at higher growth temperatures, the G/D ratio is similar across all forests. The general trend is that higher temperature increases

the G/D ratio which is consistent with higher growth temperature leading to higher G/D ratios on single-walled CNTs (SWNT) [125]. This is due to higher temperatures favoring thermally activated processes such as carbon source gas decomposition and surface diffusion. The difference between 10 minute annealed and 30 minute annealed samples, can be attributed to differences in the catalyst particle sizes. The catalyst particles are expected to be larger for samples annealed for longer times [126], which will lead to larger activation energy to grow CNTs.

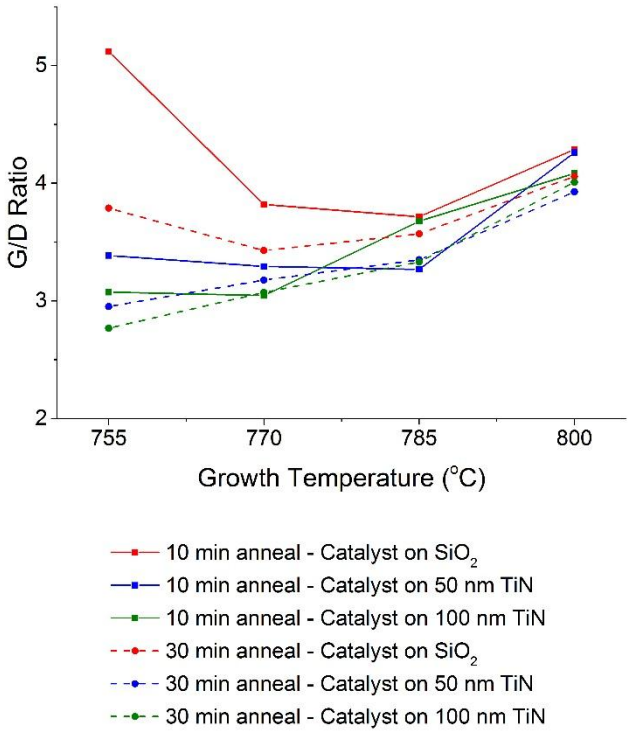

Figure 3.15 CNT quality indicated by G/D ratio measured by Raman spectroscopy.

3.2.4 CNT diameter and catalyst particle morphology

It has been demonstrated in the previous sections that the CNTs grown on different engineered catalyst stacks may have different diameters and catalyst particle heights. Hence the CNT diameters are indirectly measured by using the correlation with catalyst particle height to CNT diameters [126-128].

The catalyst film stack is annealed before CNT growth occurs. This de-wets the iron film into iron nanoparticles that are the right size to facilitate CNT growth. The catalyst morphology is an important factor for CNT growth. The CNT growth rate is closely tied to the catalyst morphology [129-131]. Therefore it can be suspected that the difference in the growth rate of the CNTs on SiO_2 and TiN is due to the morphology of catalysts after annealing. The catalyst morphology will also affect various other characteristics such as the diameter, density and alignment of the CNTs [67, 132, 133].

SAXS was used to measure the CNT diameters in the forests grown with 0, 40 and 80 nm TiN underlayer at 775°C (Figure 3.16). The CNT diameter is smaller for increasing TiN underlayer thickness. Specifically, CNTs on SiO_2 have initial average diameter of 9.5 nm, while CNTs on TiN are approximately 8 nm in diameter. These measurements further support the AFM data, which showed that the catalyst particles on TiN layers are smaller than those on SiO_2. The decrease in diameter with growth time has been attributed to diffusion of the catalyst into the Al_2O_3 catalyst support layer [116, 134]. These results show that the CNT diameter and spacing can be related to catalyst particle size and spacing.

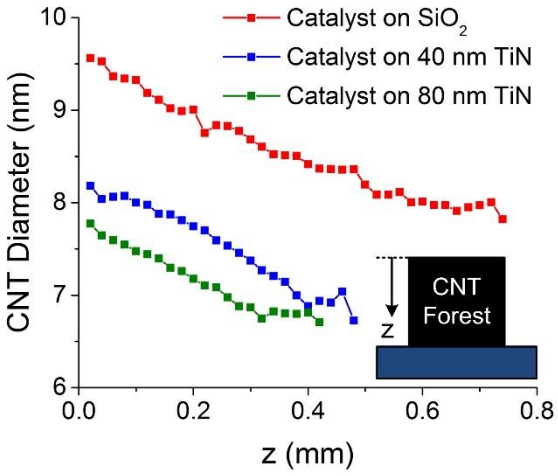

Figure 3.16 SAXS measurement of CNT diameter.

Atomic force microscopy (AFM) shows that TiN film has a small root mean square (RMS) roughness, on the order of a few nanometers, and the catalyst stack deposited on them follow similar morphology (Figure 3.17)

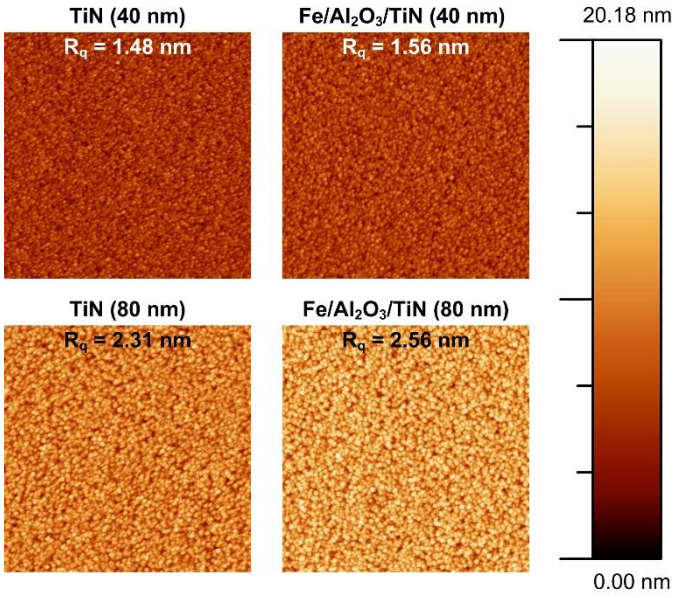

Figure 3.17 Morphology of as-deposited TiN films and catalyst stacks on TiN films.

Once annealed, the TiN film becomes much rougher, with roughness values as high as 10 nm (Figure 3.18a). Notably, the annealed 80nm TiN film forms mounds that are tens of nanometers high and hundreds of nanometers wide (Figure 3.18b). The catalyst stack deposited on the TiN films suppressed this effect, but smaller mounds are still present after annealing as shown in Figure 3.18c.

The catalyst particle height and spacing for the samples are plotted in Figure 3.19. The catalyst particles show decreasing trend when TiN layer thickness is increased (from 7.5 nm for SiO_2 to 5.2 nm for 80 nm TiN), confirming a correlation with SAXS diameter measurements. The catalyst spacing stays comparable around 18 nm.

Catalyst morphology characterization was performed on the catalyst stack used to produce the CNT forests in the parametric study. The catalyst stacks were annealing using identical recipe sans growth step, and AFM measurements were performed. The AFM images were analyzed for catalyst particle diameter (Figure 3.20a) and spacing (Figure 3.20b).

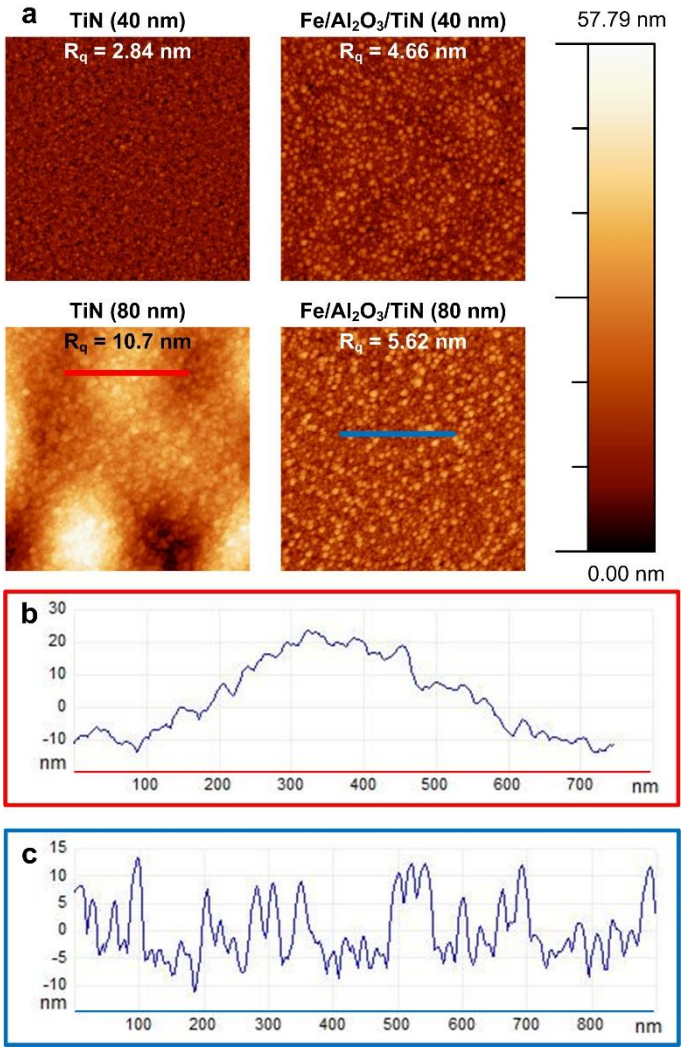

Figure 3.18 Morphology of annealed TiN films and catalyst stacks on TiN film. a) AFM image of TiN films/catalyst stacks on TiN films upon annealing b) Height profile of TiN film after annealing c) Height profile of catalyst stack on TiN film after annealing.

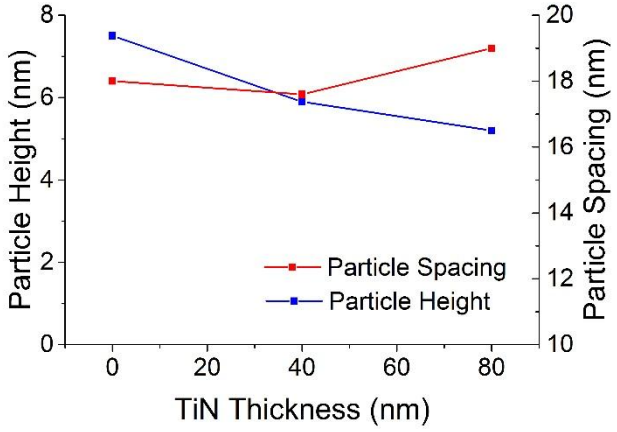

Figure 3.19 Catalyst particle height and spacing for various catalyst stack underlayers. 0 nm TiN corresponds to catalyst stack directly on SiO_2.

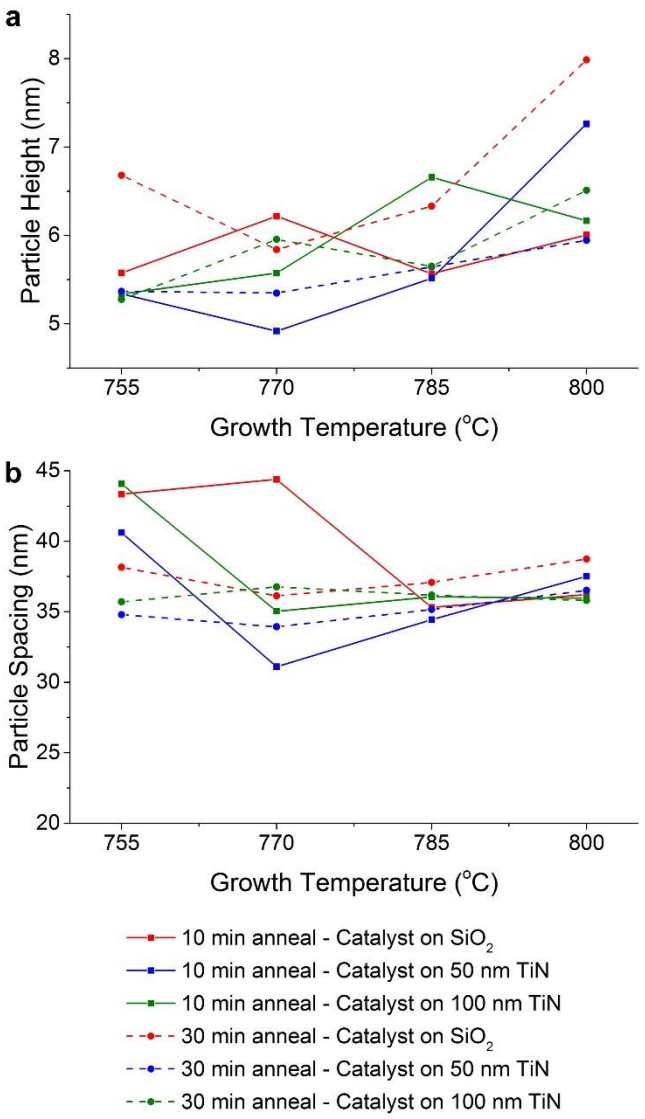

Figure 3.20 AFM characterization of annealed CNT catalyst stack morphology: a) catalyst particle height, and b) catalyst particle spacing.

The catalyst particle diameter shows an increasing trend over the range of temperatures tested, increasing at longer annealing times and higher growth temperature. Longer annealing times and thicker TiN underlayer thickness reduce the catalyst particle heights on average. The catalyst particle spacing decreases slightly as the growth temperature goes up for shorter annealing times, For longer annealing time, the spacing remains mostly constant over the range of growth temperatures tested. Again, increasing annealing time and TiN layer thickness lead to smaller spacing.

3.2.5 Elastic modulus

The CNT forests produced in the parametric study has been subjected to compression tests to measure their elastic moduli. A dynamic mechanical analyzer (DMA, TA Instruments Q800) was used to perform the tests. The samples were loaded to 18N in a force controlled compression, at a strain rate less than 0.001/s to avoid effects of high-strain rate on the results. The sample was compressed to 0.01N before the test was performed, to reduce the effect of curved top surface of the samples. Since CNT forests behave like foams [103], the initial loading and unloading slopes of the stress-strain curves were used to calculate the elastic moduli (Figure 3.21). The elastic modulus of all samples tested are shown in Figure 3.22.

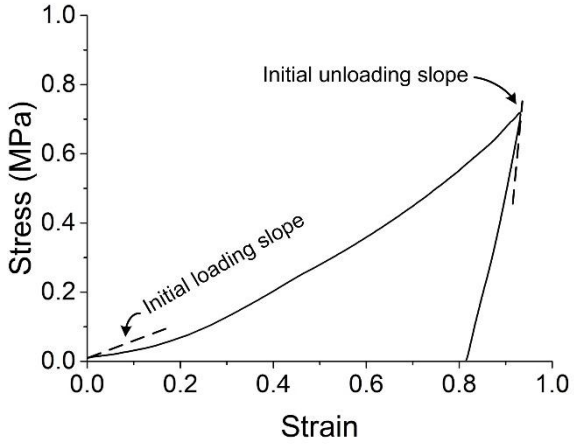

Figure 3.21 An example stress-strain curve for compression tests of CNT forests with initial loading and unloading slopes used for elastic modulus calculations.

CNT forests have very complex internal morphology, with varying CNT diameter, density and alignment through their heights [116, 135], and toward the base, the density and alignment are the worst leading to lower stiffness than the rest of the CNT forest. Since the compression of the whole forest will cause the most compliant parts to compress first, it is not surprising that the initial response to the applied load does not show elastic modulus that is in line with those of CNT microstructures that are much shorter [136]. In fact, the elastic moduli measured are on the order of a few MPa which is consistent with previous studies on indentation of taller CNT forests [104, 137-139]. This leads to implications that for applications requiring high elastic modulus, shorter

CNT microstructure are desirable.

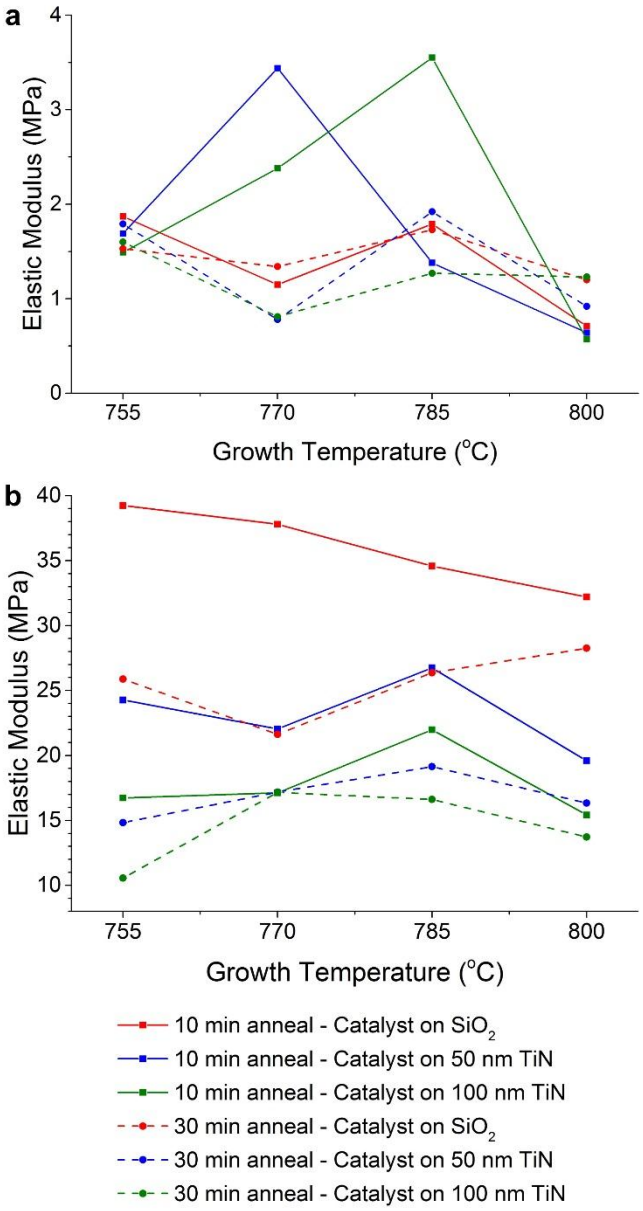

Figure 3.22 Elastic moduli of CNT forests: a) modulus calculated from the initial loading slope, and b) modulus calculated from initial unloading slope.

The elastic moduli measured from the initial loading slope show a decreasing trend as the growth temperature increases, and there is no clear trend regarding temperature or the catalyst stack configuration. The elastic moduli measured from the initial unloading slope decrease as the TiN layer thickness increases and as annealing time increases.

This supports the CNT diameter characterization results as TiN layers cause CNT diameters to be smaller, while the volumetric density remains similar. The differences caused by annealing times can be attributed to the fact that the longer annealing times decrease the volumetric density on average.

Considering CNT forests as foams, the elastic modulus calculated from the initial loading slope should scale as a function of density squared. Indeed, the data follows the general trend when plotted on log-log scale (Figure 3.23). The data does not fall exactly on the trend described by foam mechanics, signifying that the compression mechanics of each CNT forests may vary which is a reasonable assumption since the CNT diameters and alignment are generally different across the CNT forests grown in the parametric study. Other geometrical parameters, such as initial contact area of flat compression grip to the curved top surface of the CNT forests (as shown in Figure 3.5) would have contributed to the scatter of the data as well.

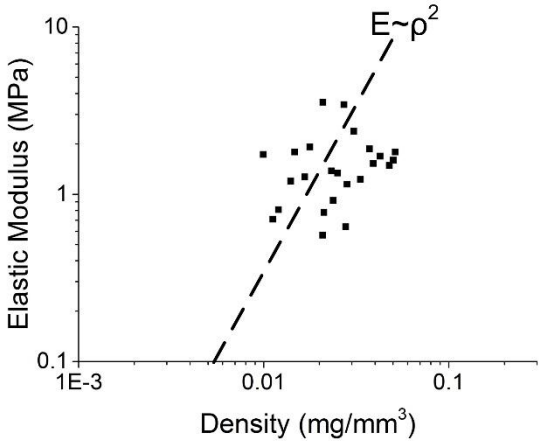

Figure 3.23 Elastic modulus-density map of CNT forests.

3.2.6 Summary of trends

The effects of varying TiN thickness, growth temperature and anneal time on the resulting CNT forests are summarized in table 3.2 below.

Table 3.2 Summary of effect of parameters on the resulting CNT forest properties. ↑ = increases, ↓ = decreases, - = no clear trend. *Elastic modulus is more strongly correlated to the density of the CNT forests.

List of parameters	**↑ TiN thickness**	**↑ Growth Temp.**	**↑ Anneal Time**
Growth Rate	↓	↑ (then ↓ for $Fe/Al_2O_3/TiN$)	↓
Relative Growth Rate	↓	↓	↓
Uniformity	↓	↑ then ↓	↓
Areal Density	-	↓	↓
Volumetric Density	-	↓	↓
CNT alignment	↓	↓	↓
G/D ratio	↓	↑ (↓ then ↑ for Fe/Al_2O_3)	↓
Catalyst Particle Height	↓	↑	-
Catalyst Particle Spacing	↓	-	↓
Elastic Modulus* from loading slope	-	↓ slightly	-
Elastic Modulus from unloading slope	↓	-	↓

Using the trends found in this parametric study, the CNT microstructures grown from catalyst on SiO_2 and TiN can be chosen to show a specific trait. The ability to tune the height, quality and density of the resulting CNT microstructures via engineering the catalyst stack will enable usage of these structures in applications requiring specific material properties. Moreover, only one ‘growth’ step is required to produce the microstructures with tunable multiple height scales, which will enable new devices and material structures exploiting architectures that were impossible/uneconomical to produce in the past.

3.3 CNT microstructures with complex trajectories

3.3.1 Growth of curved CNT microstructures by growth rate modulation

Next, curved CNT microstructure growth was achieved on compound catalyst/underlayer patterns using the growth rate modulation principles. If a continuous microscale catalyst pattern is placed partially on SiO_2 and partially on TiN, the differential growth rates induce stress within the CNT microstructure as it grows. For example, as shown in Fig. 3.24a and 3.24b, a CNT microstructure grown from a square catalyst pattern with half of its area on the TiN layer bends toward the side which is upon TiN, due to the difference in growth rate of the coupled halves of the structure. The stress is transferred between contacting CNTs at the boundary region via mechanical entanglement and van der Waals interactions among the CNTs. Depending on the curvature and length of the structures, slanted microstructures (Figure 3.24a), or arches (Figure 3.24b) can be fabricated. Because the local interaction and differential growth rate determines the trajectory of each structure, large arrays with nearly identical anisotropic shapes can be produced as shown in the SEM images. Importantly, these 3-D structures are fabricated using only two standard photolithography steps, one for patterning the TiN layer, and one for patterning the catalyst layer making this method scalable.

The curvature can be controlled by designing the amount of overlap between the catalyst and the TiN underlayer. This is illustrated in Figure 3.25a and b, which respectively show arrays of round and square cross-section micropillars where the overlap distance is varied from left to right (increments of 5 μm). As expected, the portion of the pillars growing on TiN is always shorter, and as a result, all pillars bend towards the TiN side. As the portion of overlap decreases, the stress induced by the differential growth rate causes increased bending (leading to smaller radius of curvature), reaching a maximum when the catalyst shape is split symmetrically by the TiN layer. With <50% overlap on TiN, the curvature increases gradually until the structure is only slightly curved at the rightmost column of the array. The CNTs are generally tangential to the curvature of the microstructures, similar to the CNT alignment observed in CNT forests.

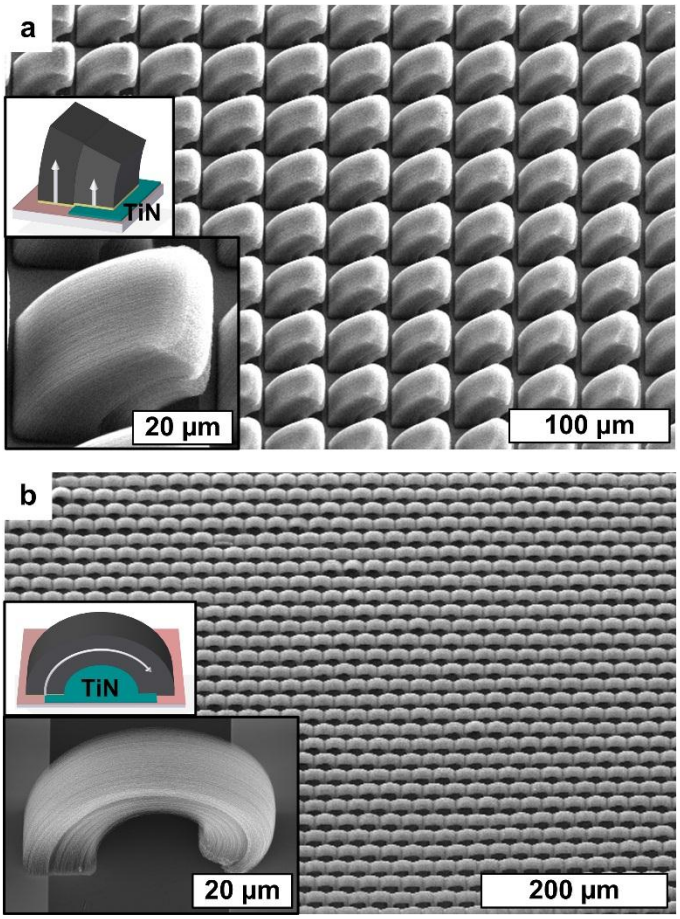

Figure 3.24 Curved CNT microstructures grown on compound catalyst/underlayer patterns: a) slanted microstructures, and b) arch-like microstructures. Insets show the catalyst/underlayer pattern arrangement and close-ups of individual structures.

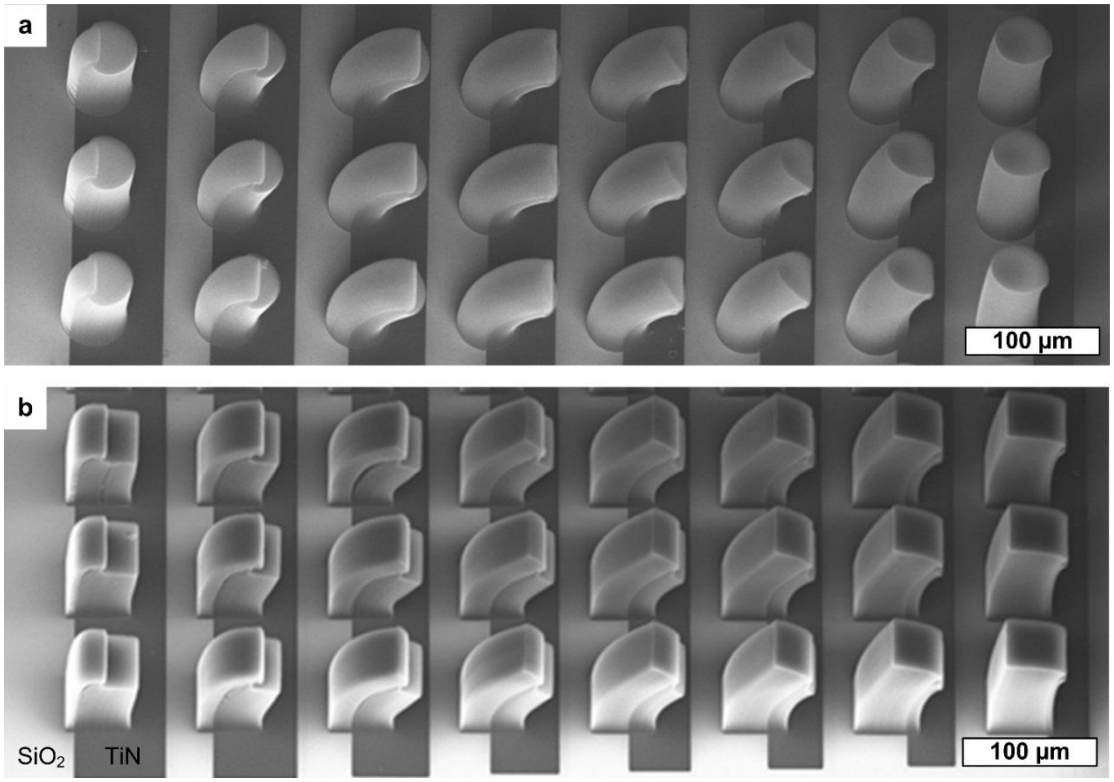

Figure 3.25 Effect on CNT microstructure curvature of catalyst/underlayer overlap ratio. CNT microstructures with a) round, and b) square cross sections are shown.

3.3.2 Complex 3-D microarchitectures

Based on the understanding of the elementary catalyst/underlayer designs that achieve unidirectional bending, a variety of more complex patterns that produce exemplary CNT microstructures having complex trajectories were designed (Figure 3.26). For instance, a compound shape consisting of a "+" catalyst pattern with each arm offset by a rectangular TiN underlayer results in growth of twisted CNT microstructures (Figure 3.26a), resembling macroscale propellers. Similarly, thin semicircular arcs of CNTs can be directed to curve outward by offsetting the TiN underlayer as shown in Figure 3.26b. Further structural complexity is shown by the scrolling of thin offset rectangular patterns (Figure 3.26c). Last, exotic hierarchical arrangements can be formed by the interaction of closely spaced structures, such as the self-organization of offset circular micropillars into wavy patterns (Figure 3.26d) that are reminiscent of macro-scale crochet stitching. This arrangement is hypothesized to have arisen in a collective manner; after the individual structures bend unidirectionally and contact one another,

their continued growth and steric hindrance causes the wavy pattern to form.

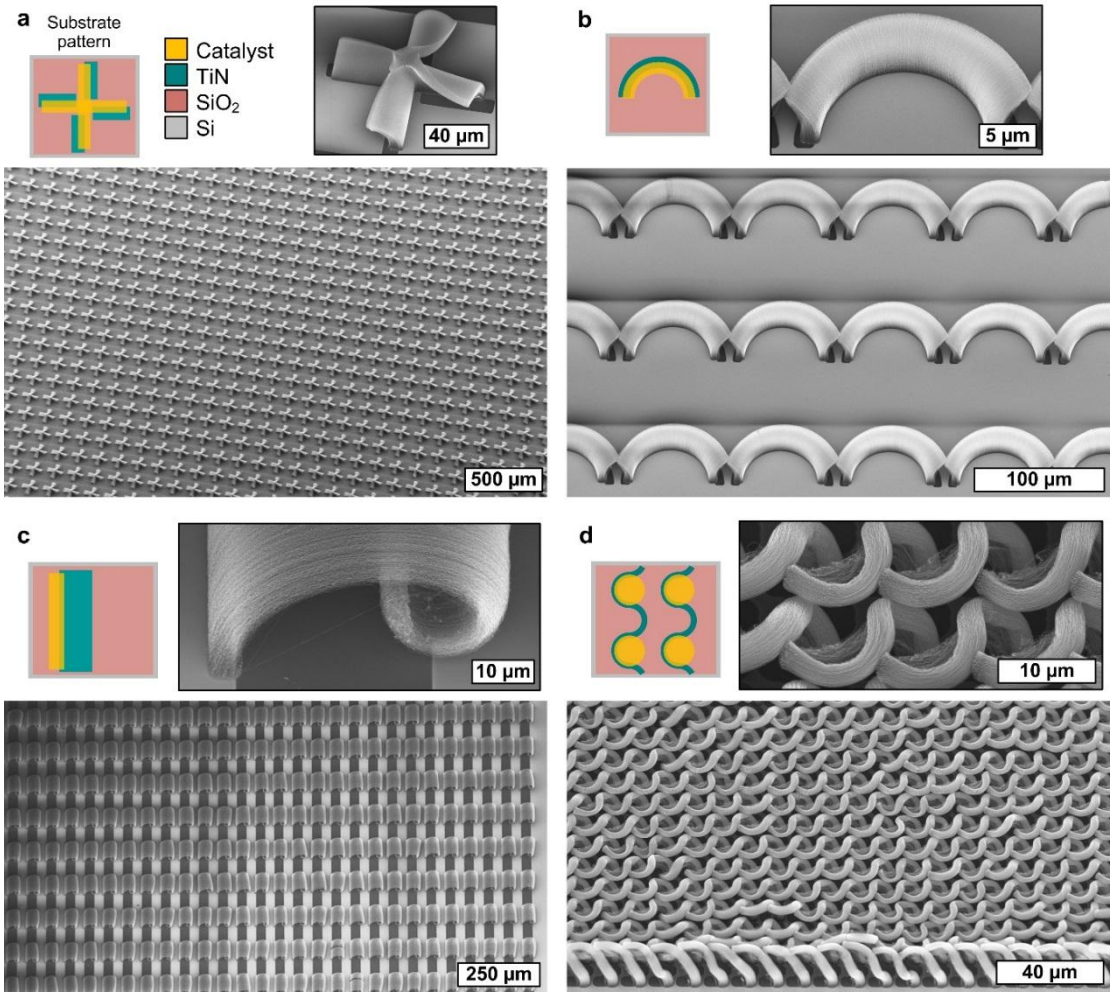

Figure 3.26 A library of complex 3-D CNT microarchitectures enabled by strain-engineering: a) "micropropellers", b) semicircular arc CNT microstructures fanning outward, c) scrolls, and d) CNT micropillars forming a collective wavy pattern.

Notably, in spite of the complex geometries and local deformations, all of these structures can be produced with impressive consistency over large arrays. Arrays of several hundred structures were examined and shown to exhibit nearly identical forms, with defects most frequently arising from debris from catalyst wafer piece preparation process rather than the CNT growth process.

CHAPTER 4

MODELING OF STRAIN-ENGINEERED CNT MICROARCHITECTURE GROWTH

This chapter presents the modeling of the strain-engineered carbon nanotube (CNT) microarchitecture growth. First, the curvature of two-segment square micropillars is approximated by adapting the classical model of a bimetallic beam bending under uniform heating. Next, a finite element method (FEM) framework is developed to simulate stepwise differential growth of the segmented microstructures. The differential growth rate is implemented by assigning initially compressed state on the newly-grown faster-growing segment and then solving for the stresses and deformation. The interfacial delamination strength between the faster and slower growing segments is estimated by calculating the shear stresses at the interface of various lengths. The growth rate, relative growth rate and catalyst pattern dimensions were found to affect the final tip position and were confirmed by experimental evidence.

4.1 Goals of modeling

The coupling of stress and CNT growth rate, via the anisotropic mechanics of the CNT forest [136], is a complex problem. The models developed in this chapter aims to predict the final geometry of CNT microstructures subjected to internal growth rate modulations. Important attributes of the system that need to be reflected in this model are:

1. Different catalyst stacks grow CNTs at different rates.
2. Coupling of CNTs from different catalyst stacks cause them to grow as a single unit.

3. The CNT growth is a sequential process, in which new material is added at the base of the microstructure continuously.
4. The coupled CNTs from different catalyst stacks transfer stress to other parts, and as the result, deforms the microstructure.

The deformation caused by the spatially differing growth rates of CNT microstructures is estimated by considering the fact that different parts are expanding at different rates and calculating a radius of curvature based on the differential growth rates alone. Then an FEM framework is developed where the growth process is discretized and simulated step-by-step to capture the sequential growth of CNTs. After each growth step, where material is added to the model, the faster-growing segment is assigned initially compressed state, then the model is allowed to resolve to better emulate the differences in the growth rate. The aim of the modeling effort is to develop a tool to better understand the stress distribution within the compound structures and hence better predict the final geometry of the strain-engineered structures.

4.2 Analytical estimation of CNT microstructure curvature

A bi-metallic strip undergoing uniform heating is a good analogous system as the different thermal expansion of coefficient can be replaced with the different growth rates of the two halves. Then the temperature difference that drives the expansion can be replaced with the growth time, and the model becomes applicable to the stress-engineered CNT microstructure growth (Figure 4.1a). Starting from the classical formulation of the bimetallic strip model [140], the temperature-dependent expansion term is replaced by a differential lengthening term representing the CNT growth rate. Accordingly, the curvature of the compound CNT microstructure is described as:

$$\frac{1}{\rho} = \frac{6\left(\frac{R_1 - R_2}{R_1}\right)(1+\mathrm{m})^2}{\mathrm{w}\left(3(1+\mathrm{m})^2 + (1+\mathrm{mn})\left(\mathrm{m}^2 + \frac{1}{\mathrm{mn}}\right)\right)} \qquad (1)$$

Here ρ is the radius of curvature, R_1 and R_2 are the growth rates (1 denotes CNTs on Fe/Al_2O_3/SiO_2 and 2 denotes CNTs on Fe/Al_2O_3/TiN), and w is the CNT microstructure width. In addition, m and n are defined as:

$$m = \frac{w_2}{w_1} \quad (2)$$

$$n = \frac{E_2}{E_1} \quad (3)$$

where w denotes the width and E denotes the respective elastic moduli of the segments . The value of n is specified as 0.6 which is the ratio of the measured areal mass density of CNTs on the respective underlayers; however, because the elongation of each layer is specified in the model, the output is insensitive to this value. The geometric parameters are defined in Figure. 4.1b.

Using the calculated curvatures, and the weighted average growth rate, the shapes of the resultant CNT microstructures were visualized using Matlab. The simulation results correspond to the rows of structures in the SEM image Figure 4.1a. To compare the experiments to the simulation, the tip position was characterized in horizontal and vertical axes, normalized to the base dimension (w), as shown in Figure 4.1b. For both the experiment and simulation, the x position of the tip reaches its maximum at 0.4 overlap, and the y position reaches its minimum at approximately 0.6-0.7 overlap (Figure 4.1c).

The differences between the predicted and calculated displacements arise because the model does not capture the exact kinetics of CNT growth, which varies with time. Moreover, it cannot consider how the stress between the two portions of the structure, which are idealized as perfectly coupled without slip, influences the deformation. CNT forests have anisotropic mechanical properties, with the lateral stiffness (perpendicular to the CNT alignment) typically much less than the axial stiffness [141], therefore in principle favoring greater deflection due to built-in stress gradient. Local wrinkling and buckling of the CNTs in the compound microstructures indicates that the growth stress

causes complex mechanical deformations, which cannot be captured by the bi-material deflection model. Moreover, assumptions of bimetallic beam bending model states that a planar cross section stays planar after deformation, which is not necessarily satisfied in the growth of curved CNT microstructures as they do not satisfy the slenderness requirement that the height of the structure be much larger than the base dimensions.

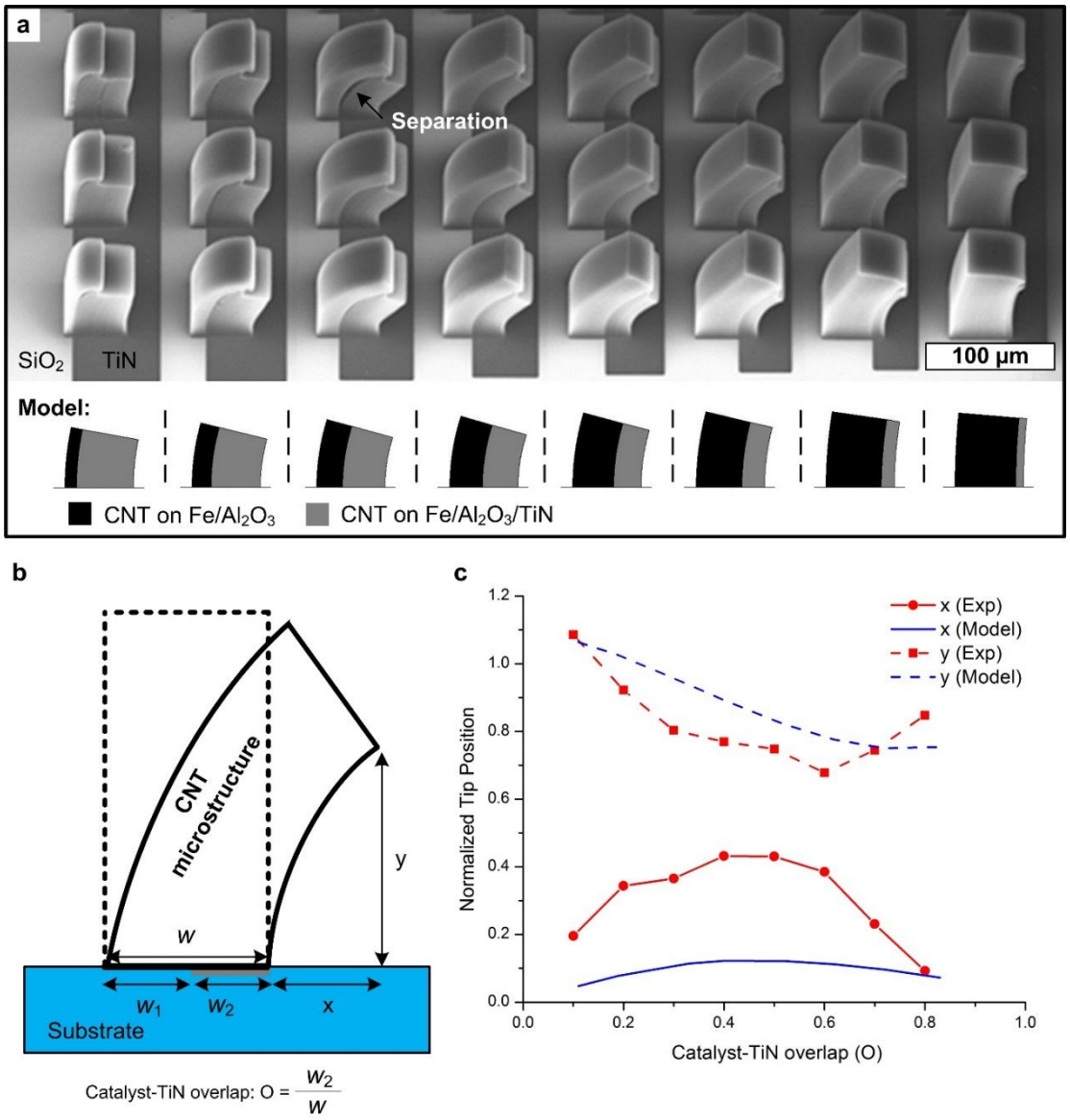

Figure 4.1 Analytical estimation of strain-engineered CNT microstructure curvature and comparison to experimental results. a) Geometric comparison of simulation using calculated curvature and the experiment b) Geometric parameters used in the simulation c) Comparison of normalized tip position between simulation and experiment as a function of catalyst-TiN overlap.

4.3 Modeling of stress-engineered CNT growth using FEM

4.3.1 Model setup

4.3.1.1 Simulation framework

A more rigorous simulation, which considers the anisotropic mechanics and enables modeling or arbitrary shapes was developed using Finite Element Method (FEM). A step-by-step growth scheme was employed to capture the physics of the 'growth' process.

1. Prescribe catalyst area and growth rate.
2. Translate the existing CNT microstructure and define newly grown portion beneath it.
3. Prescribe an initial compressive stress state for the faster growing portion.
4. Solve the entire structure to calculate the geometry of the CNT microstructure at this time step. Keep the residual stress within the structure.
5. Repeat steps 2-4 until desired growth time is met.

This scheme was implemented for three-dimensional (3-D) structures using an FEM software (Ansys 14.5 Mechanical APDL). By using FEM, the effect of material property can be built into the simulation as well as the calculation of stresses experienced at the interface and the effect of residual stress at the resolution of next growth step, enabling a more accurate depiction of the strain-engineered CNT microstructure growth. FEM simulations has been used to model CNT growth in an electric field by calculating the electrostatic forces experienced by individual CNTs and catalyst particles [142], but without the feedback of the results into the model to capture the geometric evolution. In fact, model transformation by re-defining the volume via iterative feedback of solutions is mainly done in the context of material removal such as crack growth [143, 144], and its use in the opposite case, material growth, is a fairly unexplored area. Recently, FEM simulation was used to model plant morphogenesis [145] by re-defining and re-meshing the model after each solution step to capture

addition of cellular matter. Here, a similar approach is used to model the growth of CNT microstructures in this section. The newly grown portion is added at the base of CNT microstructure, and the faster growing region is prescribed to expand vertically, to simulate growth. The model is then solved, and the resulting geometry and stress distribution is used as the start of the next iterative step.

The simulation was set up with mapped mesh using the 'SOLID 186' element. At each time step, a newly grown portion is added, then the faster growing portion is assigned an initially stressed state with a compressive stress. For example, to simulate a growth rate ratio of 2:1, the faster growing portion was assigned an initial compressive stress in the vertical direction that will cause 100% expansion in the vertical direction once the simulation is solved. Due to the nature of using the initially stressed state to model growth, linear elastic material properties were assumed, such that there is no confounding effect from plasticity on the growth process prescribed by expansion of compressed material. CNT microstructures undergo local buckling at ~5% compressive strain [146]. After resolving each step, the CNT axis is rotated toward the slower growing side, hence the elemental coordinate system is adjusted accordingly.

4.3.1.2 Material properties

The CNT forest is modeled as transversely isotropic material with the plane of isotropy parallel to x-z plane, with the CNT axis direction initially along the y axis. This anisotropy arises from the fact that CNTs have intrinsically anisotropic mechanical properties as they are hollow tubular molecules that can be approximated as slender beams, and the fact that the CNTs are vertically aligned in a CNT forest. The material properties measured in chapter 3 have been used (measured from CNTs grown at 800 °C on SiO_2 and 100nm TiN). Recently, a collaboration with Maschmann *et al.* enabled the identification of the anisotropic mechanical properties. The anisotropy of CNT microstructure modulus in compression can range from 4-100 [136, 147], hence the anisotropy value in this range will be used for properties parallel to the CNT axis and those perpendicular to it. The shear modulus G_{xy} can vary from 1-13.3 MPa for CNT microstructures used in this test [136, 148]. In other directions, G_{yz} was assumed to be the same as G_{xy} as the same inter CNT junction is responsible for resisting the shear

deformation, and G_{yz} was assumed to be an order of magnitude higher than the other directions as in this direction, the shear deformation is resisted by bending of CNTs rather than loose contact between the CNTs. For CNTs on TiN, the ratio of axial elastic moduli (E_{y_SiO2}/E_{y_TiN}) was used to derive the magnitude of other properties. The Poisson's ratios of the CNT microstructures in all directions are all assumed to be zeroes. Although Poisson's ratios in compression have been reported [136], their exact values will depend on the CNT orientation and arrangement as well as the direction of loading, and in a simplified model of straight and parallel CNTs in an array, they are all zeroes. This is appropriate in view of CNT material growth where the material extends in the axial dimension without any changes in the lateral dimensions.

CNT microstructures have an inherent stiff network at the top of them, arising from the initial crowding of CNTs before they collectively lift off from the substrate [13, 14]. This layer is called a 'crust'. This crust layer is considerably stiffer [149] than the rest of the microstructures, due to the randomly oriented and tangled CNTs that compose this layer. The crust is modeled as an isotropic material which is much stiffer than the rest of the CNT microstructure. The Poisson's ratio of CNT sheets can vary widely from a negative value to a positive value, depending on CNT composition as well as the alignment [150]. The representative material properties used in this simulation is shown in Table 4.1. It should be noted that these values can vary depending on the growth reaction conditions.

Table 4.1 Material properties of CNTs used in FEM simulation.

Material Property	**CNTs on Fe/Al_2O_3**	**CNTs on Fe/Al_2O_3/TiN**	**CNT Crust**
Ex	0.18 MPa	0.14 MPa	250 MPa
Ey	0.71 MPa	0.57 MPa	250 MPa
Ez	0.18 MPa	0.14 MPa	250 MPa
Gxy	1 MPa	0.8 MPa	96 MPa
Gyz	10 MPa	8 MPa	96 MPa
Gzx	1 MPa	0.8 MPa	96 MPa
$\nu_{xy,}$	0	0	0.3
ν_{yz}	0	0	0.3
ν_{zx}	0	0	0.3

4.3.2 FEM simulation results

4.3.2.1 Stress distribution within segmented CNT microstructures

When a single catalyst patch overlaps SiO_2 and TiN underlayers at the same time (compound structures), the faster and slower growing segments affect each other by transferring stresses though the interface. A compound structure with rectangular patches of TiN spaced evenly was grown to observe the effect of the stress transfer. The growth rates of the two portions have been matched by the boundary conditions, and the CNT microstructure shows differing CNT alignment in the fast and slow growing segments. In Figure 4.2 the CNTs grown from catalyst on TiN appear to have greater vertical alignment influenced by the interface with the faster-growing region. On the other hand, the CNTs grown from catalyst on SiO_2 are less aligned, due to the retarding force from the slower-growing mating segments, and have buckled locally in many locations. This signifies that the structures carry significant residual stresses after being grown, which is sometimes large enough to cause failure. These observations motivate a study of stress distribution within the strain-engineered microstructures, to understand the stress transfer between segments during growth and to devise strategies to reduce residual stresses and produce robust, contiguous structures.

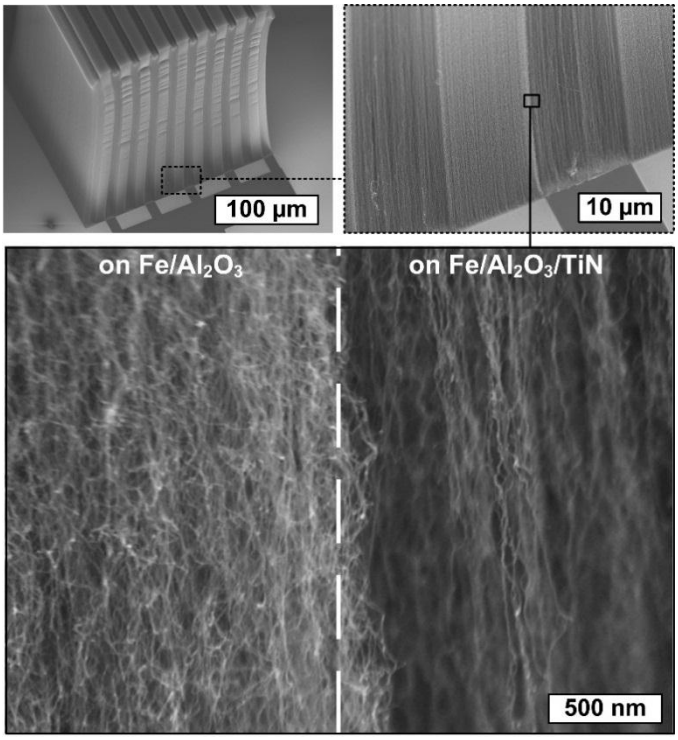

Figure 4.2 CNT alignment in a compound microstructure. Faster- and slower-growing segments affect each other by stress transfer through the interfaces.

As the CNT growth begins, the faster- and slower-growing segments impart forces on the crust layer that is initially formed. The crust will experience largest Von Misses stress just above the interface between the two portions (Figure 4.3a and b). At the interface of the CNTs on SiO_2 and those on TiN, a shear stress is expected, as the CNTs are connected to each other by entanglement and bundling. The simulation captures this shear stress at the boundary (Figure 4.3c and d). The stress is the highest in the part of the crust between the two portions when the CNTs first collectively lift off from the substrate (~ 0.4 MPa) and increases to ~ 0.65 MPa after 20 growth steps. The structures simulated with stiff crust layer retains flat top surface whereas experimental evidence shows that the top surface is not flat in most cases as shown in Figure 3.25. Simulations performed without the crust layer (Figure 4.4) has closer resemblance to the experimentally grown structures, indicating that the crust layer is not as stiff as previously assumed, at least near the interface.

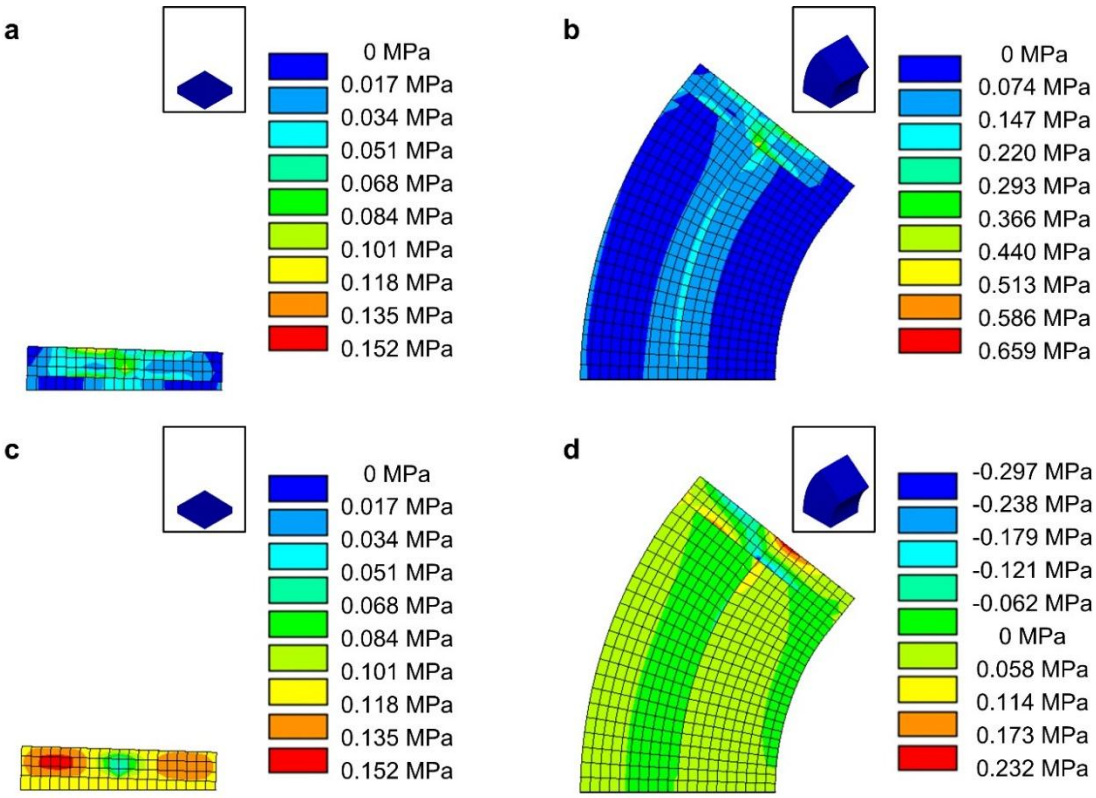

Figure 4.3 Stress distribution within the structure with crust at various stages of growth: a) von Mises stress distribution at initial stage of growth, b) von Mises stress distribution after 20 steps of growth, c) shear stress distribution at initial stage of growth, and d) shear stress distribution after 20 steps of growth. Insets show an isometric view of the structures.

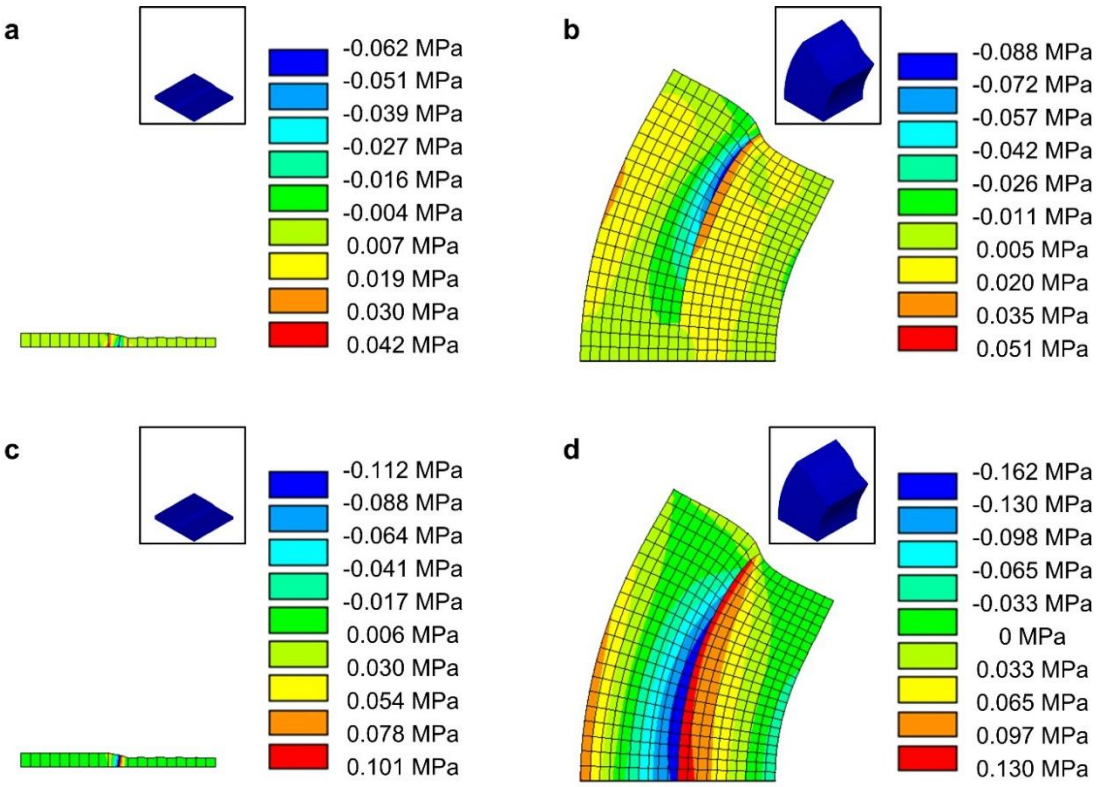

Figure 4.4 Stress distribution within the structure without the effect of crust at various stages of growth: a) shear stress distribution at initial stage of growth, b) shear stress distribution after 20 steps of growth, c) stress (parallel to CNT axis) distribution at initial stage of growth, and d) stress (parallel to CNT axis) distribution after 20 steps of growth. Insets show an isometric view of the structures.

Various ways that the compound CNT microstructures fail either during growth, or upon loading shed some light on the stress distribution within the structures (Figure 4.5). Each segment is subject to both axial stress parallel to the CNT axis and shear stress transferred through the interface. When there is substantial growth rate mismatch between the segments, the shear stress overcomes the interfacial strength which causes the segments to delaminate (Figure 4.5a). The stress parallel to the CNT axis can either be tensile or compressive, depending on the relative growth rates, and may cause local buckling of the CNTs in the faster-growing segments as they are subject to compressive stresses (Figure 4.5b). CNTs are much stiffer in tension [147], hence the counterparts in the neighboring segments do not fail. Structures that have not delaminated nor undergone local buckling of CNTs still carry residual stresses, which causes them to delaminate (Figure 4.5c) and/or (although not shown) buckle upon loading which

intensifies these stresses. The simulations show excellent agreement with the experiments in calculating both the shear stress (Figure 4.4b) and the compressive stress (Figure 4.4d).

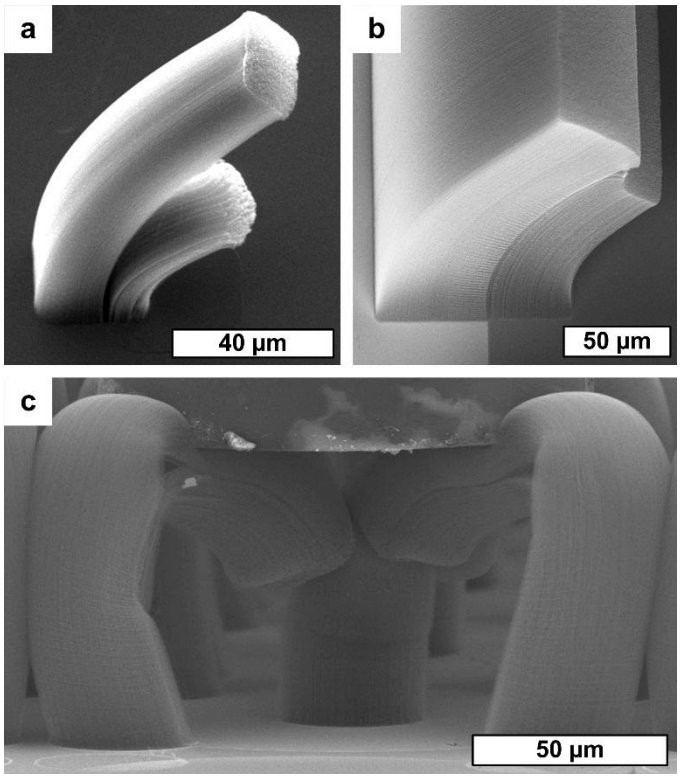

Figure 4.5 Various failure modes of strain-engineered CNT microstructures: a) splitting apart during growth, b) buckling of the faster-growing segment on SiO_2, and c) delamination of the interface upon large compressive deformation.

By increasing the length of the interface between the fast and slow growing portions, the delamination of the structures can be prevented. To show this, checkerboard patterns with alternating TiN (50nm) and SiO_2 underlayer below large catalyst patterns (1024 µm by 1024 µm) were fabricated as shown in Figure 4.6 The side length ratio is defined as the ratio of catalyst pattern side length and TiN square pattern side length, and was varied at 1, 2, 4, 8, 16, 32, and 64. The larger this ratio, the longer the length of the interface. The checkerboard patterns were grown for 5 minutes at 755, 770, 785, and 800 °C. It is shown that the compound checkerboard patterns grow to an intermediate height between the two separate structures on SiO_2 and TiN (Figure 4.7), but grow to closer heights to the structures on SiO_2. As the growth temperature increases, the

relative growth rate ratio of CNTs on Fe/Al_2O_3 and Fe/Al_2O_3/TiN decreases, leading to increased shear stress at the interface. Checkerboard structures grown at 755 and 770 °C do not delaminate regardless of the side length ratio, whereas those grown at 800 °C delaminate even at the highest side length ratio. Those grown at 785 °C delaminate when the side length ratio is 16 or less. This confirms that a longer interface length will indeed lower the shear stress at the interface, and hence prevent delamination.

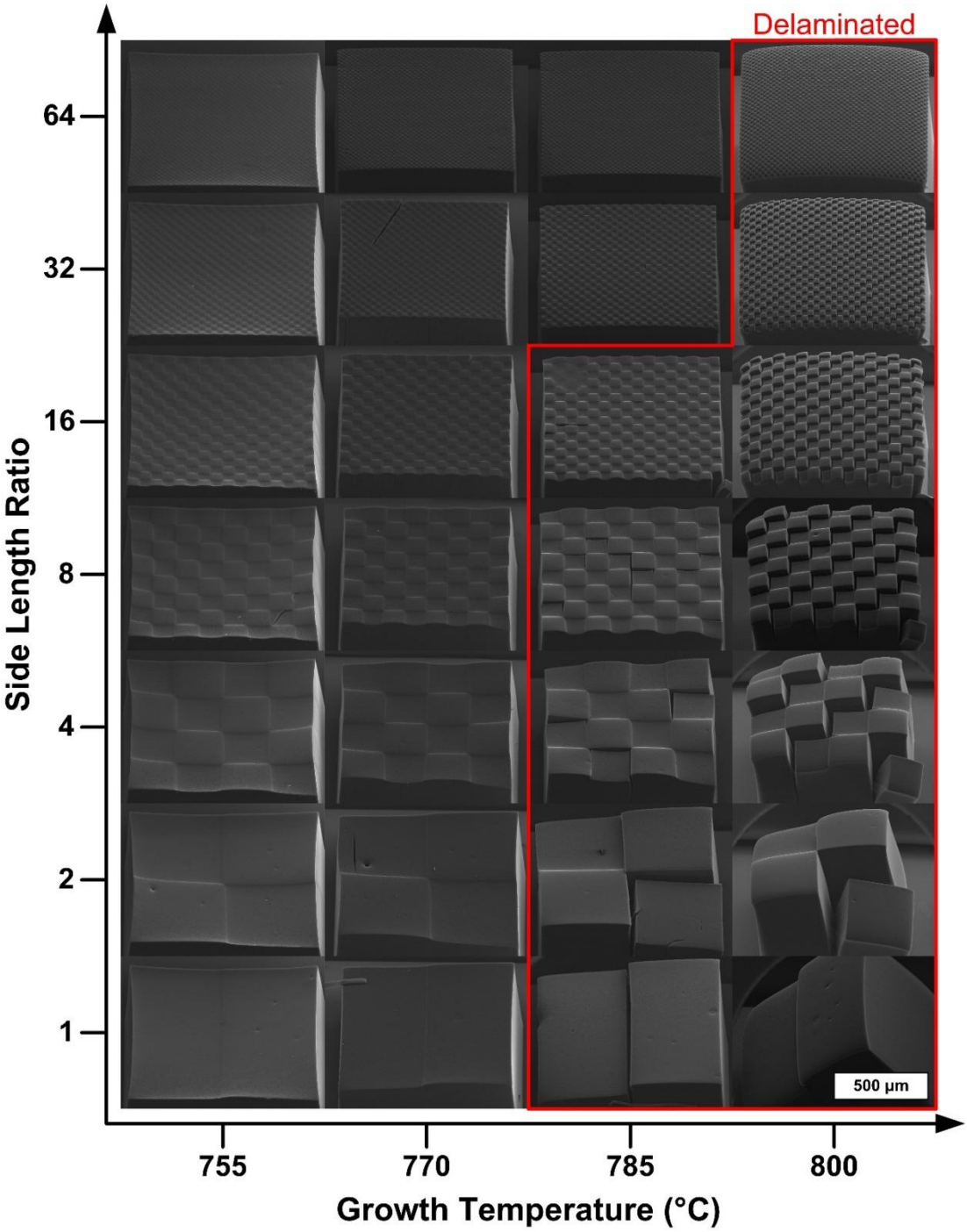

Figure 4.6 Effect of increasing shear stress by increasing growth rate mismatch, and prevention of delamination by increasing the length of interface.

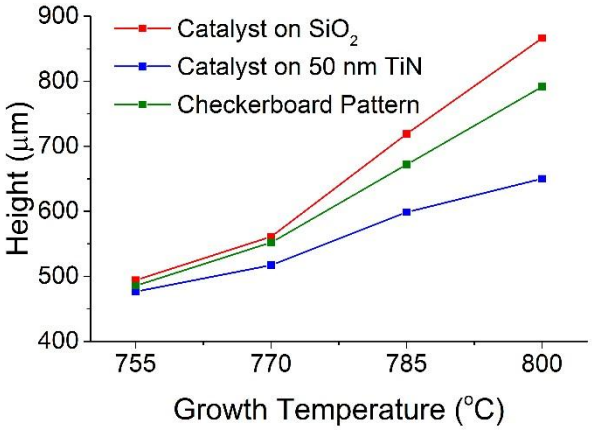

Figure 4.7 Height of CNT microstructures on SiO_2, TiN and compound checkerboard patterns.

Using the FEM model, the shear stress at the interface is calculated and maximum shear stress as a fraction of shear modulus, G_{xy}, is plotted against the growth step number for all growth temperatures in Figure 4.8. The shear stress at the interface is initially high, then drops after a growth step, and gradually increases as CNT growth progresses. Each additional growth step has less and less effect on the maximum shear stress at the interface, and its value tends toward an asymptote. Increasing the growth temperature increases the calculated shear stresses as the growth rate difference is larger, and by examining the experimental results shown in Figure 4.6, the shear strength of the interface can be inferred (Figure 4.8c). The shear strength of the interface is calculated to be $0.048G_{xy}$, and therefore the shear strain-to-failure, 0.048. The dependence of max shear stress on the growth temperature is shown in Figure 4.9. The shear stress at the beginning of the growth (Figure 4.9a) and after 16 growth steps (Figure 4.9b) both show increasing trend as the growth temperature increases. As the side length ratio increases, the shear stress experienced at the interface increases at first then decreases. The decrease in shear stress is expected as the forces causing the shear stress is distributed over a larger area as the length of the interface becomes longer. This opens up the opportunity to create contiguous structures with extreme curvatures. For a given straight interface, a fractal design can be implemented to increase the interface length to prevent delamination as shown in Figure 4.10.

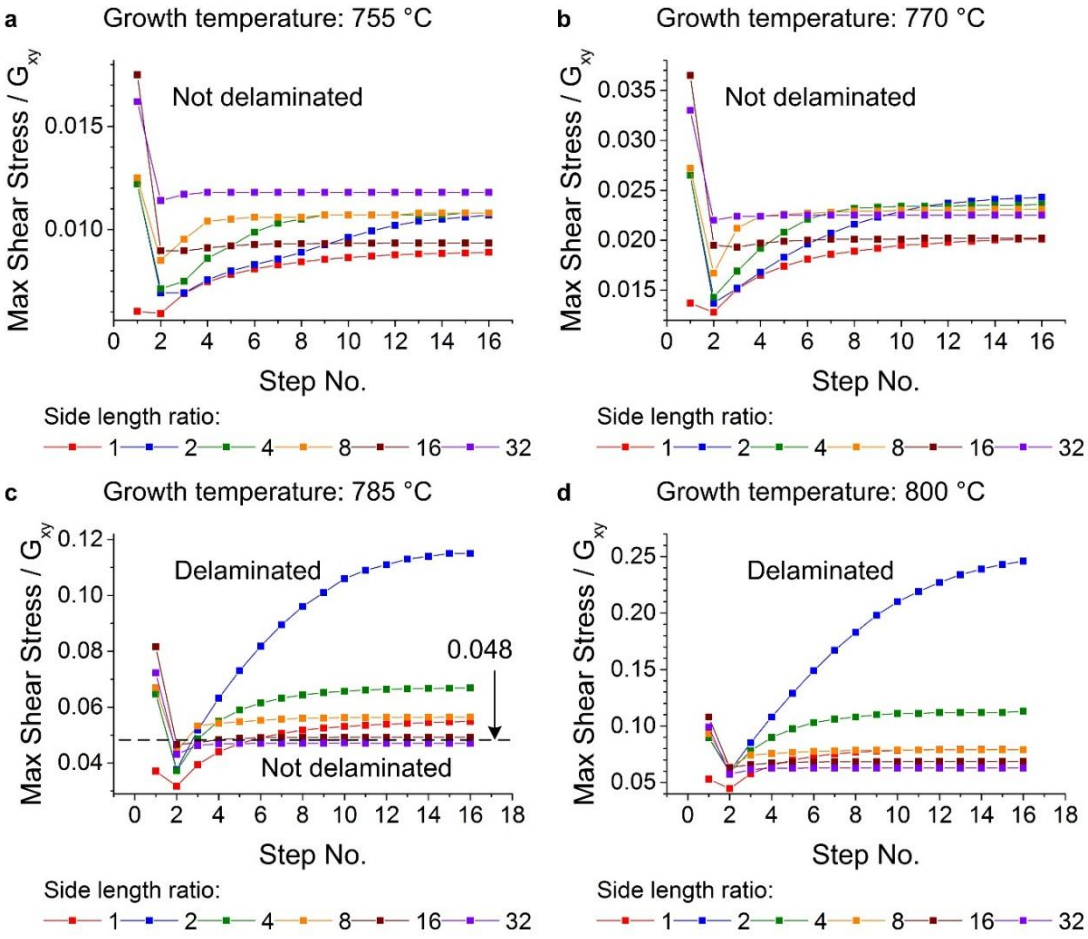

Figure 4.8 Maximum shear stress at the interface between faster-growing and slower-growing segments calculated via FEM simulations. Growth temperatures used in the simulations are: a) 755°C, b) 770 °C, c) 785 °C, d) 800 °C.

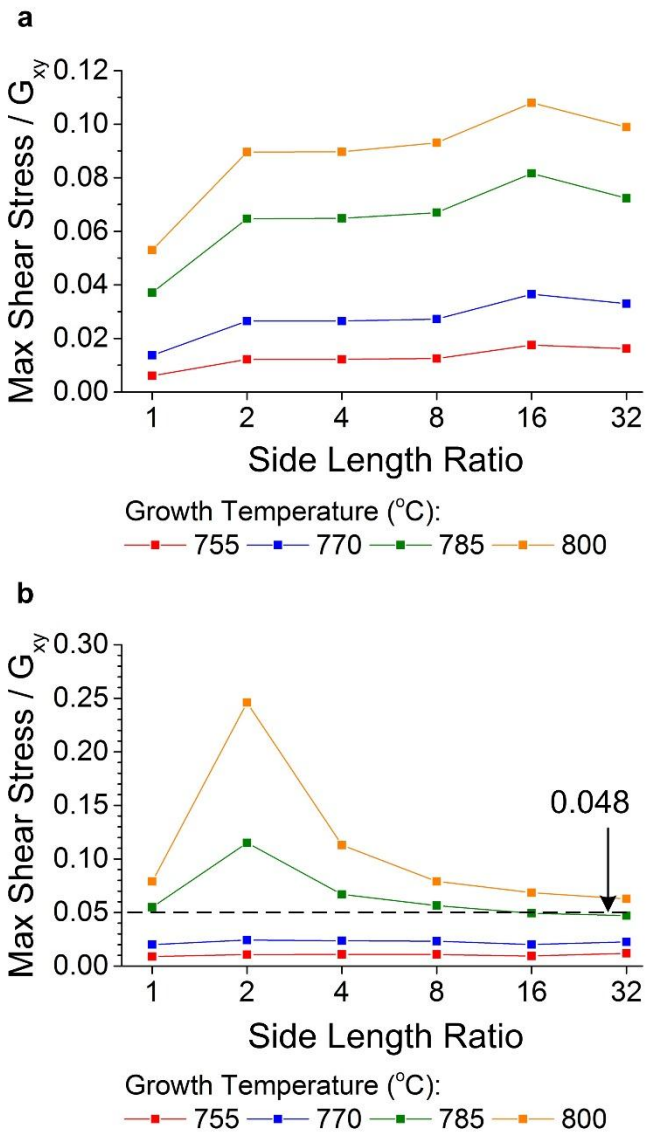

Figure 4.9 Maximum shear stress experienced at the interface of faster- and slower-growing segments: a) at the beginning of the growth, and b) after 16 growth steps. The dotted line denotes the shear strength of the interface.

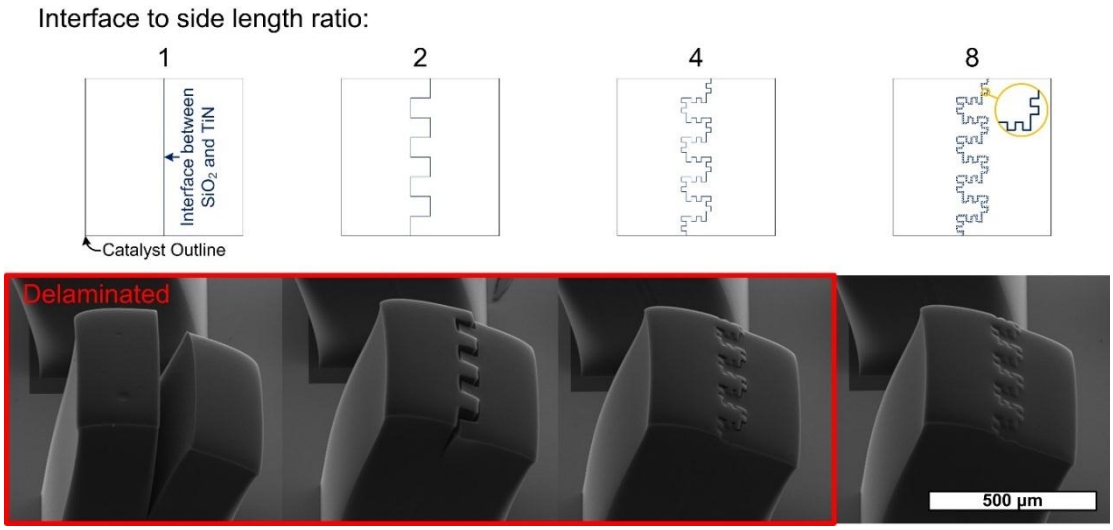

Figure 4.10 Fractal design is employed to increase interface length to prevent delamination of a straight interface.

4.3.2.2 Effect of catalyst-TiN overlap on the final geometry

The results of the FEM simulations are compared against structures presented in Figure 4.1. The FEM models closely resembles the CNT microstructures (Figure 4.11). In order to quantify the similarity, the tip position of each simulated structure is characterized in a consistent manner with 4.1b, and shows a better agreement with the experiments than a simple analytical model presented in section 4.2 (Figure 4.12). There are still discrepancies between the FEM model and the actual structures produced in experiments. This difference arises because in the actual experiments, the structure has delaminated at various places, which is not taken into consideration in the FEM model. Despite the deviations, this comparison shows that the FEM model closely captures the differential growth rate induced deflection of the strain-engineered CNT microstructures.

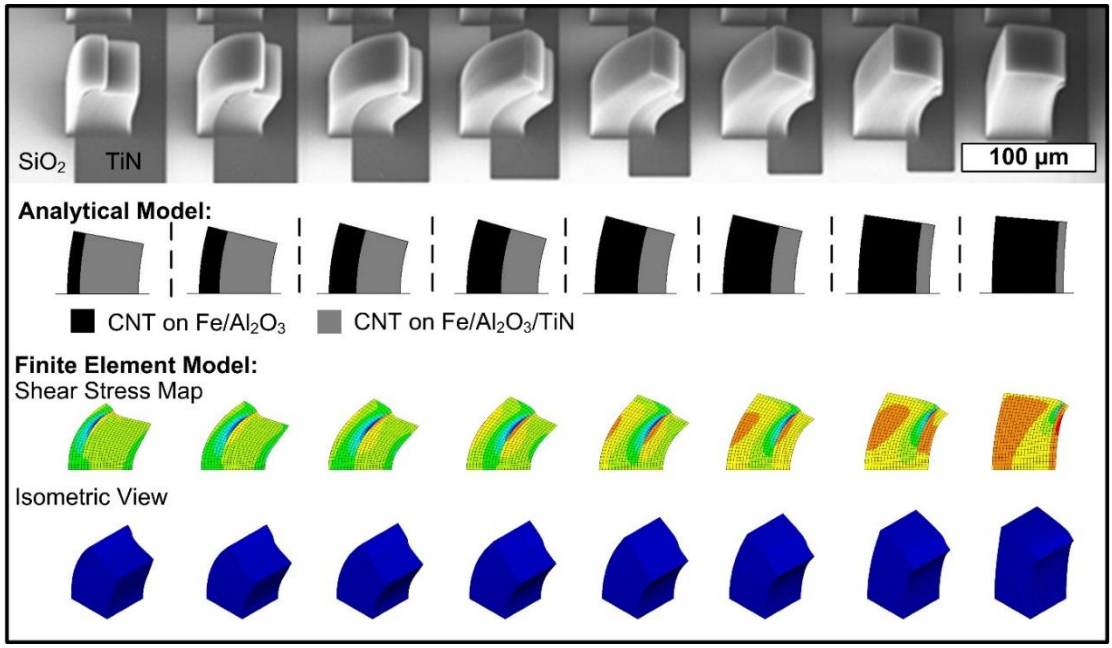

Figure 4.11 Comparison of structures grown in experiments, analytical model and FEM model.

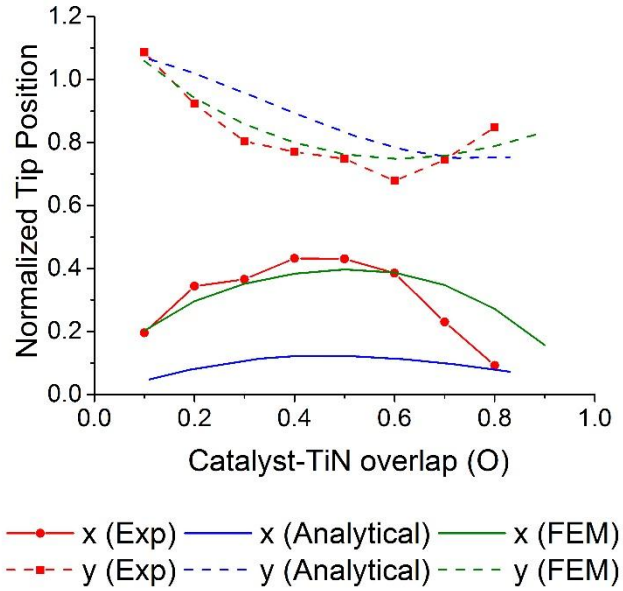

Figure 4.12 Comparison of normalized tip positions of structures grown in experiments, analytical estimation and FEM simulations.

4.3.2.3 Effect of base dimension and relative growth temperature on the final geometry

To design and produce structures with desired geometry, two other parameters can be varied. The base dimension can be controlled by catalyst design much like the catalyst-TiN overlap, and the CNT growth temperature can be controlled by changing the growth recipe. Increasing the growth temperature translates to increasing the overall height, as well as increasing the relative growth rates of the faster-growing portions (section 3.2.1). To validate the model, the CNT growth experiments were performed and compared to the simulation results with the parameters listed in Table 4.2. The FEM model and the actual CNT microstructures are shown below in Figure 4.13. Again, the normalized tip position for CNT microstructures and FEM models show a good agreement (Figure 4.14).

Table 4.2 A list of parameters varied for FEM simulation validation with CNT growth experiments.

Simulation Parameters	**Parameter values used**
Base Dimension (μm)	1024, 512
CNT growth temperature (°C)	755,770,785,800

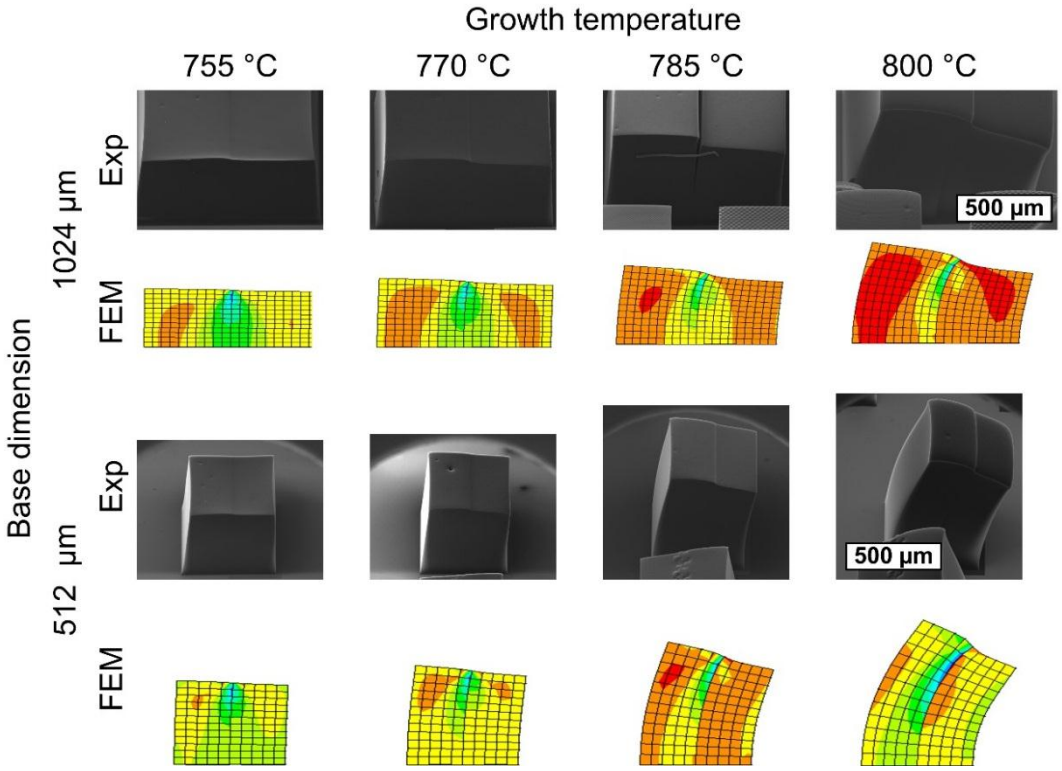

Figure 4.13 Comparison between CNT microstructures and FEM simulations on the effects of base dimension and growth temperature.

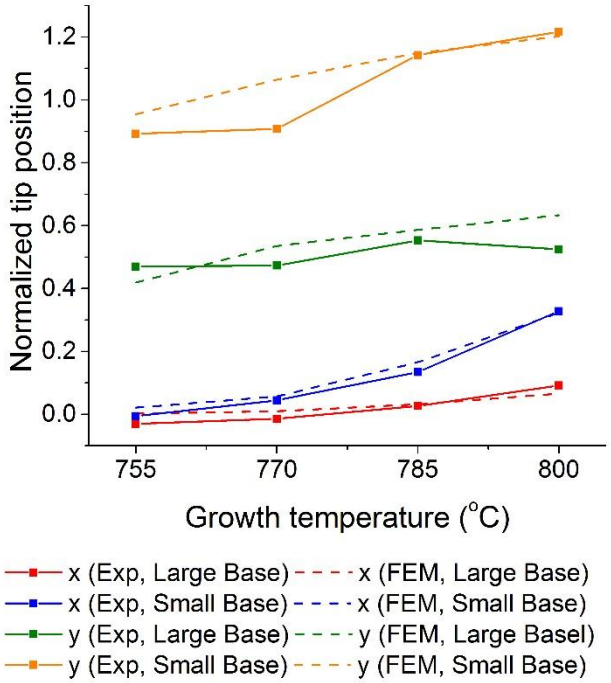

Figure 4.14 Comparison of normalized tip position for CNT microstructures and FEM simulations with varying base dimension and growth temperature.

4.3.2.4 Summary of trends

The differential growth rates cause strain mismatch that leads to internal stresses in the CNT microstructures as they grow. Two failure modes, shear failure at the interface and local buckling of faster-growing segment, have been observed. The FEM model successfully captures these stresses and the contour plots show a good agreement with the experimental evidence. The largest shear stress is observed at the top of the interface, hence the shear failure will progress from the top in most cases. The largest compressive and tensile stress parallel to the CNT axis is experienced at the middle/bottom of the interface, which causes faster growing CNTs to locally buckle. The magnitude of these stresses increase in the structure over time, as the structure grows and more strain mismatch is accumulated.

To enable design of the strain-engineered structures, catalyst-TiN overlap, base dimension and relative growth rates were studied for their effect of the final geometry of the structure. The effects of varying these parameters on the tip position of the structures is summarized in Table 4.3 below.

Table 4.3 Summary of effects of parameters on the final tip position and radius of curvature for simulated strain-engineered microstructures. ↑ = increases, ↓ = decreases.

List of parameters	Normalized tip X position	Normalized tip Y position
↑Catalyst-TiN Overlap	↑ then ↓	↓ then ↑
↑CNT Growth temperature	↑	↑
↑Base Dimension	↓	↓

4.3.3 Simulation of structures multidirectional curvature

Lastly, the capability to simulate more complex structures such as propeller like structures shown in Figure 3.30a is demonstrated. Figure 4.15 shows a good agreement between the structure and the simulation result. The ability to predict the shapes of complex structures with multi-directional curvatures highlights the importance of the model framework as a tool for designing novel geometries via creative catalyst designs.

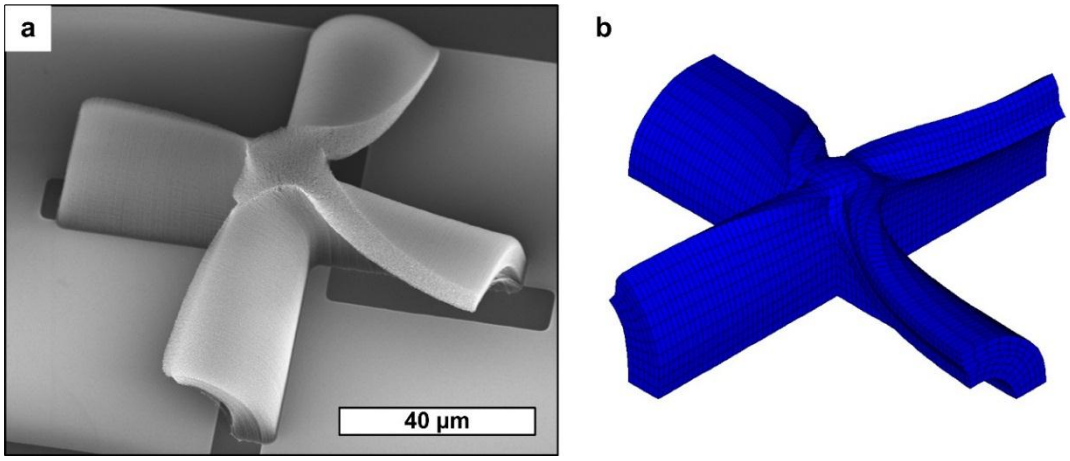

Figure 4.15 Propeller-like structures with multidirectional curvatures. a) CNT microstructure, and b) FEM simulation.

4.3.4 Opportunities for improvement

4.3.4.1 Model framework

The FEM model assumed no delamination or failure of the material occurs in the structures. In reality, the CNT material will fail when subjected to a large stress or strain. This phenomenon can be built into the model to study the evolution of the structure when some of the element in them have failed. The failure of some parts of CNT microstructures during growth has been shown (Figures 4.1a and 4.5) and expansion of the modeling framework to incorporate the failure will improve the correspondence between the model and actual experiments (Figures 4.12 and 4.14).

4.3.4.2 Material properties

CNT microstructure have inherently very complex material properties, because of the variations in the density, arrangement and alignment of CNTs in them. For instance, the alignment of CNTs and their diameter and density change over time as they grow [116, 135]. A more refined model can be developed by studying the spatial variations in CNT microstructures and assigning more accurate material properties accordingly. Aside from spatially varying properties, the properties are non-linear and differ greatly in compression and tension [147], therefore capturing this in the model will improve the accuracy of the model. Also, the effect of mechanical forces on the growth rate should

be studied further. Currently, no effect of forces on the growth rate was assumed, however, the averaging of heights in checkerboard patterns (Figure 3.25) suggest the forces do affect the growth rate.

CHAPTER 5

MECHANICS OF CONFORMALLY COATED CNT MICROSTRUCTURES

Significant portions of this chapter with additional editing are being prepared for publication in: Brieland-Shoultz A., Tawfick S.*, Park S.J.* (* equal contributions), Bedewy M., Maschmann M., Baur J.W. & Hart A.J., Scaling the Stiffness, Strength, and Toughness of Ceramic-Coated Nanotube Foams into the Structural Regime. Advanced Functional Materials, 2014.*

This chapter presents a method to tune the mechanics of carbon nanotube (CNT) microstructures via atomic layer deposition (ALD). First, ALD technique and application on CNTs is overviewed. Next, a wide range tuning of elastic modulus of microstructures is presented. Then tuning of deformation behavior from buckling to brittle failure is investigated, with emphasis on recovery of coated CNT microstructures, relating the transition to the coating thickness.

5.1 ALD of Al_2O_3 on CNTs

CNT microstructures are inherently foams [103], with 1-3% volume fraction filled [104, 151]. Here lies the gap between individually stellar mechanical properties of CNTs and their use in demanding applications. The low volume fraction drives down the bulk properties. However, on the upside, this opens up opportunities to tailor the mechanical properties by filling up the void within the microstructure, with material of choice. On the flip side of the fact that CNTs occupy a very little fraction of the volume defined by the outlines is the opportunity that the CNTs can serve as a scaffold that defines the

volume with large window of property tuning.

In order to fill up the voids within a CNT microstructure, a conformal coating technique is required. ALD is a versatile and widely used conformal coating technique. A common material for ALD is aluminum oxide (Al_2O_3) [152]. ALD consists of a set of two half reactions that are self-limiting, and uses gaseous precursors, such that conformal coating is achieved. The substrate to be coated should have a hydroxyl (OH) group attached to it and from there the reaction starts (Figure 5.1). When CNTs are coated with Al_2O_3, their diameters increase noticeably, highlighting the ability of ALD to penetrate cellular structures such as foams and create conformal coatings (Figure 5.2). Each cycle of ALD deposits a single molecular layer of Al_2O_3. The thickness deposited for each cycle is 1.1-1.3 Å [153, 154], which is much smaller than 3.8 Å Al_2O_3 monolayer thickness. This can be attributed to the fact that the deposition is dependent on the surface chemistry and surface species, and the monolayer thickness is achieved in an ideal scenario.

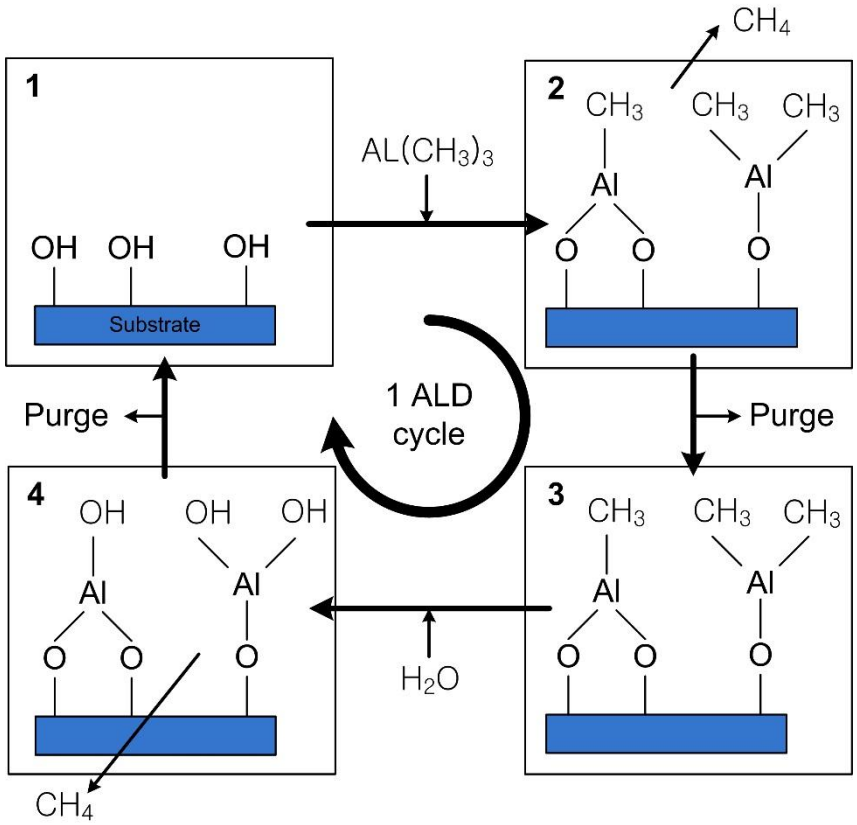

Figure 5.1 Schematic representation of ALD of Al_2O_3.

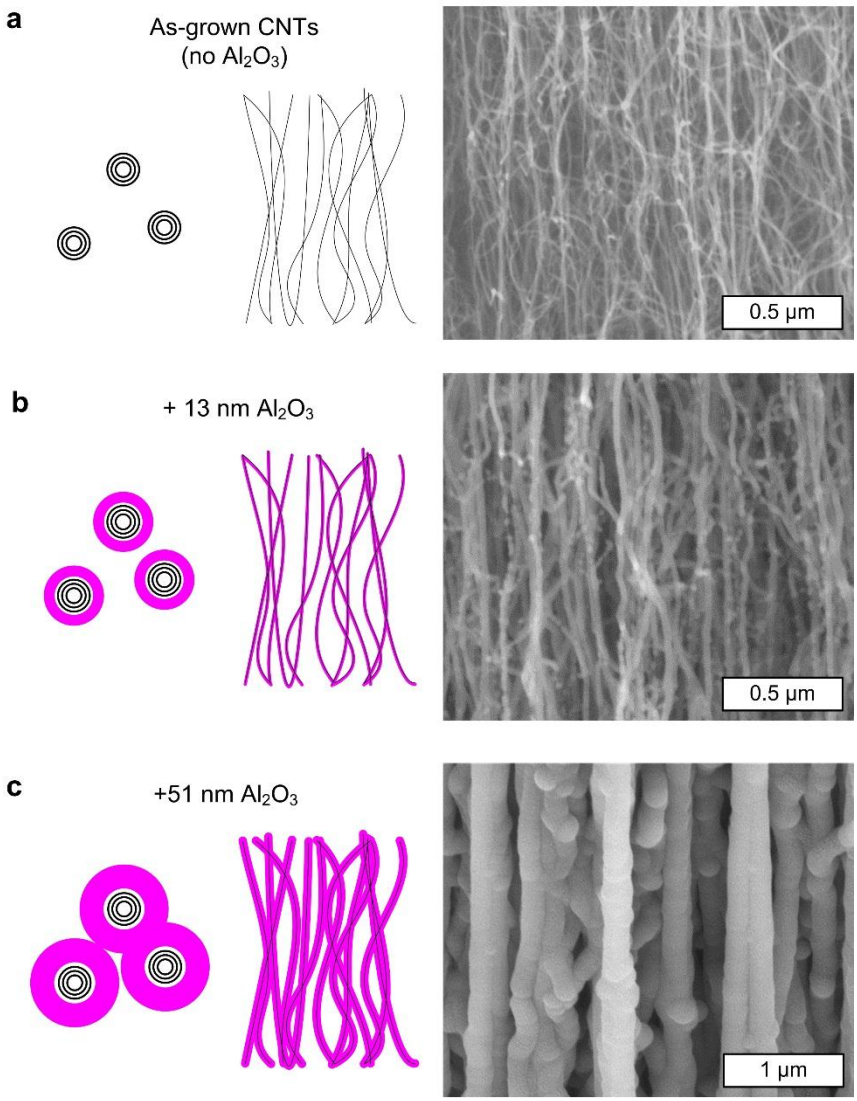

Figure 5.2 Schematic representation of CNTs coated with various thicknesses of Al2O3 via ALD: a) no coating, b) 13 nm, and c) 51 nm.

On CNTs, the Al_2O_3 coating starts nucleating on the defects sites [155] as otherwise CNTs are chemically inactive. Functionalization with NO_2 or nitroaniline has been shown to improve the coating uniformity by providing sites where ALD reactions can be initiated [155-157]. The coating nucleates along the length of CNTs, forming beads of Al_2O_3 (Figure 5.3a) and grows in size upon subsequent cycles. This formation of beads at CNT defect sites has been observed in previous studies [156, 157]. When the Al_2O_3 beads grow big enough to meet each other, then the subsequent cycle will start adding continuous layers on the cluster of beads. Finally, when all of the beads have met, the coating grows as continuous conformal coating (Figure 5.3b-d).

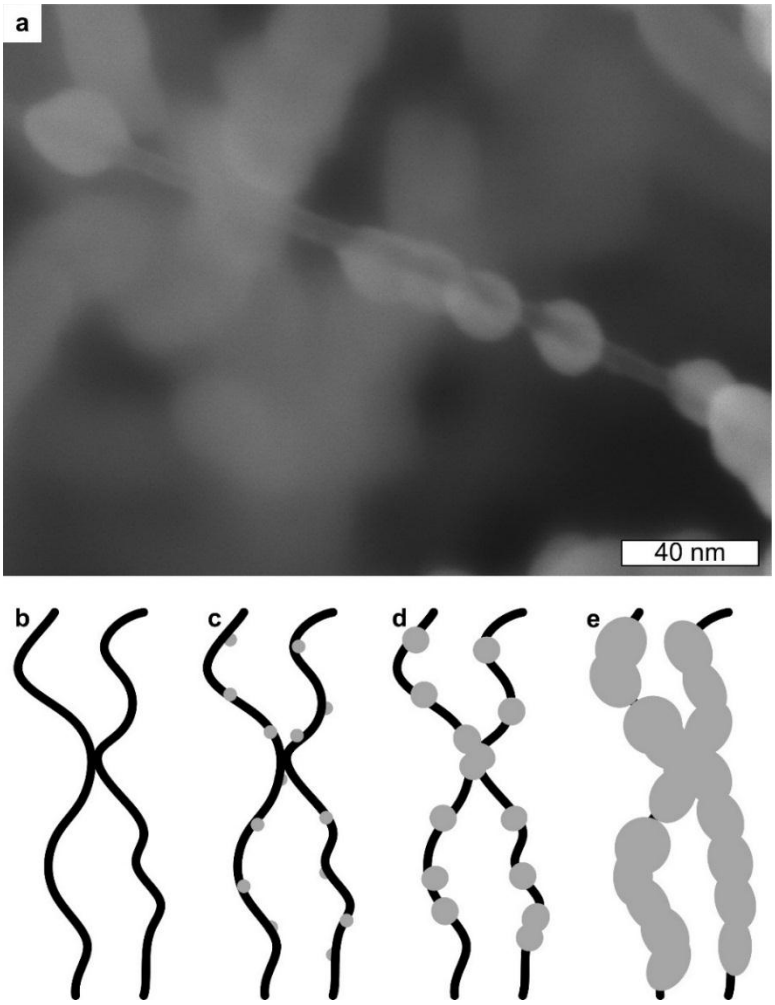

Figure 5.3 Schematic depiction of progression of ALD coating cycles on CNTs. a) Discrete nucleation of ALD coating b) CNTs without coating. c) CNTs with ALD coating initiated at defect sites d) CNTs subjected to ALD cycles beyond nucleation. Al_2O_3 forms microbeads around CNTs. e) CNTs subjected to even more ALD cycles. The coating has grown to include all the Al_2O_3 beads and hence the CNTs have continuous coating on them.

Even though ALD coating is a conformal coating, the gaseous precursors need to reach the nucleation sites on CNTs to initiate coating, and this may not always be possible due to a foam-like arrangement of CNTs in the CNT microstructure. Therefore a CNT 'wall' feature was grown and coated by ALD and the cross section was imaged to examine the coating penetration depth. The penetration depth of ALD coating into the surface of CNT microstructure is found to be 5-7 µm (Figure 5.4a) and indeed a CNT 'wall' with 10 µm thickness is fully infiltrated due to precursors diffusing in from both sides (Figure 5.4b). In order to create a uniformly coated large area CNT structure, a

perforated CNT ‘honeycomb’ structure was grown (Figure 5.4c). Cross section SEM image of the honeycomb structure indeed shows uniform coating.

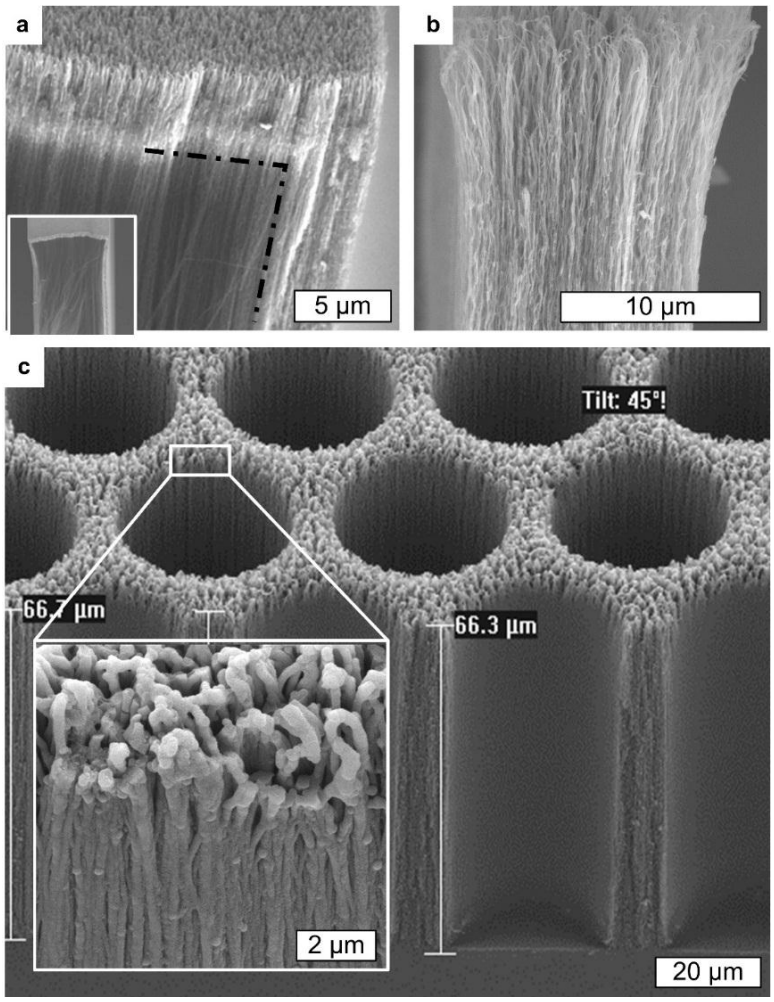

Figure 5.4 Measurement of ALD coating penetration depth into the surface of CNT microstructures. a) Cross section of CNT wall structure coated with ALD. Inset shows an overview. The penetration depth is 5-7 µm. b) Cross section of a CNT wall that is 10 µm wide. The structure is fully infiltrated with ALD coating. c) A honeycomb structure with perforations to allow diffusion of gaseous precursors into the CNT microstructures to achieve uniform coating.

The precursor diffusion in the honeycomb structures is still limited by the aspect ratio of the holes. A set of CNT honeycomb structures with varying hole diameters, but same wall thicknesses were grown to a very tall height (~1 mm) and subjected to 100 cycles of ALD coating to elucidate the geometric limitation of ALD coating (Figure 5.5).

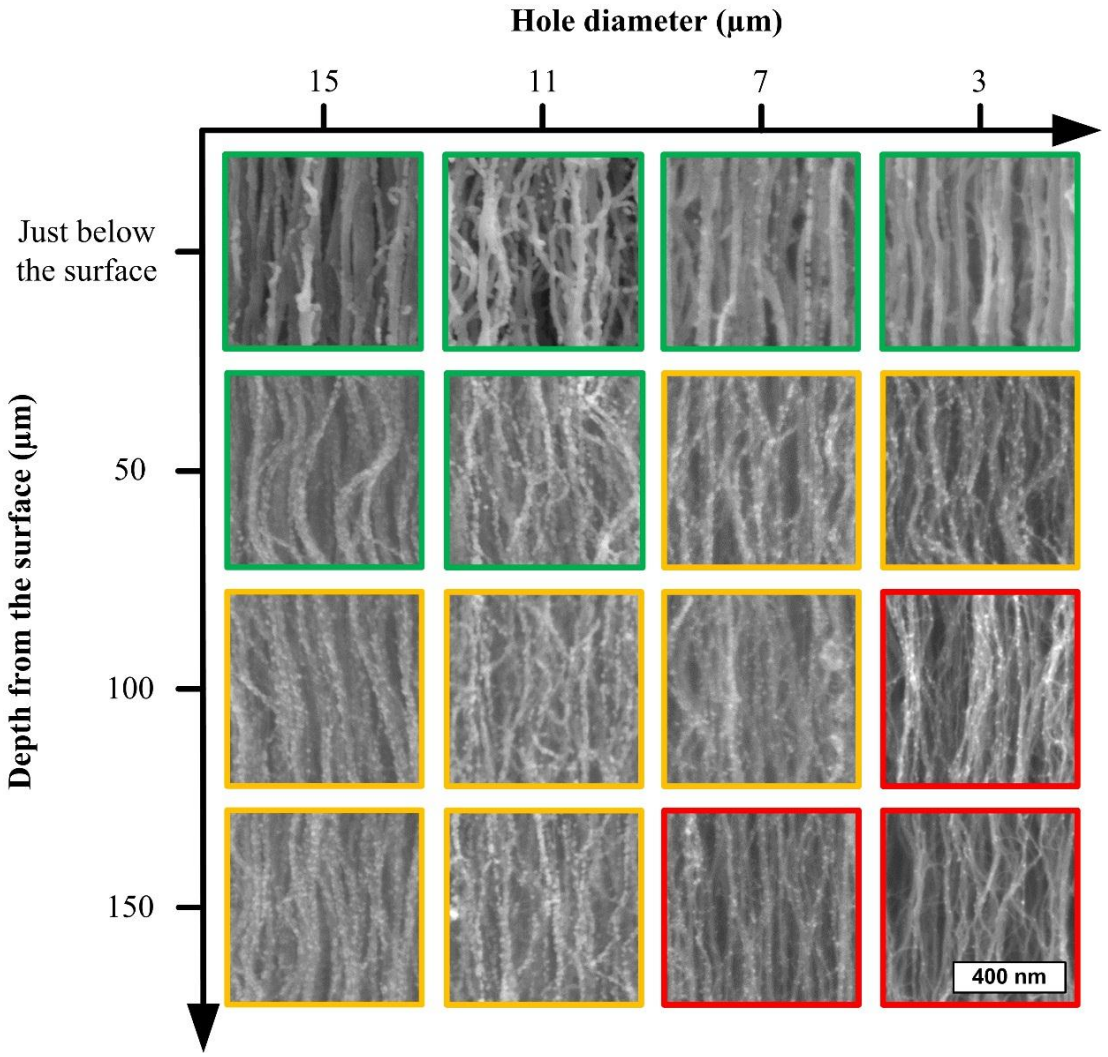

Figure 5.5 Degree of ALD coating depending on the diameter of the hole and depth from the surface of a CNT honeycomb structure. Green indicates continuous coating, orange indicates discontinuous beads on CNTs covering more than ~50% of CNT surface and red indicates less than 50% of CNT surface covered.

For the purpose of classification, coating state which has some sections of CNTs coated by multiple adjoining Al_2O_3 beads will be considered to have 'continuous coating'. Not surprisingly, there is a limit to the aspect ratio of the holes that the ALD coating will penetrate to produce continuous coating, and the ratio is roughly 5. This suggests that there will be a trade off when designing for a structure with maximum stiffness, because in order to ensure uniform coating, the holes need to be larger, which will drive down the cross sectional area that supports the load, reducing the overall stiffness.

Transmission small angle X-ray scattering (SAXS) was used to characterize the

morphology of the as grown and Al_2O_3-coated CNTs by placing the honeycomb structures in the beamline path of a synchrotron X-ray beam and collecting the scattered X-rays on an area detector [115-117, 158] (Figure 3.9). The statistical distribution of outer diameters for both coated and uncoated CNTs were obtained by fitting a mathematical model of poly-disperse core-shell cylinders to line-scans of scattering intensity. This determines the average outer and inner radii of the bare CNTs as 5.0 and 3.5 nm, respectively. The line-scans are obtained by integration of the scattered intensities within a sector of +/- 10° about the axis of maximum intensity on the 2-D scattering pattern, as shown in Figure 3.9. As seen in Figure 5.6a, the peak corresponding to the scattering from the population of Al_2O_3-coated CNTs shifts to a lower value on the x-axis with increasing coating thickness. This indicates a significant increase in the size of the scatters, which is quantified by fitting the data for coated samples with a core-shell scattering model. Analysis of the coated samples gives average coating thickness of 8.5, 14.5 and 26.7 nm for 50, 100 and 200 cycles of ALD, (Figure 5.6b). For 100 and 200 cycles, a second peak on the SAXS linescans is seen at a q value higher than the form-factor peak. This peak could arise from the observed roughening of the Al_2O_3 layer at the greater coating thickness (Figure 5.3b-d).

The average coating thickness was also estimated by measuring the weight of the samples before and after ALD coating. A sub-linear relationship between mass and the number of cycles was found, showing that the deposited thickness per ALD cycle is affected by the ability of the precursors to diffuse into the CNT forest; this reduces as the porosity of the sample decreases when subjected to multiple cycles. Therefore, a model was constructed where the pore size is decreased with each subsequent cycle to predict the thickness deposited by each cycle of ALD. The best fit to the SAXS and weight measurements corresponds to a decrease of effective diffusion coefficient of vapor phase precursors in porous media by 0.5% per cycle, starting at the 140^{th} cycle of ALD coating (Figure 5.5b). There are two main contributing factors: decrease in porosity as the volume is filled up, leading to less diffusion of precursors into the structure, and coalescence of coated CNTs as the coating thickness increases. Improved uniformity of coating could likely be achieved by increasing the precursor cycle duration (steps 2 and 4 in Figure 5.1).

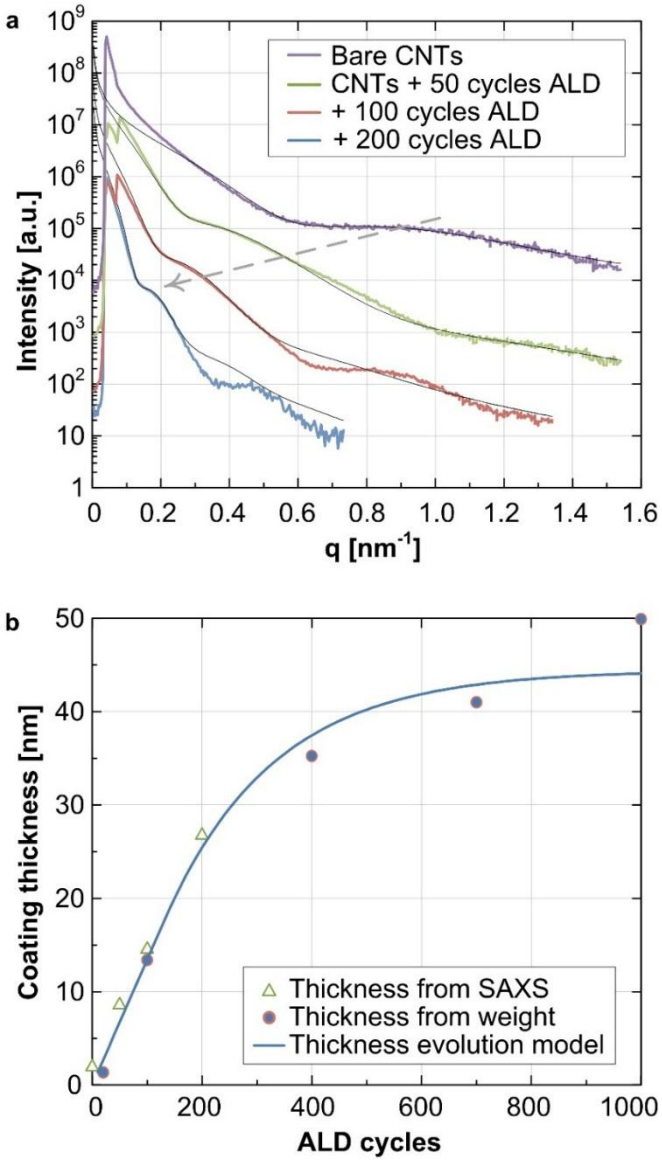

Figure 5.6 Measurement of ALD coating thicknesses on CNTs. a) Line-scans of SAXS on CNT honeycombs with various coating thicknesses b) Comparison between SAXS and theoretical prediction.

5.2 Elastic modulus

Cylindrical CNT microstructure of diameter 20-70 µm were coated with 0, 100, 250 and 1000 cycles of ALD and indented using a nanoindenter at Air Force Research Lab (AFRL). An SEM image of structures tested and example load-displacement curves for 30 µm diameter pillars are shown in Figure 5.7.

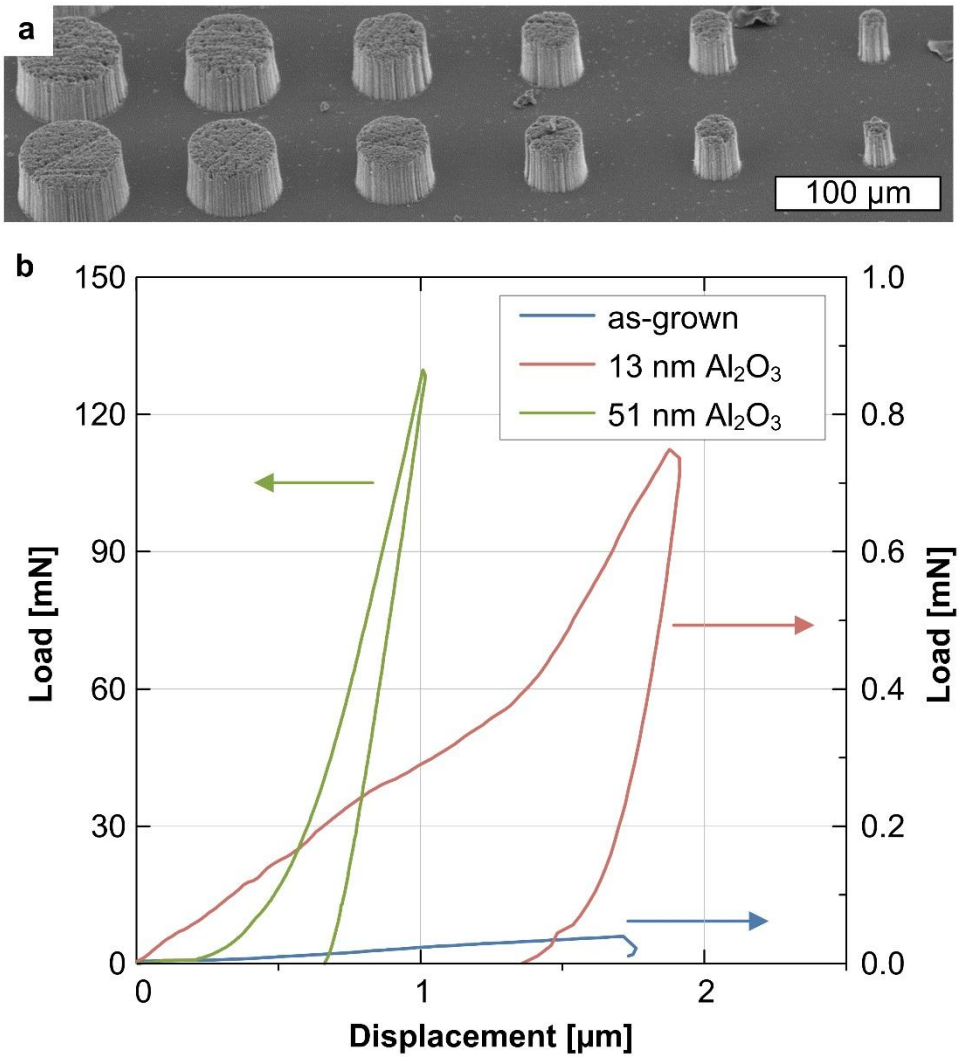

Figure 5.7 Compression of CNT-Al_2O_3 composite micropillars. a) CNT micropillars of 20-70 µm diameters to be tested b) Example load-displacement curves for compression of 30 µm diameter composite micropillars.

As a result of diffusion-limited coating, the elastic modulus of the Al_2O_3-CNT composites depended strongly on the micropillar diameter. The micropillars were tested in axial compression with a cylindrical flat diamond tip (100 µm diameter). The elastic modulus was obtained from the unloading slope in continuous modulus mode (10 nm oscillations at 50 Hz) at a compressive pre-strain of 0.05 (approximately 2 µm compression of the micropillar). The full matrix of compression tests performed is summarized in Figure 5.8. Here, modulus is inversely proportional to pillar diameter, as the reinforcement of larger pillars is limited by ALD penetration and therefore the final composite pillar is a reinforced shell surrounding a soft core of uncoated CNTs.

These trends, and specifically the size-dependent modulus of non-coated pillars, are also attributed to size-dependent growth effects on the density of CNTs within the forest [114, 135]. The CNT micropillars subjected to 1000 cycles of ALD exhibit elastic modulus of up to 70 GPa, whereas the elastic modulus of uncoated and large diameter is lower than 10 MPa, which shows a tuning range of almost 4 orders of magnitude.

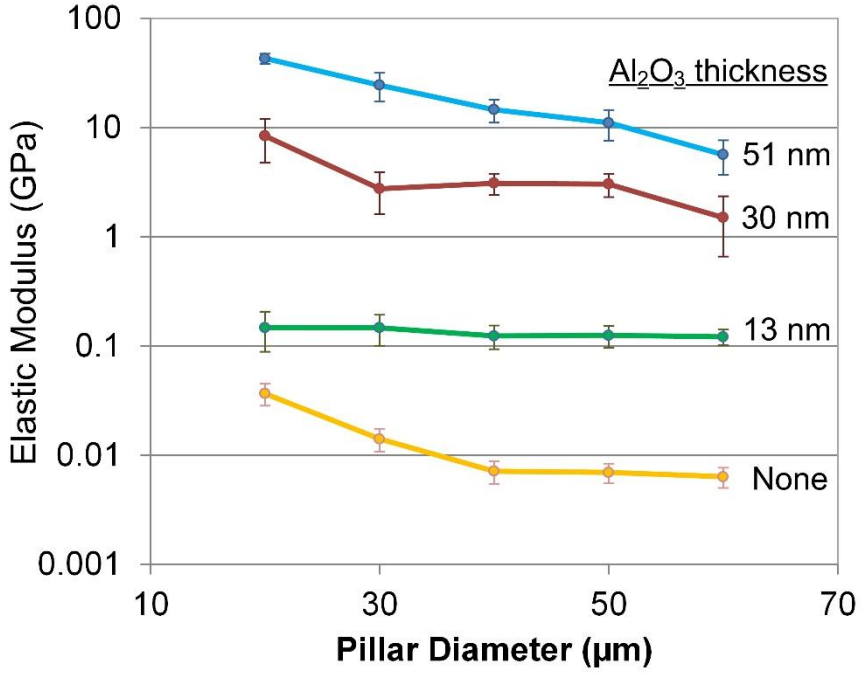

Figure 5.8 Elastic modulus of CNT micropillars coated via ALD.

The elastic moduli and the density of these micropillars are then plotted on an Ashby chart and compared to other materials of similar composition, such as CNT and aluminum foams [159-161] (Figure 5.9). Comparing the scaling behavior to conventional open cell foams, we note that the elastic modulus and strength of the Al_2O_3-CNT composite scale as $E \sim \rho^{2.8}$ (Figure 5.9). Ideal bend-dominated open-cell foams such as open-cell polymer foams [162], and aluminum honeycombs [163] scale as $E \sim \rho^2$ and. The modulus scaling of our ALD-coated CNTs incidentally resembles the elastic moduli of isotropic CNT foams[159], CNT aerogels[164], and Si aerogels [165] which scale as $\sim \rho^3$, and commonly attributed to the interdependence of strut thickness and cell size.

On the other hand, ultralight open-cell foams such as Ni-P microlattices [166] show $E \sim \rho^2$ because of the strut aspect ratio is independent of density. High modulus scaling power (n), as shown by the Al_2O_3-CNT foams, is advantageous because the low-density as grown CNTs can be coated to achieve a comparatively large gain in elastic modulus with increasing density.

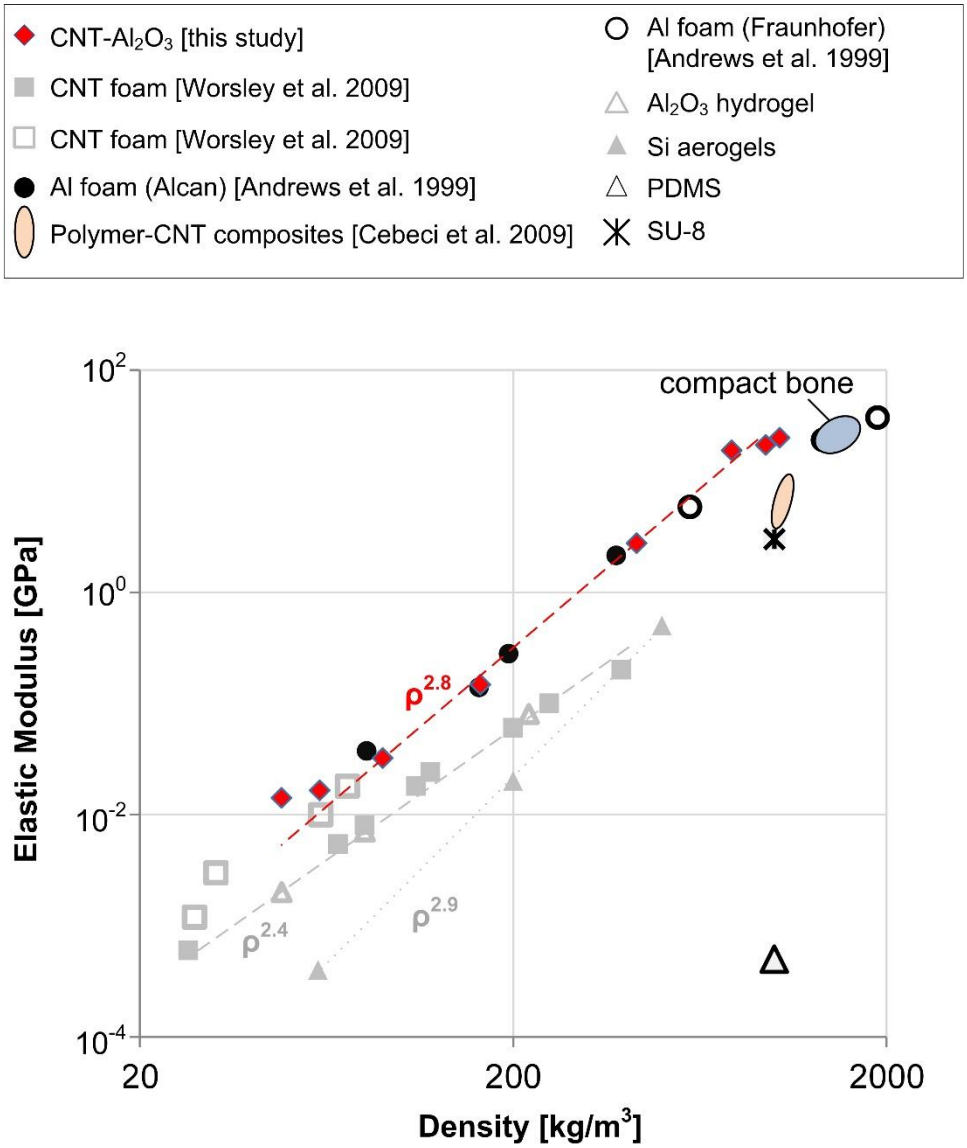

Figure 5.9 Elastic modulus versus density plot of CNT-Al_2O_3 composite foams and related materials. Previously published data taken from [159-161].

5.3 Deformation behavior

Another aspect of mechanical property tuning afforded by conformal coating of CNTs with Al_2O_3 via ALD is the change in deformation behavior. Because conformal coating adds thickness to the individual CNTs within a microstructure, its effect is analogous to changing strut thickness in cellular materials. This changes an important parameter in foam characterization, its relative density which is the ratio of foam density (ρ) to the density of the bulk solid (ρ_s). Foam mechanics [167] suggests that foams undergo buckling dominated compression behavior to yielding dominated deformation behavior as the relative density increases. Therefore, it is reasonable to assume that the deformation behavior of CNT-Al_2O_3 composite foams will also undergo characteristic change. Indeed, 20 μm diameter CNT micropillars grown to ~40 μm coated with 0, 3, 13, 28, 37, 43, 51 nm of Al_2O_3 (0, 25,100, 250,500, 750, and 1000 cycles respectively) show differences in their deformation behaviors (Figure 5.10). The failure mechanism changes from buckling of cell walls at lower coating thicknesses, to brittle fracture after a certain threshold coating thickness. The percentage recovery of induced strain is quantified to show this difference (Figure 5.11).

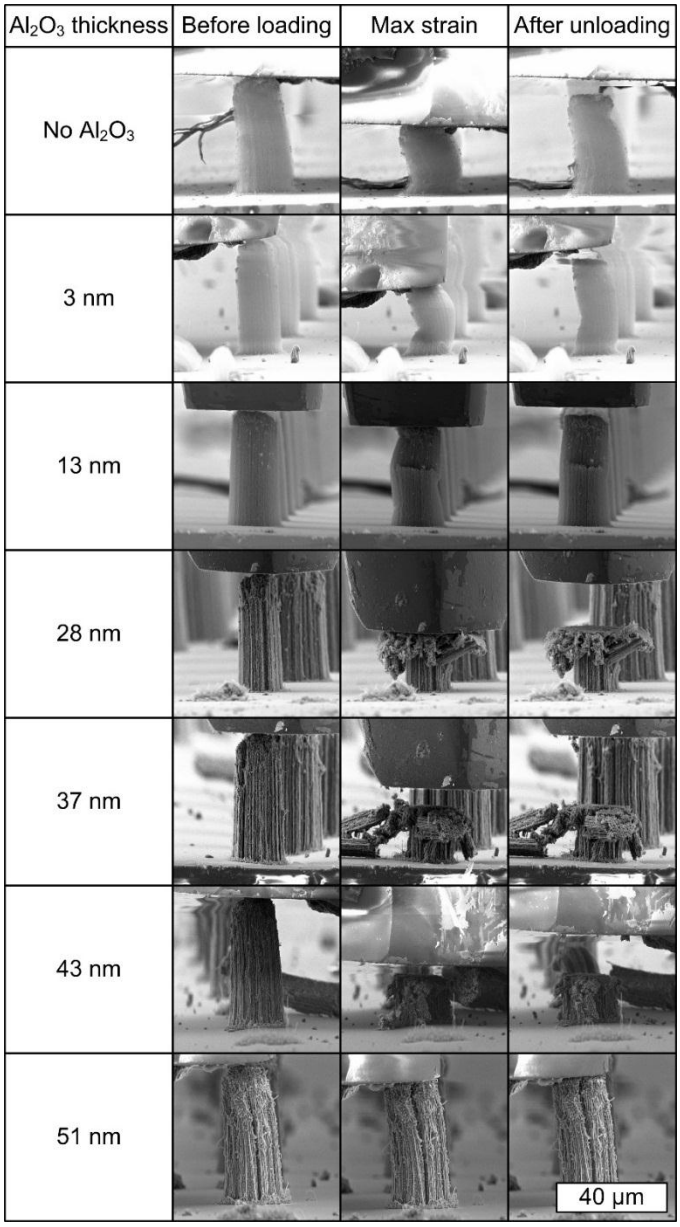

Figure 5.10 Axial compression of 20 µm diameter CNT micropillars coated with various thicknesses of Al_2O_3.

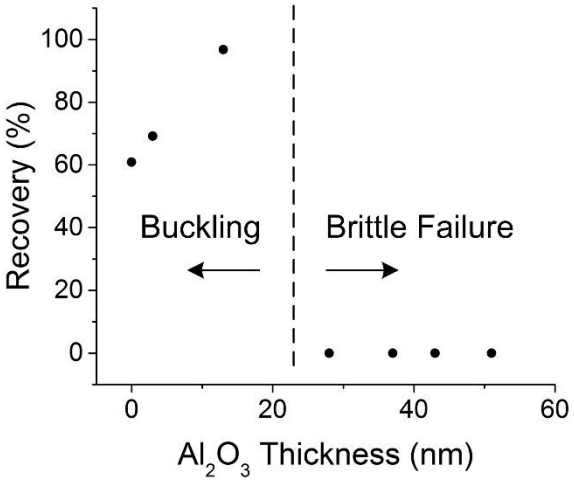

Figure 5.11 Recovery of CNT microstructures coated with various Al_2O_3 thicknesses after compression.

To clearly show the differences in deformation behavior, larger structures were coated and compressed axially. CNT microstructures with 100 µm diameter were grown to ~200 µm in height and coated with 3, 13 and 51nm of Al_2O_3 and compressed. Figure 5.12 shows the differences in failure modes of these structures.

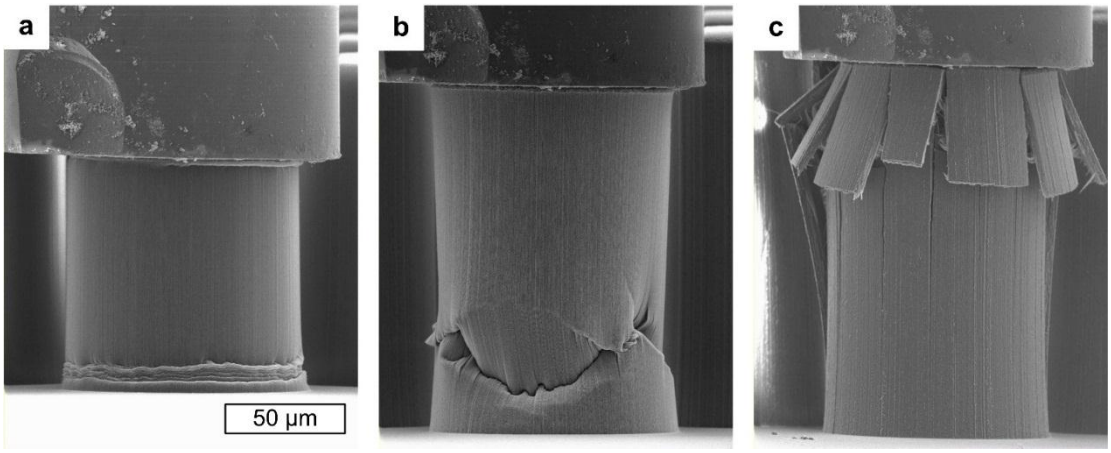

Figure 5.12 Deformation behavior of CNT micropillars subjected to various thicknesses of Al2O3 coating. a) 3 nm b) 13 nm, and c) 51 nm.

The progression of deformation of these structures is shown in Figure 5.13. Structures subjected to 3 nm of Al_2O_3 coating deform just like uncoated CNTs [103], developing accordion-like buckles at the base. This buckle formation is presumably due to the base having lower elastic modulus because of lower CNT density and alignment (Figure 5.13a). An intriguing phenomenon is observed during indentation of micropillars coated with 13 nm of Al_2O_3. The structure undergoes kinking of the shell, much like a rubber hose would (Figure 5.13b). Then upon unloading, the compressive strain recovers almost fully. Compressive strains of up to 50% has been observed to recover (Figure 5.14). Those coated with 51 nm of Al_2O_3 undergo brittle fracture. Since the diameter of the CNT micropillar exceeds twice the surface penetration depth of ALD, it behaves like a solid cylindrical shell with wall thickness of 5-7 μm. This structure undergoes two step buckling. Since Al_2O_3 is a brittle ceramic material, when loaded past the strength of the material, the structure barrels out and develops cracks along the axial direction of CNTs. The direction perpendicular to the CNTs does not develop cracks until much later when the structure catastrophically fails (Figure 5.13c). This can be seen as crack-bridging effect of CNTs in a fiber-ceramic composite [168]. Similar deformation behavior of Al_2O_3 coated CNT forests has been reported by Abadi *et al.* [169].

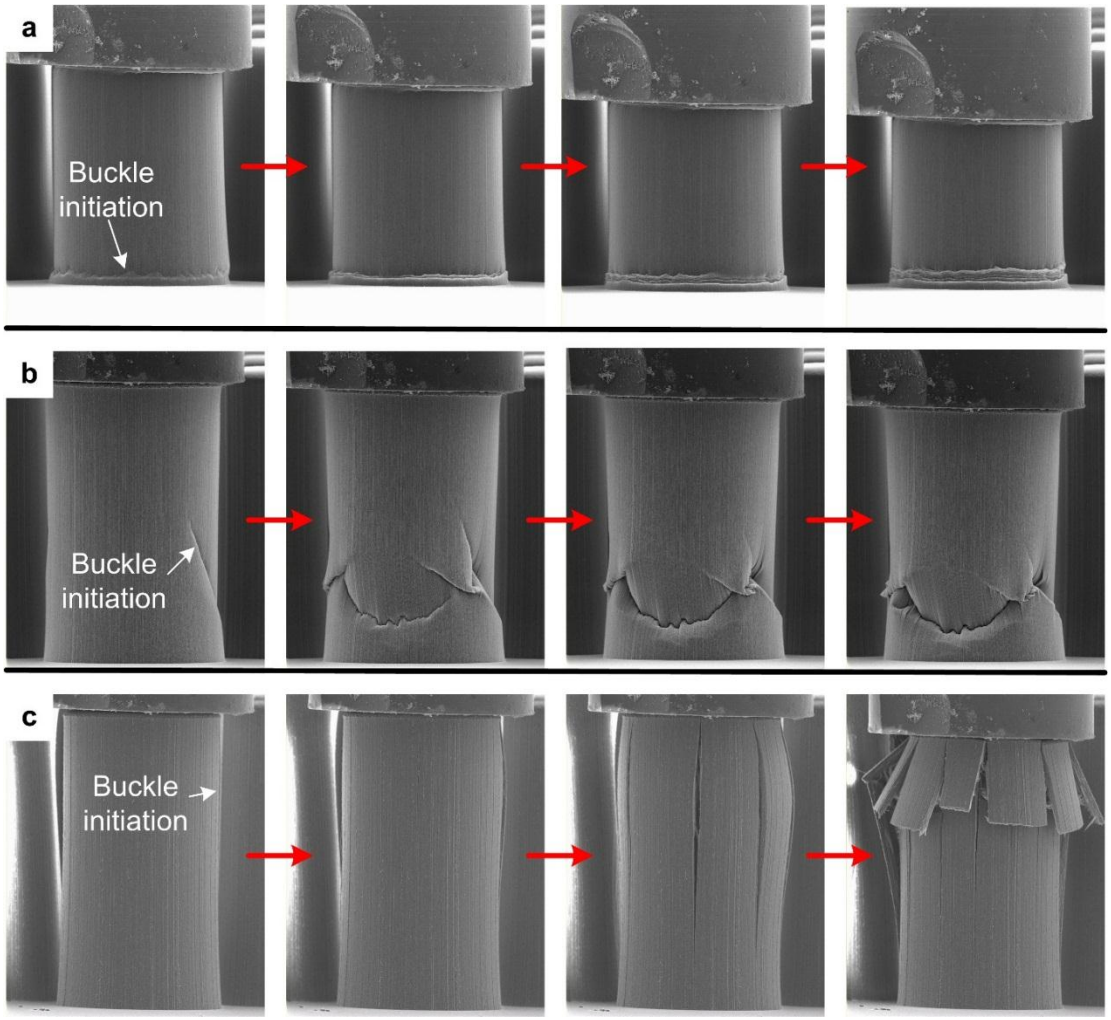

Figure 5.13 Deformation sequence of CNT microstructures subjected to various thicknesses of Al_2O_3 coating: a) 3 nm, b) 13 nm, and c) 51 nm.

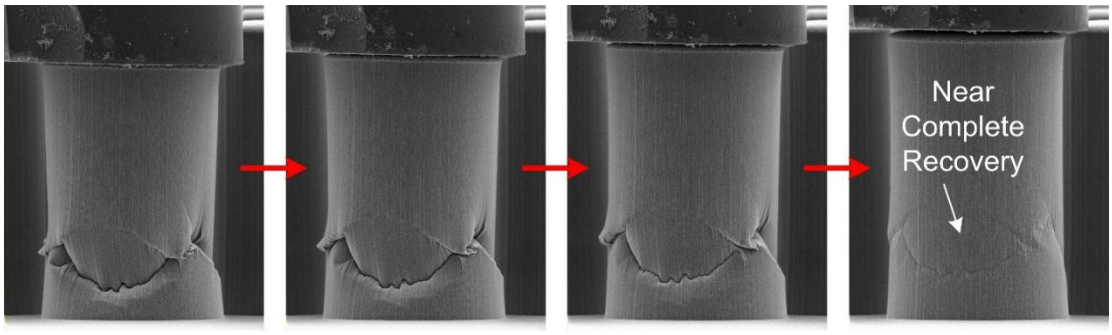

Figure 5.14 Unloading sequence of CNT microstructure with 13 nm Al_2O_3 coating.

The brittle failure of structures with 51 nm of Al_2O_3 coating clearly show snapping of the CNTs in the composite material. This snapping occurs when the brittle coating

material develops a crack and induces stretching of the CNTs in a radius. At approximately 2-3% global strain, the CNTs snap, leading to catastrophic failure shown in Figure 5.13c.

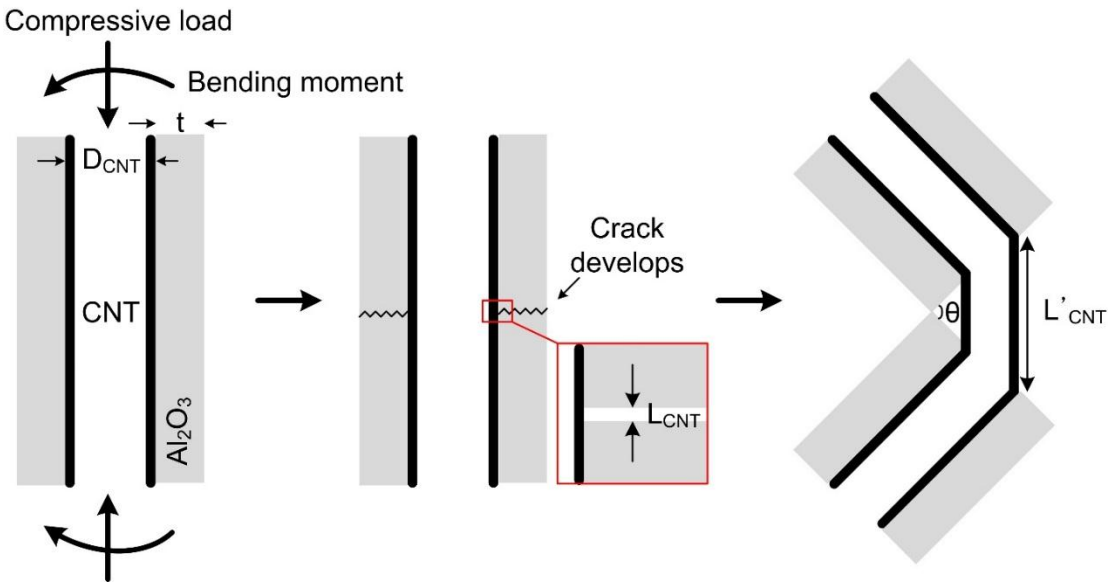

Figure 5.15 Compressive loading causes local stretching of CNTs.

At this moment individual CNTs are under tension, and typically the compressive load induces local strains in the CNTs. This strain, ε_{CNT}, can be quantified in terms of geometric parameters shown in Figure 5.15 as follows:

$$\varepsilon_{CNT} = \frac{L'_{CNT} - L_{CNT}}{L_{CNT}} \quad (4)$$

where L_{CNT} is the length of the exposed CNT segment before stretching and L'_{CNT} is the length of the exposed CNT segment after stretching which is expressed by the following equation:

$$L'_{CNT} = 2(t+D_{CNT})\sin(\theta/2) \quad (5)$$

where t is the thickness of the Al_2O_3 coating, D_{CNT} is the diameter of the CNTs and θ is the angle of the bend. The CNTs are locally strained to a much larger strain than the case where the coating was not present due to geometric constraints. **The conformal coating amplifies the local tensile strain in the CNTs under compression.** Once the induced tensile strain becomes too large for the CNTs to sustain it, the CNTs will fail by snapping. Individual CNTs [68, 170], as well as their ensembles [147, 171, 172] have large strain to failure. This strain limit is presumably different for different classes of CNTs, but values as large as ~14% for a Single-Walled CNTs (SWNTs) with 1 nm diameter [173], and ~16% for Multi-Walled CNTs (MWNTs) with 20 nm diameter [174] were experimentally measured and 15% for SWNT with small diameters was theoretically calculated [175]. The critical coating thickness that will cause snapping of CNTs can be derived by combining eq.1 and eq.2 above.

$$t_{crit} = \frac{(1 + \varepsilon_{CNT,limit})L_{CNT}}{2\sin(\theta/2)} - D_{CNT} \qquad (6)$$

Assuming 16% as the strain to failure [174], 10 nm CNT diameter [116], 3 nm average exposed CNT length, and 6° bend angle (measured from Figure 5.13c) of the CNTs in this case, the critical coating thickness is calculated to be 23 nm. This value falls in the transition zone between buckling and brittle failure modes of the Al_2O_3 coated CNTs (Figure 5.11). The average exposed CNT length is an assumption, and needs to be validated through other techniques.

Below the critical thickness of coating, the CNTs are still stretched, but do not snap, which stores elastic energy. Then the recovery of the structures is governed by the competition of the elastic energy stored in the stretched CNTs against the attractive forces between them in the compressed configuration (such as van der Waal's forces). The stored elastic energy is reduced as the coating thickness decreases as the local tensile strains in the CNTs decrease. This creates the linearly decreasing trend in recovery of the structure with coating thicknesses below the critical coating thickness.

5.4 CNT honeycomb structures with large recovery

Honeycomb structures (Figure 5.4c) allow fabrication of large scale CNT structure with uniform Al_2O_3 coating throughout. CNT honeycombs coated with 13 and 25 nm of Al_2O_3 were used to study the characteristics of CNT-Al_2O_3 composite foam configurations that show large elastic recovery. These structures were limited to hole sizes (15 μm and 11 μm) and height (60 μm) combinations that showed more uniform coating previously (Figure 5.5). A single compression and cyclic compression were performed on each CNT-Al_2O_3 composite honeycomb structures (Figure 5.16-17). Compression tests were done with load control on a Dynamic Mechanical Analyzer (DMA, Q800, TA Instruments), and up to 18N of load was applied for single compression and 10 N for 50 cycles in cyclic compression. The loading rate was limited to less than 10^{-3}/s for single compression test and was 0.01 hz for cyclic compression.

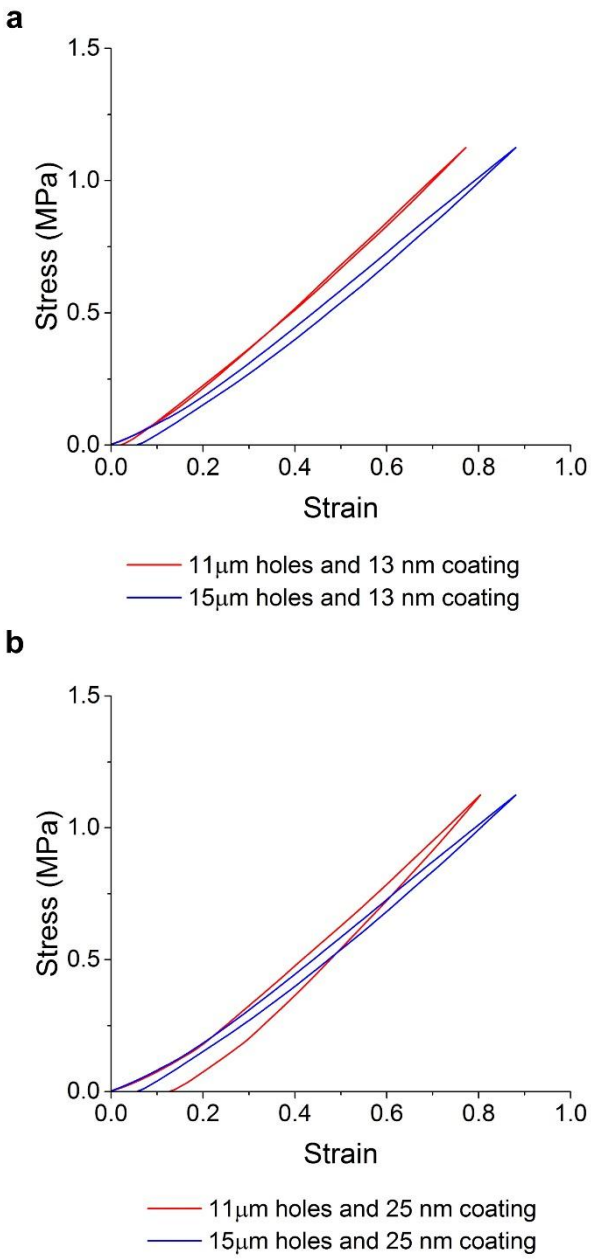

Figure 5.16 Single compression tests of Al_2O_3 coated CNT honeycomb structures. a) 13 nm, and b) 25nm.

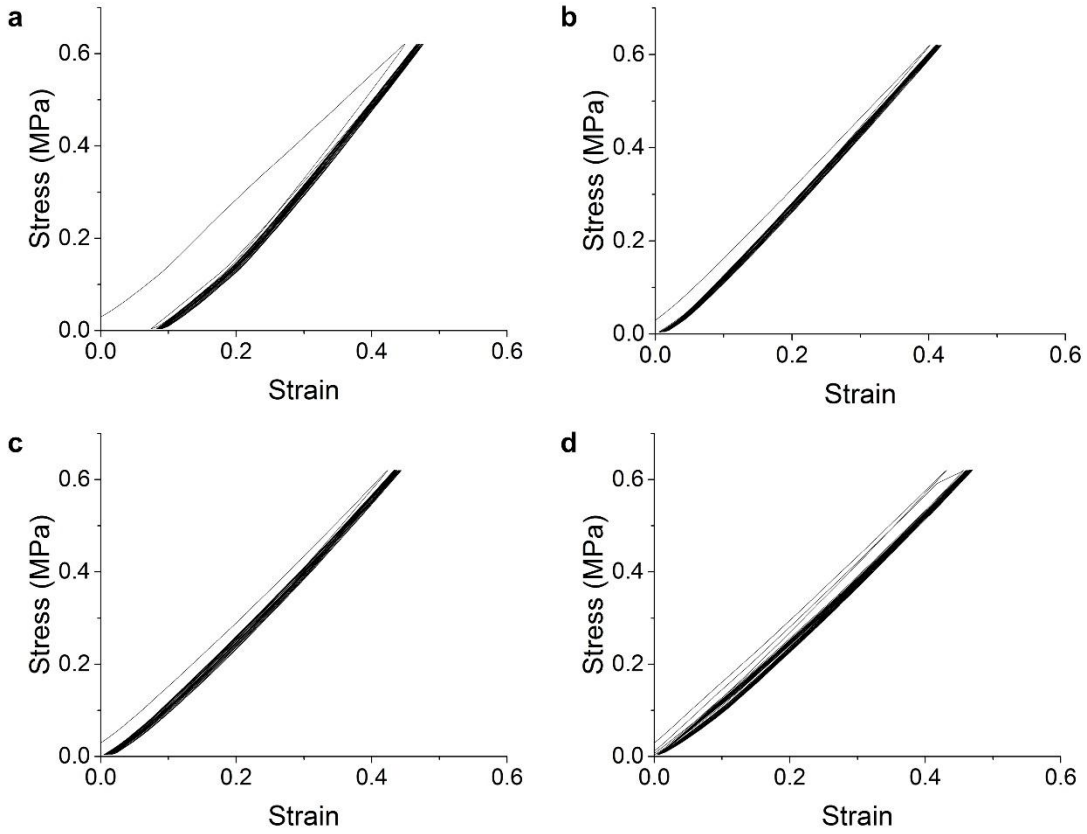

Figure 5.17 Cyclic compression tests (50 cycles) of Al_2O_3 coated CNT honeycomb structures: a) 11 µm hole/13 nm coating, b) 15 µm hole/13 nm coating, c) 11 µm hole/25 nm coating, and d) 15 µm hole/25 nm coating.

Compression tests reveal that the compressive strain of up to 0.75 is recoverable. Cyclic compression tests also reveal that strains up to 0.4 is recoverable and there is almost no structural degradation over 50 cycles. Closer examination of the data reveals that over 50 cycles only 2% of plastic deformation occurs, corresponding to 0.04% /cycle, which is almost negligible. Indeed, comparison of cross section of honeycomb structures that were compressed once and 50 times show that the structures suffered minimal damage during the cyclic loading with no evidence of non-recoverable buckling at both structural level and individual CNT level (Figure 5.18). Similar large strain recovery and structural integrity have been observed from CNT forests with much higher packing volume fraction [103] (13% as opposed to 1-2% which is typical of the CNT forests used in this work). The volume fraction of CNTs with 13 nm of Al_2O_3 is approximately 10%. The structural robustness and the large strain recovery characteristics make this

CNT-Al_2O_3 composite material attractive for applications requiring large strokes and resilience such as use as flexible mechanical elements in micro-electromechanical systems (MEMS) or in applications requiring compliant contacts.

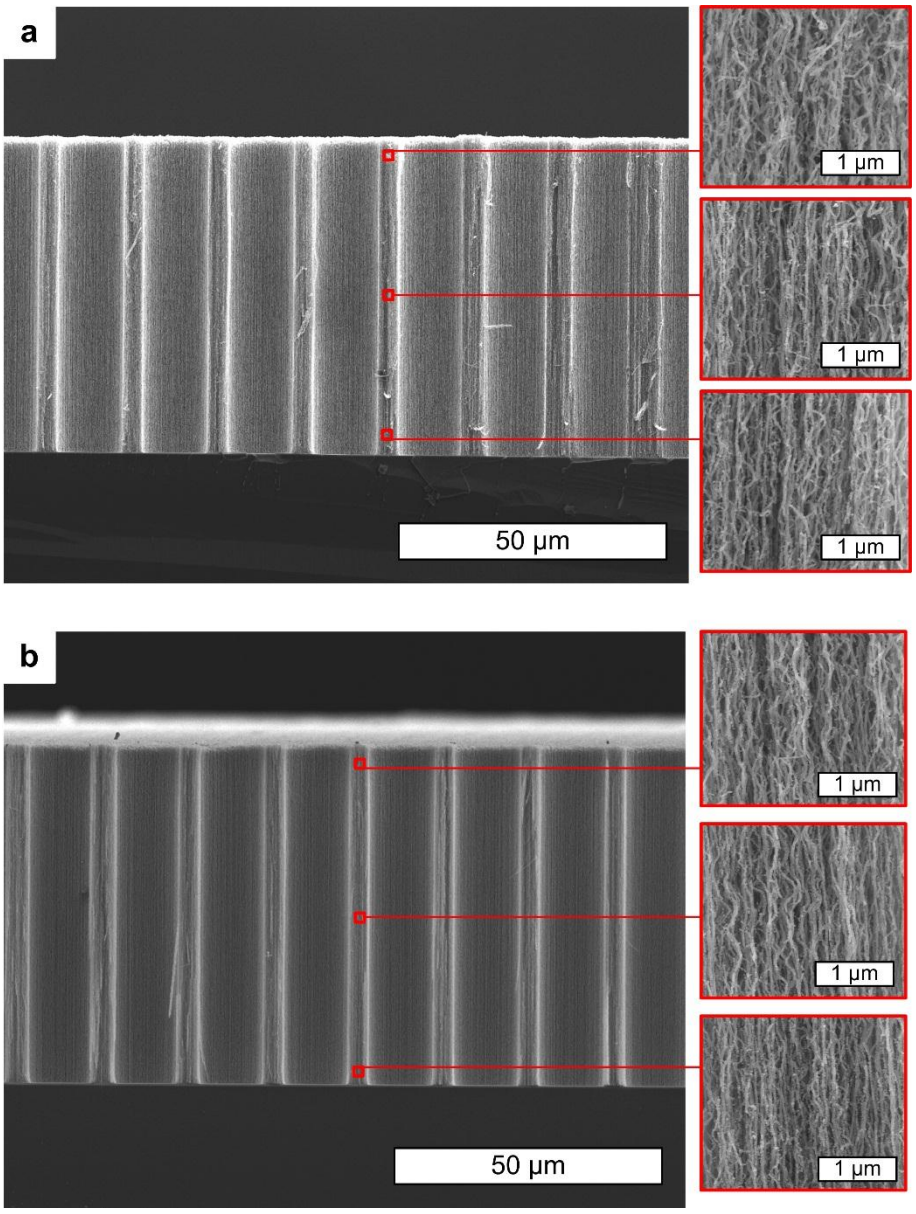

Figure 5.18 Cross section SEM images of a CNT honeycomb structure coated with 13 nm Al_2O_3: a) after 1 compression cycle, and b) after 50 compression cycles.

There is little hysteresis present in the load-displacement curves of the Al_2O_3 coated CNT honeycomb structures. The damping capacity of these structures, defined as the ratio of energy dissipated to energy absorbed during a single loading cycle, is shown in Figure 5.19. The damping capacity of Al_2O_3 coated CNTs is calculated to be in the range of 0.02-0.04 and stays constant over the course of 50 cycles. The damping capacity of these structures by themselves is quite low. However, since the structures are porous and exhibits large strain recovery, addition of polymers with high energy dissipation may potentially lead to composite material system that shows high damping capacity.

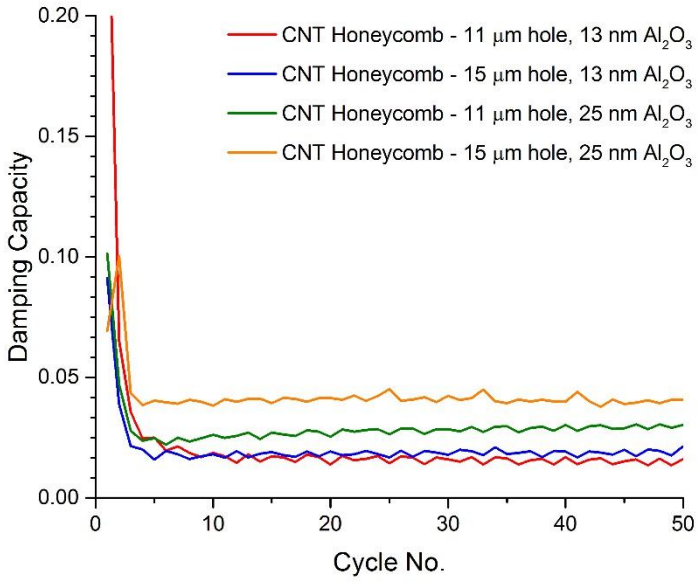

Figure 5.19 Damping capacity of Al_2O_3 coated CNT honeycomb structures.

CHAPTER 6

COMPOSITE MATERIAL WITH HIGH STIFFNESS AND DAMPING

Significant portions of this chapter with additional editing were published in: Meaud J., Sain T.*, Yeom B.*, Park S.J.* (*equal contributions), Shoultz A.B., Hulbert G., Ma Z.-D., Kotov N.A., Hart A.J., Arruda E.M. & Waas A.M., Simultaneously High Stiffness and Damping in Nanoengineered Microtruss Composites. Acs Nano 2014; 8: 3468-3475.*

This chapter describes the use of carbon nanotube (CNT) microarchitectures in a multifunctional composite that maximized stiffness and damping capacity simultaneously. First, the design of CNT microarchitecture in a truss-like geometry for strain amplification is presented. Then the fabrication technique for a two-part hard phase/soft phase composite material is described. Next, the properties of the fabricated laminated nanocomposite is presented. Lastly, the opportunities for property improvement are discussed.

6.1 Stiffness and damping

Most engineering structures are designed to have high stiffness and strength. However, in response to dynamic loads, the damping capacity is equally important and classical materials exhibit a tradeoff between stiffness and damping. For example, steel and diamond are very stiff but exhibit poor energy dissipation. On the other hand, materials with high damping such as rubber and other elastomeric materials have a very low stiffness. Materials combining high stiffness and mechanical energy dissipation are

needed in automotive, aviation, construction and other technologies where structural elements are exposed to dynamic loads.

In response to a sinusoidal load, the stress and strain are out of phase for a viscoelastic material. The tangent of the phase angle, commonly called tan(δ), (also known as loss tangent or loss factor), is a measure of the damping capacity of the material. There is a tradeoff between stiffness and damping and a figure of merit is defined to assess the combined performance of the material [176] as follows:

$$|E^*| * \tan(\delta) \qquad (1)$$

where E^* is the complex modulus and tan(δ) is the loss factor of the material. Most conventional materials cannot exceed 0.6 GPa in the figure of merit, which is shown on a stiffness-damping map as a dotted line in Figure 6.1. This line is referred to as Lakes line.

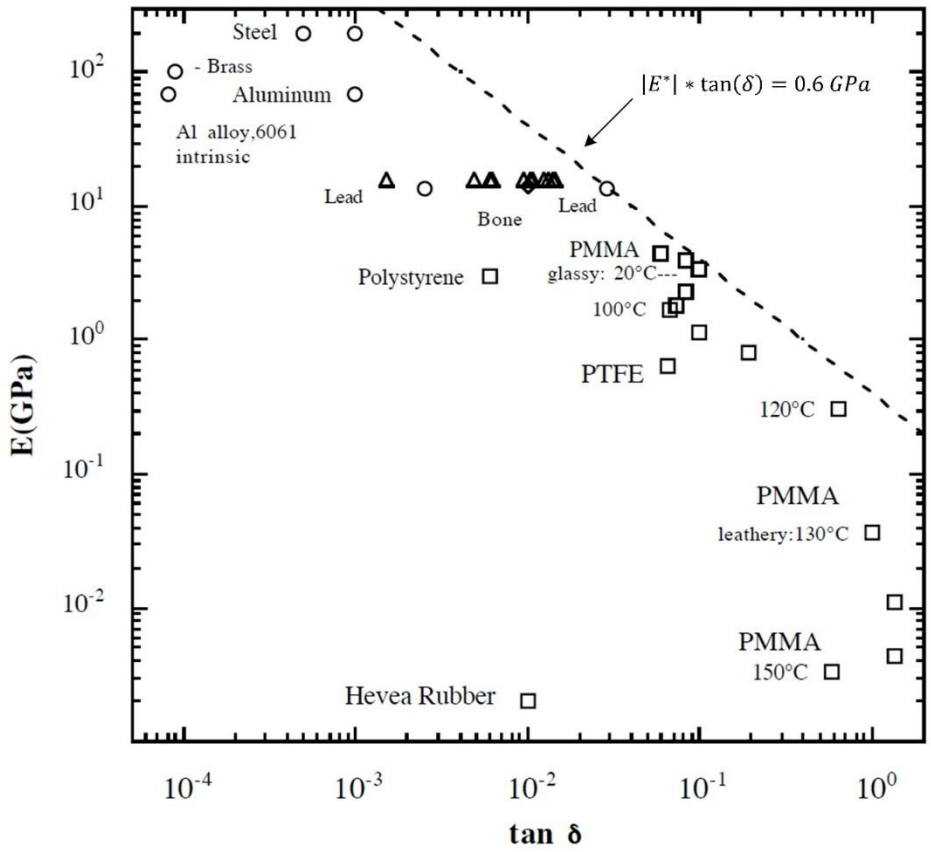

Figure 6.1 Stiffness-damping map with some common materials. The figure of merit value of 0.6 GPa is not exceeded by most materials. Figure adapted from [176].

The presence of structural hierarchy within natural and man-made materials and its effect on bulk material properties has been an important focus of the materials research community since the early nineties [177-179]. The hierarchical particulate composites with spherical inclusions proposed by Lakes [180] is one such hierarchy which can lead to improved stiffness and damping. However, preserving the mechanical properties as one moves up in length scale (e.g. from nanometer to micrometer) is a critical challenge for practically relevant macroscale materials [68, 181-184]. Understanding the effects of hierarchical structure can guide the *ab-initio* synthesis of new materials and thereby can result in desired mechanical properties [177, 185, 186].

6.2 Material-by-design

A combination of stiff strain-engineered CNT microtrusses and a high loss surrounding material with a judiciously designed structure was used to attain high stiffness and high damping simultaneously [176, 187-191]. The problem of preserving the mechanical properties as one builds up the hierarchy has been resolved by using a designed topology of carbon nanotube based truss structures and subsequent optimization of it. The exceptional ability to control the manufacturing of these building blocks - CNT microtruss and layer-by-layer (LBL) composite layer - allows a simulation-based *material-by-design* approach and reduces the processing and fabrication times compared to conventional nano-composites manufacturing. Using the concept of spatial strain amplification, which results from the material inhomogeneity, the proposed nanocomposites acquire orders of magnitude improvement in stiffness compared to the pristine polymer without any loss in damping.

In order to evaluate the best candidate microarchitectures for composites with high stiffness and damping, several topologies that could be manufactured using CNT growth were investigated using finite element methods (FEM)**.** Results from simulations for the composites are shown in a stiffness-loss map (in which the effective dynamic modulus is plotted as a function of the effective loss factor) in Figure 6.2a. A composite with straight pillars behaves like the Voigt topology analyzed by Chen and Lakes [187] exhibiting very high stiffness but low damping. Replacing the straight pillars with curved pillars and arranging them in a truss configurations can increase the damping with a moderate loss of stiffness. Parametric studies showed that by varying the stiffness of CNT pillars from 1GPa to 1TPa as shown in Figure 6.2b, a value of 100GPa stiffness produces the best combination of stiffness and damping for the nanocomposite.

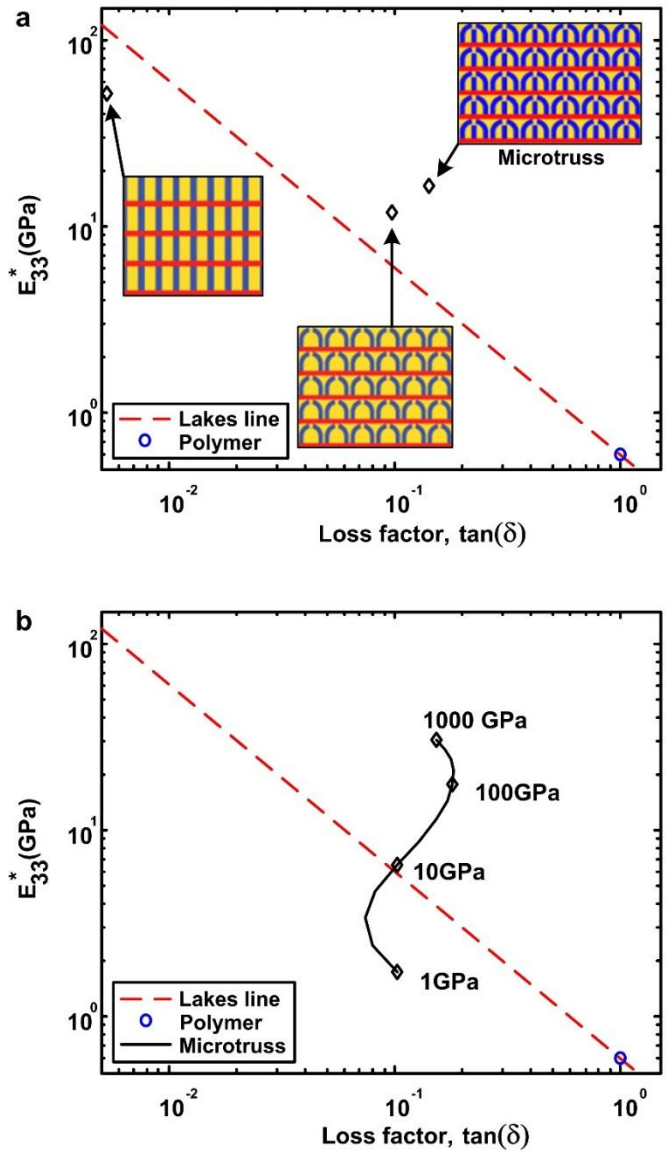

Figure 6.2 Computational evaluation of composite performance with varying a) geometries, and b) stiffness of truss members.

The contour plot of the dissipated energy per cycle, shown in Figure 6.3a, demonstrates that significant energy dissipation is introduced in the space between the straight pillars and the curved pillars in this most complex topology. Another set of parametric studies, as shown in Figure 6.3b, revealed that by optimizing the gap filled with polymer, higher stiffness can be achieved without any reduction in damping.

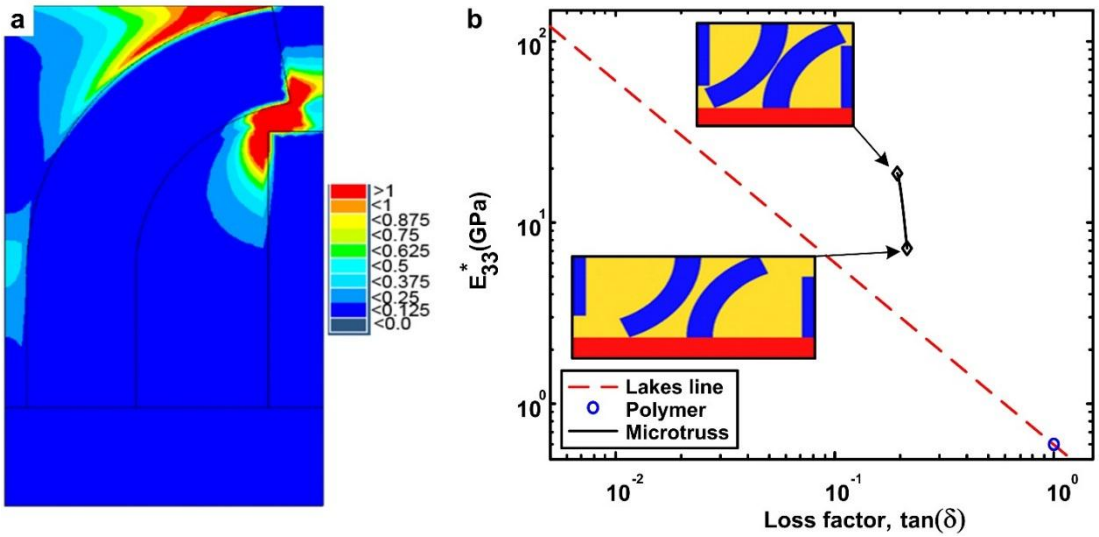

Figure 6.3 Strain amplification in the polymer matrix by stiff microtruss members. a) Dissipation contour plot b) Effect of the spacing between the truss members.

6.3 CNT microtruss

CNTs have been investigated as reinforcements for polymer nanocomposites because of their extreme stiffness [73, 192]. However early work did not take full advantage of the properties of the CNTs due to lack of organization at scales much larger than the nanoscale of the CNTs. Nanocomposites made of CNT forests filled with an elastomer have been shown to exhibit an anisotropic response with properties similar to a foam material when compressed in the direction of the fillers [193].

Strain-engineered CNT microstructures were designed to create the microtruss topology by geometry optimization. The angles of corner members of the microtrusses were varied by changing the overlap between the TiN underlayer and the catalyst pattern that defines the members. The center member was kept short by placing the catalyst pattern entirely on the TiN underlayer (Figure 6.4). Once the desired shape is chosen, a large array of CNT microtrusses were fabricated, and conformally coated by ALD of Al_2O_3 for mechanical reinforcement and subsequently by a nanostructured polymer film assembled using the layer-by-layer technique. The crevices of the trusses are then filled with lossy polymer.

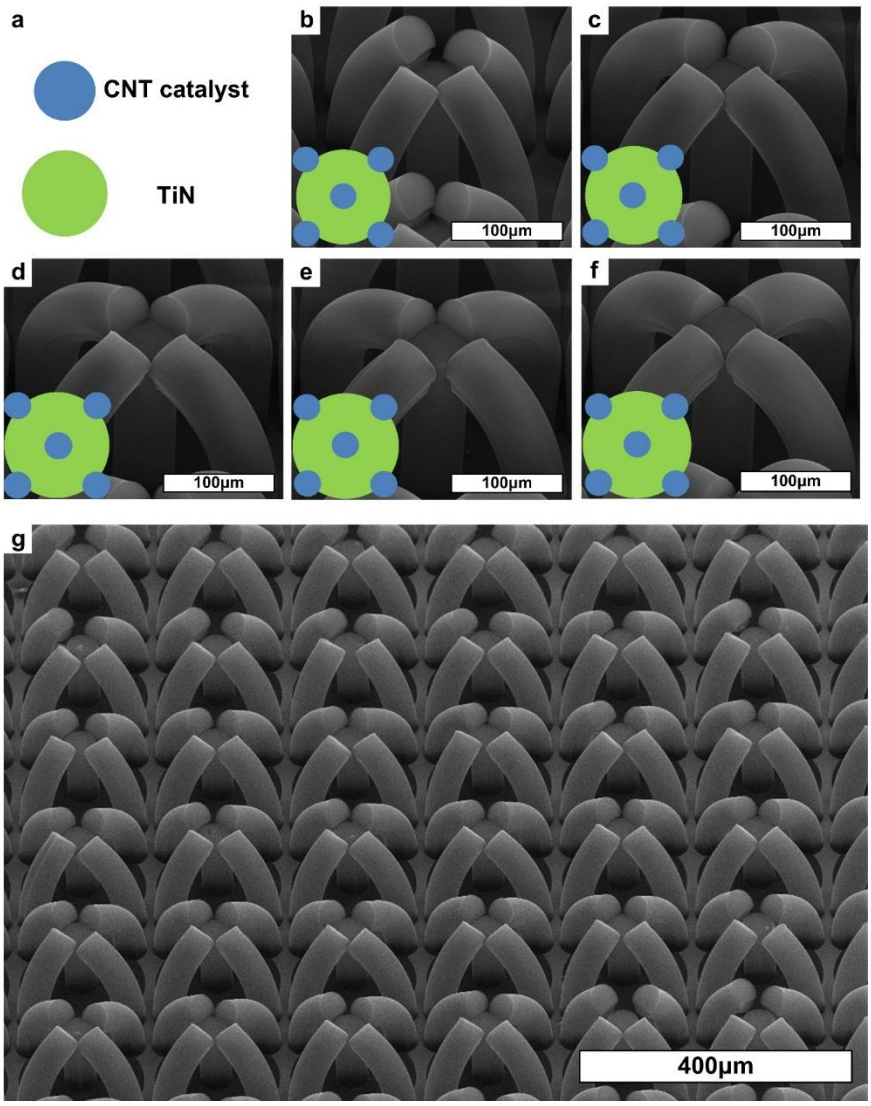

Figure 6.4 CNT microtruss geometry optimization: a) shows legend for catalyst pattern shown in b)-f) in the lower left corner b)-f) shows CNT microtrusses in the order of decreasing corner member angles. g) A large array of CNT microtrusses.

6.4 CNT microstruss–PU composite lamina

Previous studies have shown a LBL assembled clay-nanocomposite film [194] that exhibits remarkable stiffness enhancement at the macroscale (thickness of a few µm). However, even though LBL deposition has advantages in fine control of intermolecular interaction between matrix and fillers, fabrication of macro scale thick film using the LBL method requires a significant amount of time. Therefore these clay-nanocomposite films were used to coat the Al_2O_3 reinforced CNT microtrusses to take advantage of

their properties.

Once the LBL process is done, the remaining open spaces between the CNT microtrusses are filled with Polyurethane (PU) with large damping capacity. The PU in solvent is drop casted on the CNT microtrusses and the solvent is evaporated by heating on a hot plate. Once the solvent has evaporated, the remaining uneven PU/CNT microtruss film is molded by applying heat to flow the PU and pressing against a flat surface (Figure 6.5a) to remove the excess PU above the CNT microstrusses. The resulting film has flat top and bottom with CNT microtrusses revealed without excess PU to cover them (Figure 6.5b).

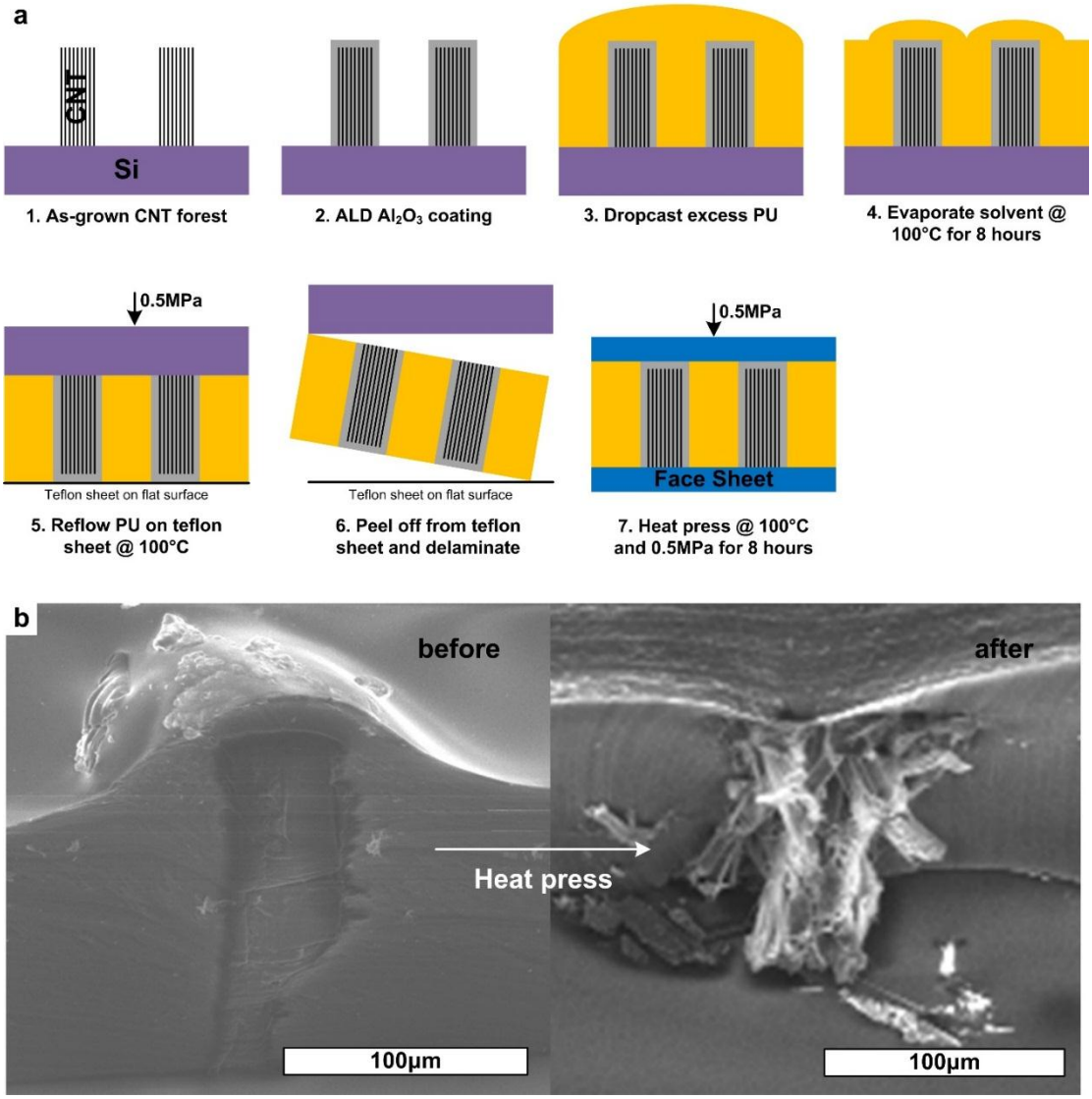

Figure 6.5 CNT microtruss-PU composite lamina fabrication a) Schematic of the process flow b) Effect of molding to get rid of excess PU at the top.

This flat PU film with embedded CNT microtrusses (Figure 6.6a) is sandwiched between steel sheets, and this repeat unit is stacked to a desired thickness to produce a layered nanocomposite (Figure 6.6b). The core elements and particles have dimensions in the nanometer range while the CNT truss members have height in the micrometer range. The in-plane dimensions of the overall composite are 5-10 mm; the out-of-plane dimension is 0.65 to 0.85 mm. Combination of the two different length scales in manufacturing gives rise to a hierarchical structure within the material with a very attractive combination of stiffness and damping.

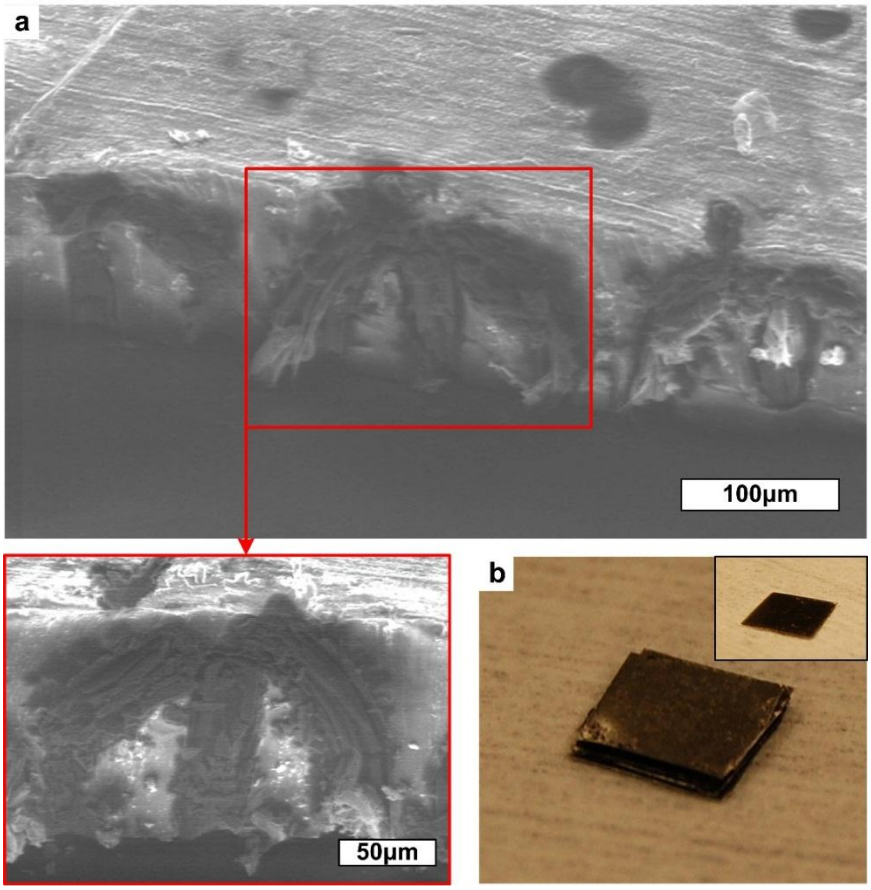

Figure 6.6 Final composite laminate with steel interlayer face sheets. a) Cross section of a single composite lamina b) Stacked laminate (Inset shows a single lamina).

6.5 Stiffness and Damping measurements

Toward manufacturing the final composite, first a single layer alumina coated microtruss sample filled with PU is tested under nanoindentation (as shown in the inset of Figure 6.6b). The geometry of the samples considered were as follows: a single layer of dimension 10 x 10 mm^2 with microtrusses composed of 40 μm diameter CNT truss members, leading to the final composite manufactured by sandwiching 3 such layers resulting in a thickness of 850 μm for the layered composite with in-plane cross section dimensions of 10 x 10 mm^2 (as shown in Figure 6.6b**).** The single layer sample was tested using a spherical indenter of diameter 150 μm under load control. The final composite was subsequently tested to assess its mechanical properties (tension-compression mechanical machine, Kammath & Weiss). A macro-scale measurement was chosen instead of nanoindentation in order to determine homogenized (on the scale of several repeat geometrical unit cells) properties rather than local point-wise properties. DMA measurements were not considered because of their low resolution. The sandwiched composite was loaded and unloaded in cyclic compression at a constant displacement rate of 0.5 μm/sec (corresponding to a strain rate of 6e-4/sec). The load-displacement curves were recorded from both the tests, and stress-strain values were calculated once the cyclic response was stabilized after three cycles of loading/unloading of both the samples, resulting in the plots shown in Figure 6.7.

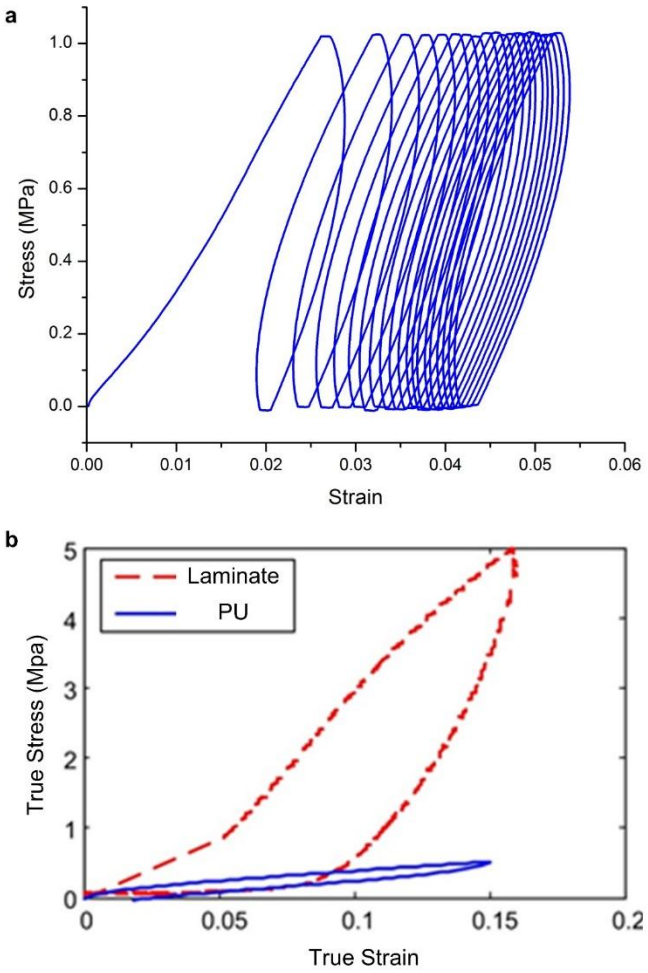

Figure 6.7 Stiffness and damping measurement of fabricated composite material: a) cyclic compression of a single lamina, and b) compression of a multi-layer laminate.

For the triangular loading pulse used in these experiments, damping cannot be measured in terms of the tangent of the phase angle. However, an energy-based definition of damping, the specific damping capacity (denoted as, ψ), can be used [195]. Specific damping capacity ψ is defined as the ratio of the dissipated energy per cycle to the stored energy. The dissipated energy per cycle is given by the area within the loading/unloading curve. The stored energy is given by the enclosed area of the triangle connecting the origin, the point on the curve corresponding to maximum strain, and the projection of this point on the horizontal axis. To compute the stiffness of the truss sample from the loading/unloading curve, the slope of the unloading curve was used.

It is observed that the composite has considerably higher stiffness than the pristine PU

for both single layer and the final sandwiched composite. The stiffness of the PU with the same loading condition was found to be 2.3MPa. It increased to 318MPa for the single layer and 204MPa for the sandwiched specimen. Moreover, the damping of PU (ψ=0.54) was maintained in the case of the final sandwiched structure (ψ=0.54) even though it was slightly lower in the single layer specimen (ψ=0.45). The difference between the single layer measurement and the final sandwich composite is due to the different test set-ups used, as an indentation test used for the single layer specimen only measures relatively local material response depending on the indenter location, hence it is usually different than the global macroscopic response. It is highly possible that the indenter tip directly touches the microtruss and therefore provides a much stiffer response and lower damping. Further, the final sandwich composites may have manufacturing variability between successive layers, resulting in variation in response.

The resulting composite exhibits much higher stiffness (100 times) and similar damping (specific damping capacity of 0.8) compared to the monolithic backbone material. The manufacturability of the laminate based architecture and the compatibility between the CNT microtruss and the surrounding viscoelastic layer gives the resulting composite attractive macroscale properties and paves the pathway for future practical applications.

6.6 Opportunities for improvement

Imperfections in the manufacturing process, such as the presence of PU between the top of the CNT pillars and the metal sheets, could cause a drop in the stiffness and an increase in the damping. For these reasons theoretical simulations are expected to be an upper bound for the stiffness and a lower bound for the damping. The important point to note here is that even with manufacturing imperfections, the composite has significant improvement in stiffness properties (30 fold for the 40 μm CNT microtruss) without losing any damping of the base PU. As explained earlier the chosen microtruss topology enhances shear dissipation within the PU matrix and hence damping doesn't reduce as much as one expects in a traditional Voigt topology. For this particular set of samples the damping of the pristine PU was preserved in the final sandwiched composite. However our model prediction shows that by increasing the CNT stiffness

and reducing the gap between successive CNT pillars one can actually improve both the stiffness and damping of the final composites (as shown in Figure 6.2b and 6.3b) and the resulting composite response (with CNT pillar stiffness being 1 TPa composite stiffness can be 30 GPa and damping about 0.6) can exceed the traditional bounds estimated by Lakes.

CHAPTER 7

SUPERHYDROPHOBIC AND DIRECTIONALLY WETTING SYNTHETIC SURFACE

This chapter presents a design and manufacturing of a simultaneously superhydrophobic and directionally wetting surface inspired by a butterfly wing. First, the concept of superhydrophobicity and anisotropic wetting properties are discussed. Next, a proof of concept experiment with unidirectionally curved carbon nanotube (CNT) microstructures are presented to demonstrate superhydrophobicity and directional wetting properties. Then, CNT microstructure arrays with geometry closely mimicking butterfly scales is designed and manufactured. Finally, the superhydrophobicity and directional wetting properties of the CNT butterfly scales are quantified by measuring their contact angle hysteresis.

7.1 Hydrophobicity

Hydrophobic state refers to a situation where a droplet has a contact angle (CA) above 90°. Superhydrophobicity refers to a state of CA above 150°. The CA changes due to surface energy minimization of the droplet. The Wenzel model [196] states that the CA is described by the following equation:

$$\cos(\theta^*) = r\cos(\theta) \qquad (7)$$

where θ^* is the apparent contact angle, θ is the Young's contact angle (for an ideally flat surface of same material) and r is the ratio of true area to the apparent area of the surface.

The Cassie-Baxter model [197] states that the CA is the average of air-liquid CA and solid-liquid CA and describes the contact angle with the following equation:

$$\cos(\theta^*) = -1 + \phi_s\big(1 + \cos(\theta)\big) \qquad (8)$$

where φ_s is the fraction of solid in contact with the liquid. Wenzel model breaks down at higher θ and at large *r* where it predicts the apparent CA to be 180°. Therefore Wenzel model is applicable at CA lower than a threshold θ_c beyond which the Cassie-Baxter model is applicable. The threshold θ_c can be calculated by equating the two equations [198] which yields:

$$\theta_c = (\phi_s - a)/(r - \phi_s) \qquad (9)$$

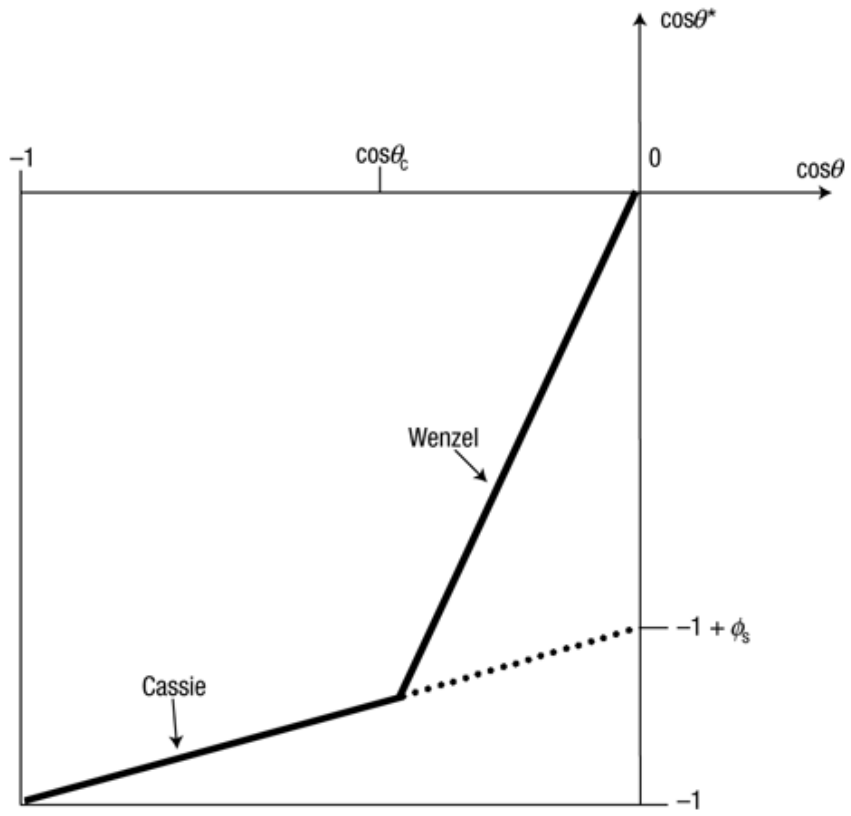

Figure 7.1 Relationship between apparent CA (θ*) and Young's CA (θ) showing the two superhydrophobic regimes and their boundary θc. Dotted line shows metastable Cassie-Baxter state. Figure adapted from [199].

7.2 Superhydrophobicity and anisotropic wetting properties of natural surfaces

Microscale roughness plays an important role in wetting behavior of a surface [199]. Examples abound in nature where hierarchical micro- and nanoscale structures are employed to tune the wetting behavior of a surface [200]. Lotus leaves [201, 202], cicada wings [203] and gecko feet [204], are superhydrophobic which leads to their self-cleaning behavior. Rose petals are superhydrophobic, but with high adhesion [205] due to Cassie impregnating wetting. Fish scales are superoleophobic [206] both in air and water. Anisotropy is also prevalent on natural surfaces. Scallion and garlic leaves [207] show large contact angle hysteresis and shark skins have anisotropic drag [208]. Seemingly a paradox, salvinia achieves air retention under water with hydrophilic pins [209].

Some natural surfaces have combinations of directional and superhydrophobic wetting behavior. A butterfly's wing (*Morpho Aega*) has hierarchical micro- and nanostructures that rolls the droplet in the radially outward direction, but pins them in the opposite direction [210] (Figure 7.2). This is due to the fact that individual scales on the wings act like hinged flaps that lift up and resist the rolling of droplet in one direction but not in the opposite direction.

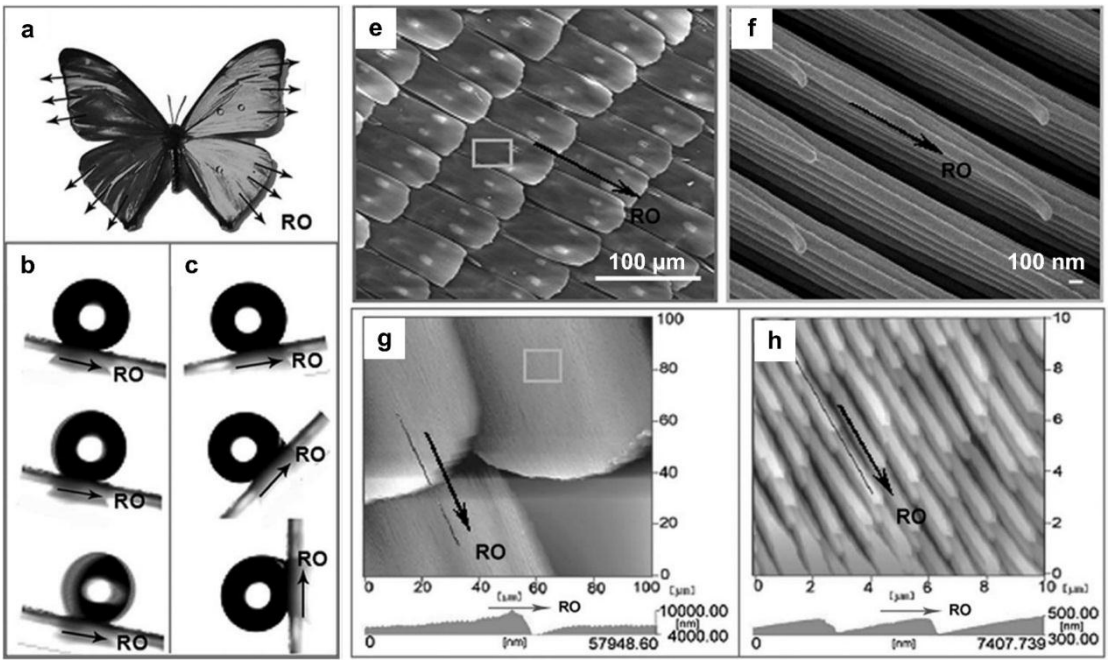

Figure 7.2 Anisotropically wetting and superhydrophobic butterfly wings. a) RO direction b) Droplet rolling in RO direction c) Droplet pinning against RO direction d) SEM image of wing scales f) SEM image of nanoscale ridges g) AFM image of wing scales h) AFM image of nanoscale ridges. Figure adapted from [210].

Efforts to re-create these surfaces with complex wetting behaviors have been limited to surface textures such as replica molding of rose petals [211] and rice leaf/butterfly scale like structures [212], or machining of grooves on the surface of a metal [213]. These surfaces do capture anisotropic and superhydrophobic wetting behavior, but do not show the directional wetting as the wing scale architecture which plays on important role in the directionality of wetting behavior is absent.

Slanted polymer nanorods [214] and curved silicon nanopillars [37] have also shown

anisotropic wetting, but not superhydrophobicity. Indeed it remains a challenge to replicate butterfly scales. In the next section, it is shown that CNT microarchitectures can be used to re-create the hierarchical geometry of butterfly scales.

7.3 Superhydrophobicity and directional wetting behavior of unidirectionally curved CNT microstructures

CNTs have been shown to achieve anisotropic and superhydrophobic wetting behaviors via chemical modification and microstructure patterning [215]. ALD reinforced and silanized curved CNT microstructures show directional wetting behavior (Figure 7.3a) resisting droplet movement in one direction by the curved micropillars being deflected by the rolling droplet. In the opposite direction, the droplet rolls without pulling the curved micropillars with it. The same microarchitecture shows superhydrophobicity in a Cassie-Baxter state as well (Figure 7.3b). This result shows that it is possible to create CNT microarchitecture based surface that has both superhydrophobicity and directional wetting properties, and motivated design and fabrication of an ‘artificial butterfly wing’.

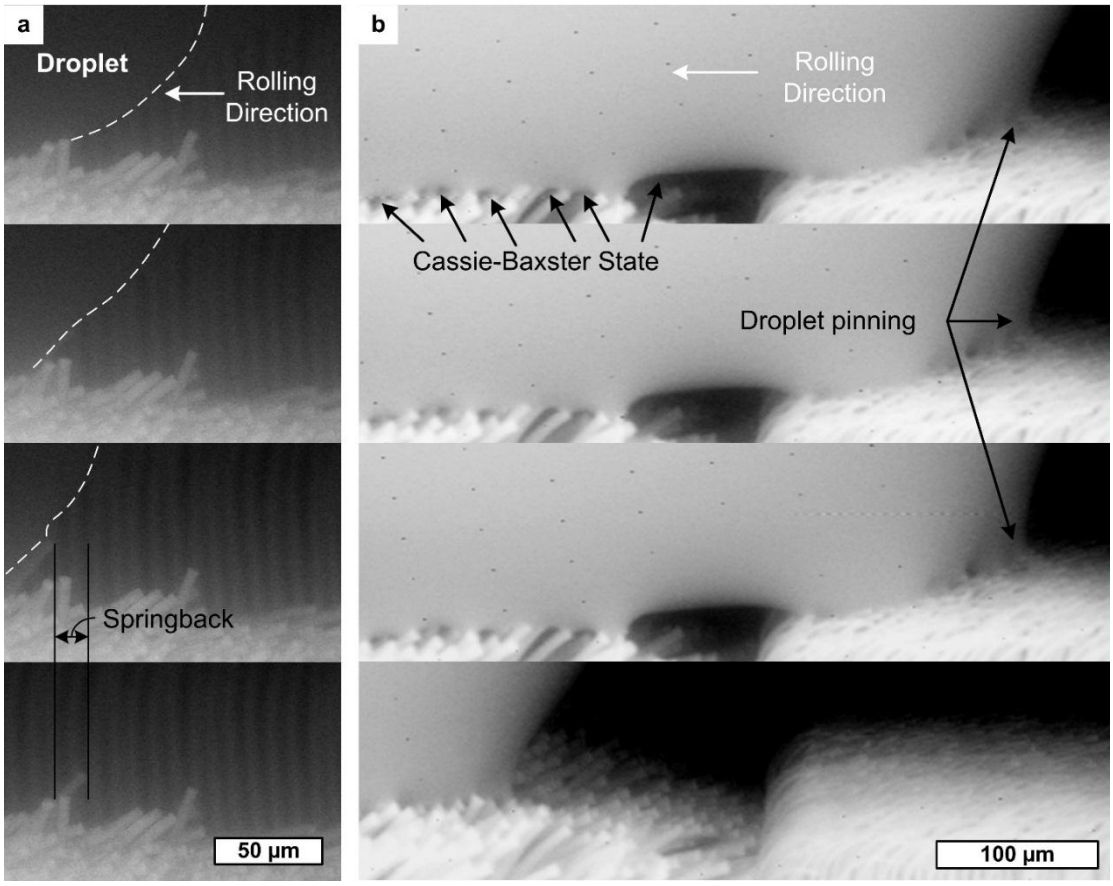

Figure 7.3 In Situ SEM video snapshots of droplet rolling on reinforced and silanized curved CNT microarchitectures that show a) bending of a curved pillar that resists the droplet rolling motion, and b) droplet pinning and superhydrophobicity on curved CNT microarchitectures.

7.4 Design and fabrication of CNT microstructure arrays resembling butterfly scales

In order to mimic the butterfly scales, a hierarchical design was chosen where each CNT microstructure will have a large flat surface facing the vertical direction, with smaller scale ridges with high aspect ratio. The catalyst outline is defined such that the smaller scale ridges are added on one side (Figure 7.4a). Then the TiN layer outline is defined across the neutral axis of the cross section, away from the ridge definition with room for alignment error in the lithography. This will ensure that the scales will grow and curve away from the ridges, exposing them to the top surface when the trajectory of the microstructure reaches angles around 90° (Figure 7.4b). The catalyst and TiN

definition is repeated over a large area, leaving some gap in between the structures so that they may move independently of one another (Figure 7.4c). With geometric tuning and surface modification, a droplet sitting on this surface is expected to be in the Cassie-Baxter regime (Figure 7.4d).

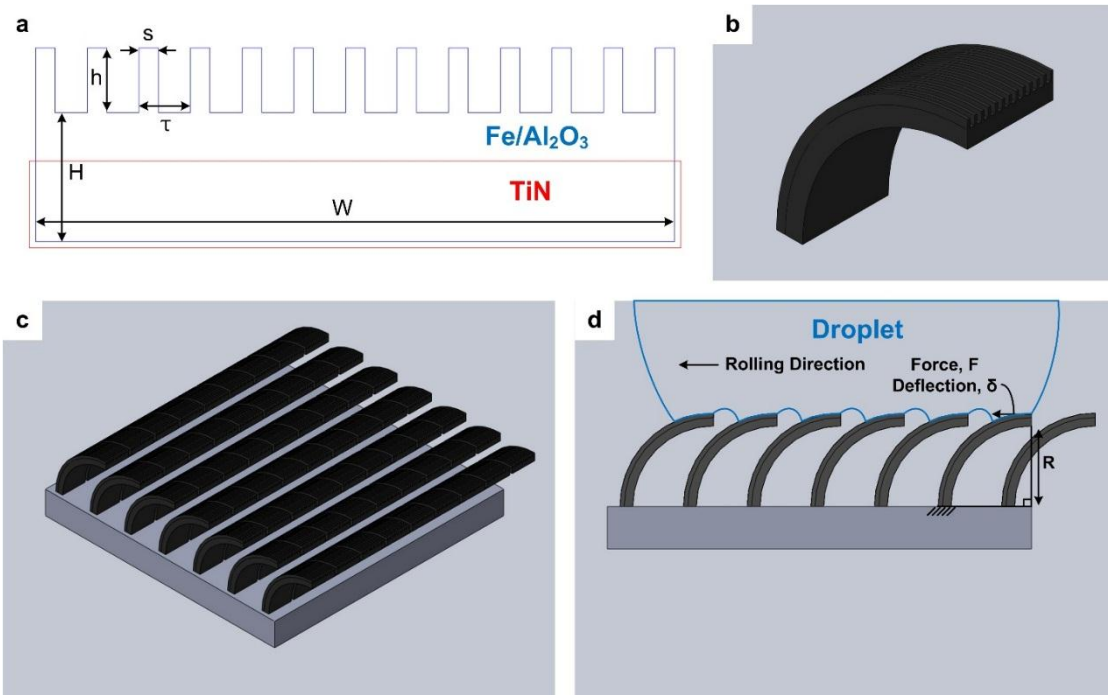

Figure 7.4 Design of CNT butterfly wing architecture a) Catalyst stack pattern for a single scale showing the scale cross section with microscale ridges on top - s is the ridge width, τ is the ridge wavelength (s/τ is the ridge density), h is the ridge height, H is the base height, W is the base width. b) A solid model of CNT microstructure with ridges facing the vertical direction. c) A proposed arrangement on a substrate d) A side view of the array with a schematic showing droplet rolling and resulting capillary force direction.

Individual CNT scales can be thought of as rotary springs with the spring constants tuned by the geometry as well as the material properties. For a curved beam following 90° arc trajectory and constrained at the base (Figure 7.4d), the lateral deflection (δ) can be expressed as follows [216]:

$$\delta \cong \frac{\pi F R^2}{4EI} \qquad (10)$$

where *F* is the force applied, *R* is the radius of curvature, *E* is the elastic modulus and *I* is the second moment of area. The stiffness in lateral direction (*F*/δ) can be obtained by re-arranging equation (4) as follows:

$$\frac{F}{\delta} \cong \frac{4EI}{\pi R^2} \qquad (11)$$

This value depends on the elastic modulus (*E*) as well as the geometric parameters (*I* and *R*), opening up opportunities for precise tuning by architectural design as well as property tuning of CNT microarchitectures. For observation with *In situ* SEM, the deflection should be on the order of 10 μm and forces acting of microstructures with similar geometries has been measured to be approximately 10 μN [217], leading to 1 N/m target stiffness of the CNT scales. The thickness of the CNT scales was chosen based on the target stiffness and properties of Al_2O_3 reinforced CNTs and was decided to be 20 μm. Table 7.1 shows the geometric specification of the designed scales.

Table 7.1 Geometric parameters of the CNT scale catalyst patterns used in this work.

Geometric parameter	**Value (μm)**
Ridge width, s	3
Ridge wavelength, τ	8,16
Ridge density, s/τ	0.1875, 0.375
Ridge height, h	10
Base height, H	20
Base width, W	99

The catalyst pattern shown in Figure 7.4a was fabricated and subjected to CNT growth to achieve CNT butterfly scales (Figure 7.5). The structures show excellent resemblance to actual butterfly scales (Figure 7.2e and Figure 7.6). Once the scales were grown, they were coated with 25 nm of Al_2O_3 via atomic layer deposition (ALD) to provide structural reinforcement and subsequently coated with fluorosilane to imbue superhydrophobicity.

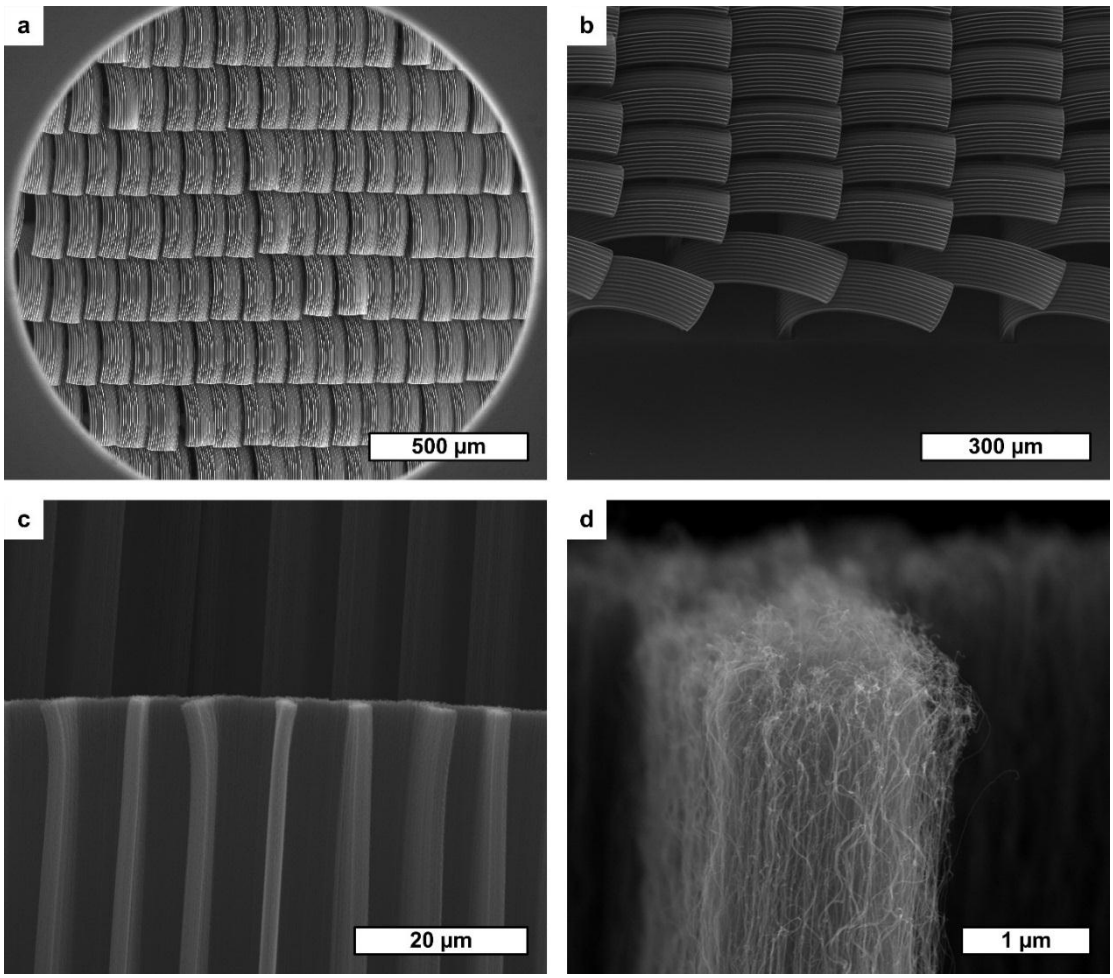

Figure 7.5 CNT microarchitecture closely resembling the butterfly scales. a) A large array overview b) Edge of the array c) Tip of an individual scale showing the smaller scale ridges d) Close up of individual ridge, the width is less than 2 µm.

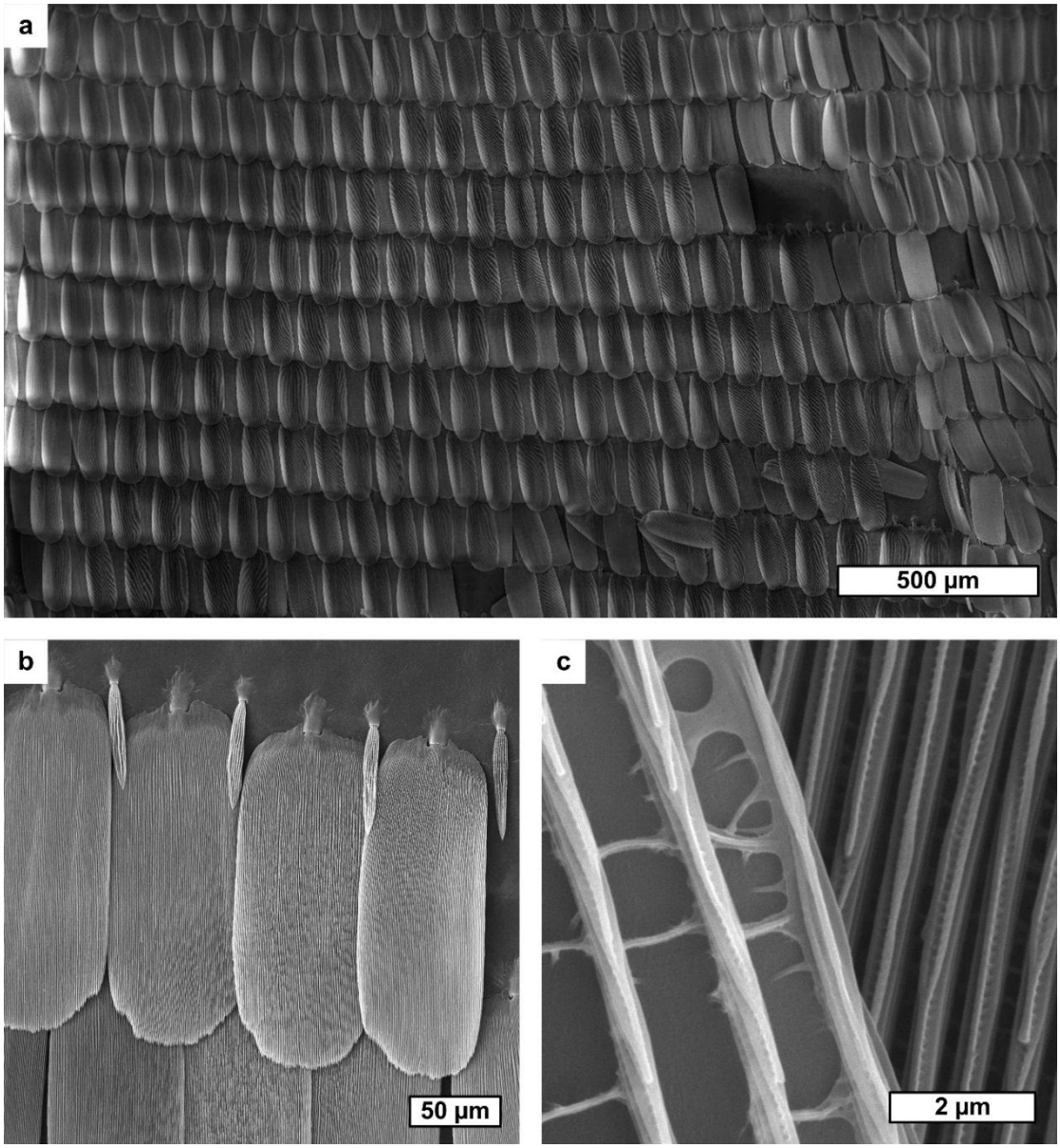

Figure 7.6 Scales from an actual butterfly wing a) A large area overview of the scales b) A few scales c) Nanoscale ridges on the scales. (Images courtesy of Adam Paxson.)

7.5 Superhydrophobicity and directional wetting properties of CNT scales

The superhydrophobicity (CA>150°) and directional wetting properties of the CNT scales were quantified by measuring the CA hysteresis (CAH) of the fabricated samples. The CAH is defined as the difference of the two CAs and to show directional wetting behavior, the CAH in two opposing directions on the surface need to be different. A goniometer (Model 500, ramé-hart instrument) on a floating stage was used to measure the CAH. Droplet scrubbing experiments were performed, where a droplet anchored on a needle is positioned on the surface and the surface is translated using a linear translation stage. The image of the droplet is captured by a camera and analyzed to obtain the two CAs (advancing and receding) of the droplet on the surface in a particular direction (Figure 7.7).

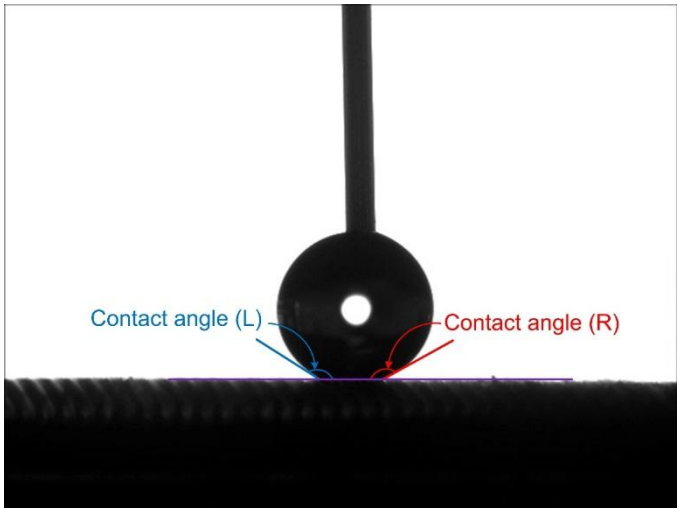

Figure 7.7 Contact angles measured by the goniometer in a droplet scrubbing experiment.

The CA measurements of CNT butterfly scales are shown in Figure 7.8. The data show that CAH hysteresis is higher in the RI direction regardless of the ridge density, and that the higher ridge density leads to larger CAH in both directions. The differences in CAH in the RI and RO directions for both ridge densities is shown in Figure 7.9. As the droplet is translated over the surface, it gets pinned on individual CNT scales and needs

to pull away before it can continue translating over the surface. The CNT scales will deflect more in RI direction before the droplet is de-pinned, causing the CA to decrease more before the de-pinning event. This leads to increased CAH in the RI direction. CNT scales with higher ridge density will have longer contact line between the droplet and the scales. This causes more forces to be imparted on the scales, causing further deflection before the droplet is de-pinned leading to higher CAH as shown in Figure 7.9. This is a successful usage of strain-engineered CNT microstructures to re-create the butterfly scales, and a first demonstration of superhydrophobicity and directional wetting properties simultaneously on a synthetic surface.

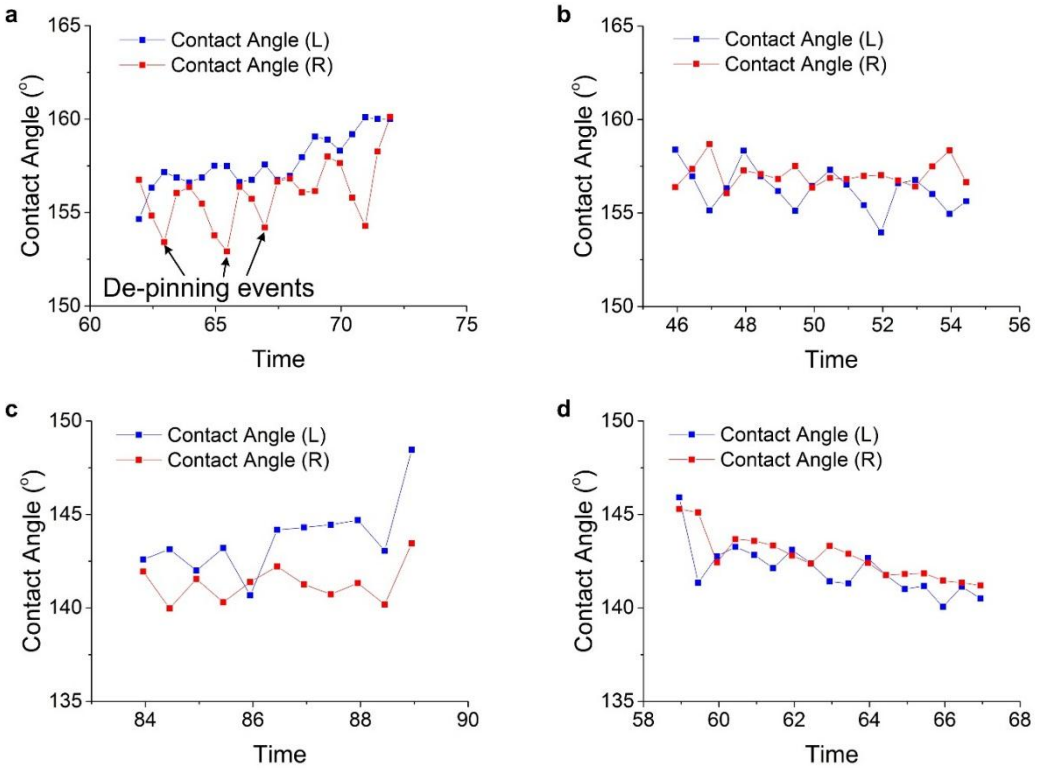

Figure 7.8 Contact angle measurements from droplet scrubbing experiments on various CNT scales. a) Ridge density = 0.375, in RI direction b) Ridge density = 0.375, in RO direction c) Ridge density = 0.1875, in RI direction and d) Ridge density = 0.1875 in RO direction.

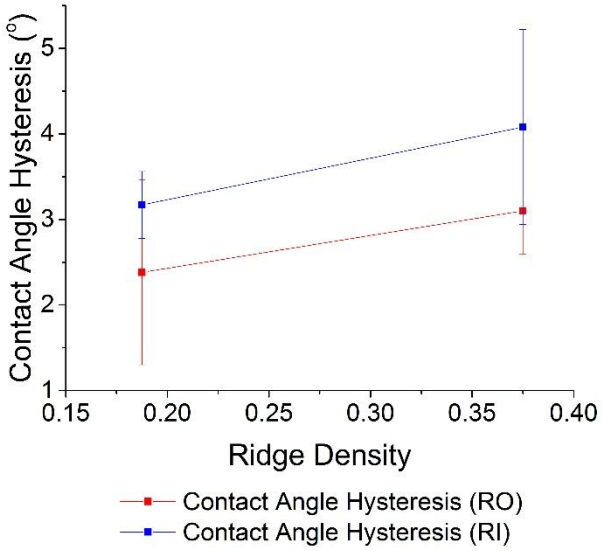

Figure 7.9 Contact angle hysteresis for CNT scales with various ridge densities showing directional wetting behavior.

CHAPTER 8

CONTRIBUTIONS AND OUTLOOK

8.1 Contributions of this thesis

This thesis has demonstrated advances in the following three axes of pursuit:

1. Architecture: The carbon nanotube (CNT) growth process was used to demonstrate complex three-dimensional (3-D) microarchitecture formation

    A. A novel catalyst stack was utilized to tune the growth rate of the CNTs on the same substrate. A parametric study was performed to document and understand the growth of CNTs on the newly developed catalyst stack, noting the effect of reaction conditions on the resulting CNT forest geometry/property.

    B. Strain-engineering principle was invented to utilize strain mismatch to shape the CNT microstructures as they grow. Precisely defined and complexly structured CNT microstructures were designed and fabricated which would be otherwise next-to-impossible to fabricate in a timely manner. (with Michael De Volder and A. John Hart)

    C. Developed a novel modeling scheme and a finite element method (FEM) routine to simulate the growth of strain-engineered CNT microstructures, and understand the stress distribution within the structures and devise strategies to decrease the residual stresses. The model is shown to closely estimate the grown CNT microstructure geometry, with capability of varying and observing the effects of parameters such as the relative

growth rates, catalyst-TiN overlap, structure dimensions and constituent material property on the resulting CNT microstructure geometry.

2. Mechanics: Atomic layer deposition (ALD) was used to precisely tune the mechanics of CNT microstructures with extreme range.

   A. Stiffness of the CNT microstructures were tuned to almost 4 orders of magnitude by varying the coating thickness of Al_2O_3. The stiffness of the CNT-Al_2O_3 composite foam is shown to scale favorably with increasing density with the scaling power of n=2.8. (with Anna Brieland-Schoultz and Sameh Tawfick)

   B. The deformation behavior was tuned from buckling, to brittle fracture and recovery of large strains up to 0.75 was shown. The integrity of the composite structure under multiple compression cycles were shown with little plastic deformation as low as 0.04% per cycle. The underlying mechanism behind large recovery observed was studied.

3. Multifunctionality: CNT microarchitecture fabrication and their subsequent property tuning was used to demonstrate multifunctional metamaterials.

   A. A composite material with high stiffness and damping was designed and fabricated. This composite material is tested to show that it preserves the damping capacity of a specifically engineered polymer while increasing the elastic modulus by a factor of 100. (with Julien Meaud, Trisha Sain and Bongjun Yeom)

   B. A superhydrophic and directionally wetting synthetic surface inspired by butterfly scales was designed and fabricated. The surface was demonstrated to have both superhydrophobicity and directional wetting properties by showing contact angles above 150° and contact angle hysteresis ranging from 2.5-4° in opposite directions. Higher ridge density led to larger contact angle hysteresis. (with Adam Paxson)

The contributions of the thesis has expanded the current design space for microarchitectures on both throughput-structural complexity map (Figure 2.8) and elastic modulus-structure size map (Figure 2.9). As the result of the work described in this dissertation, complex structures can be directly grown (Figure 8.1) and continuous tuning of elastic modulus independent of structure geometry (Figure 8.2) was realized.

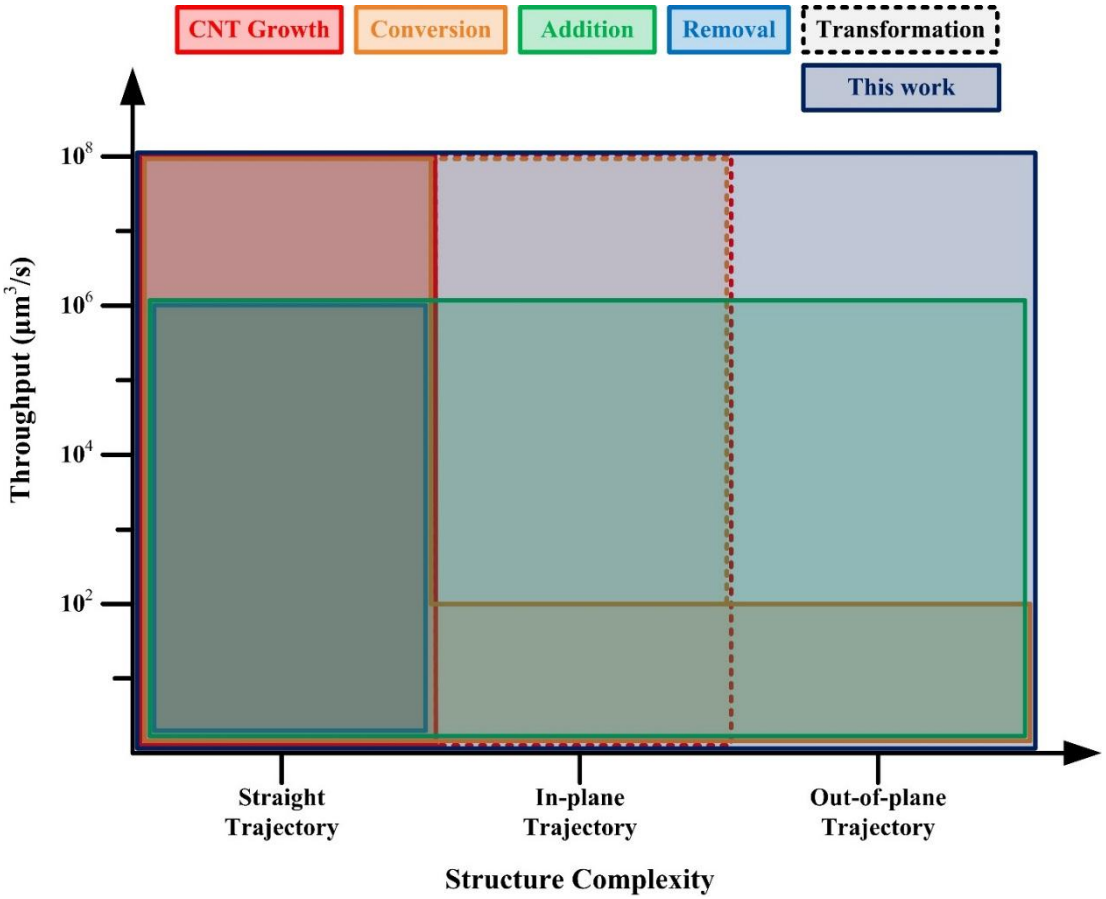

Figure 8.1 Expansion of currently available throughput-structure complexity space afforded by the work described in this dissertation.

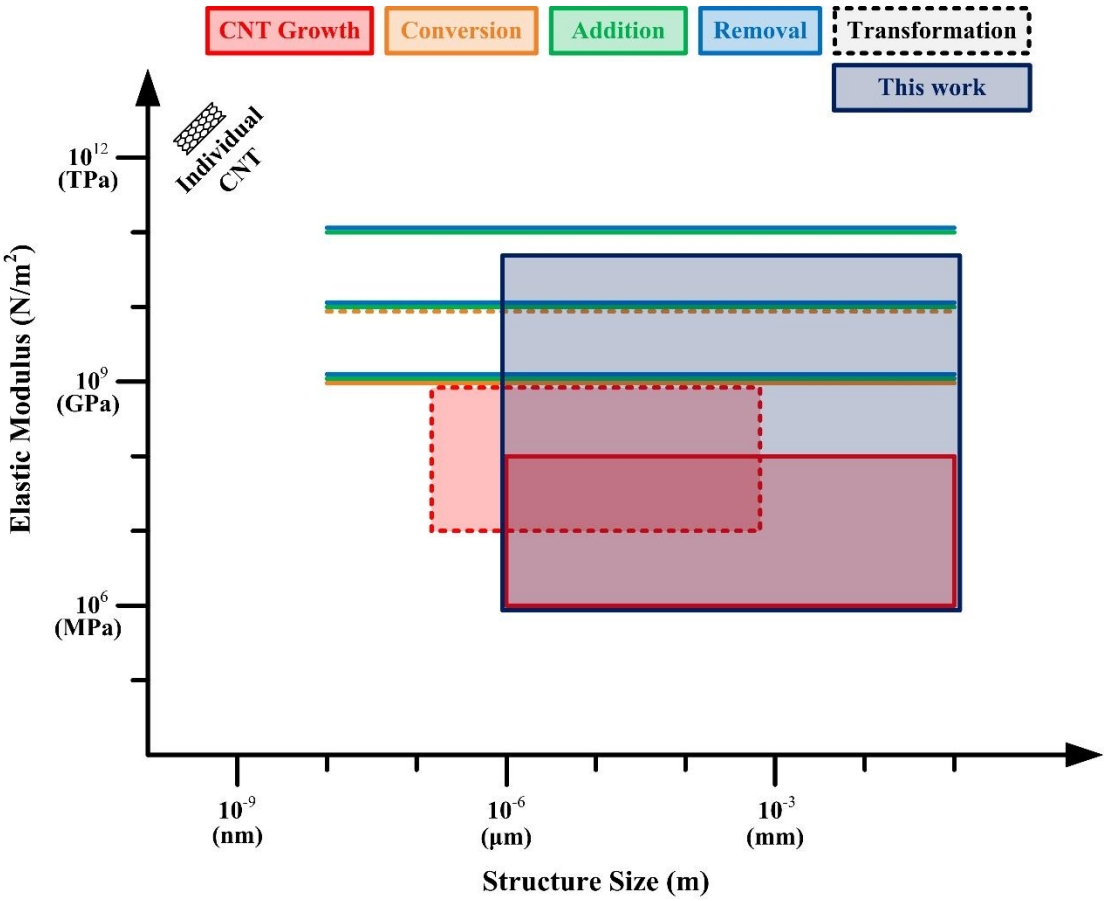

Figure 8.2 Expansion of currently available elastic modulus-structure size space afforded by the work described in this dissertation.

In addition to the work presented in the dissertation, many tangential and complementary directions were pursued in collaboration with other researchers that led to fruitful research outcomes:

1. Study of statistical variation in CNT growth was performed led by Ryan Oliver and Erik Polsen.
2. Visualization of strain evolution in CNT microstructures as they are being compressed axially using Digital Image Correlation was performed led by Matthew Maschmann.
3. Use of ultrafast lasers to machine CNT microstructures was carried out with Aaron Schmidt and Ryan Murphy.

4. Novel sensors and actuators using hydrogel infiltrated arrays of complex 3-D CNT microstructures is being pursued in collaboration with Davor Copic.

5. Nanoscale patterning of CNT catalyst was performed via nanoimprint lithography and CNTs were grown on the nanoscale patterns with Jong G. Ok.

8.2 Outlook

More complex CNT microstructures could be fabricated by modification of the growth recipe. Specifically, the relative growth rates of CNTs on Fe/Al_2O_3 and on $Fe/Al_2O_3/TiN$ are temperature dependent, which opens up opportunities for exploitation in multistep CNT growth at different temperatures, which will result in segmented CNT microstructures with varying curvatures in each segment.

Post processing techniques, such as capillary forming, can be utilized to reduce the dimensions of the fabricated CNT microstructures. With fine control over the application and evaporation of liquid, architectural integrity should not be jeopardized [218]. Capillary forming can be used to shrink the sizes of CNT microstructures (Figure 8.3a and b) and the fine control of pressure and temperature enables precisely controlled liquid application (Figure 8.3c).

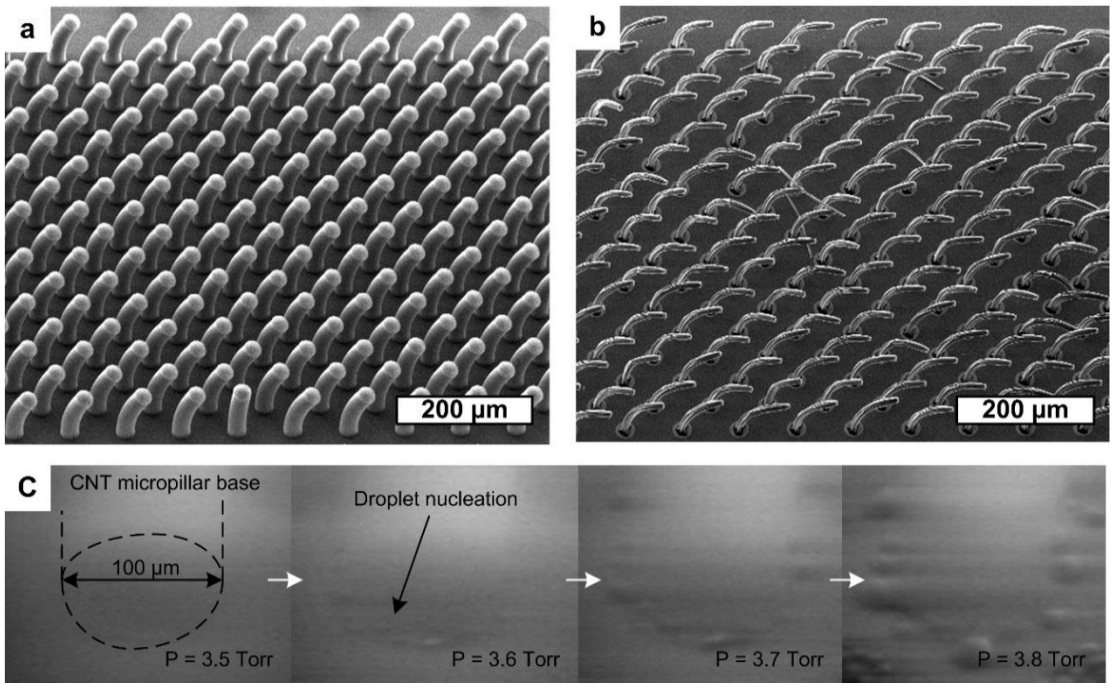

Figure 8.3 Capillary forming as a post processing technique to reduce the dimensions of strain-engineered CNT microarchitectures. a) Strain-engineered CNT microstructures before capillary forming b) Same structures after capillary forming c) *In situ* SEM video snapshots of controlled liquid (water) deposition at the base of CNT micropillars.

Structures with critical dimensions as small as 5 µm (Figure 3.30) were fabricated, and the uniformity of the structures was not sacrificed at this scale. It is expected that smaller 3-D microstructures could be made while still using optical lithography along with high precision alignment of the catalyst and TiN layers. Notably, sub-micrometer vertical CNT features have been fabricated for use as interconnects [219]. One way to achieve a nanoscale patterning is the use of nanoimprint lithography. Pillars and wall patterns with their dimensions down to 110 nm have been fabricated, and CNTs were grown on them (Figure 8.4 and 8.5). Other nanoscale patterning methods, such as interference lithography, is expected to successfully fabricate nanoscale patterns as well.

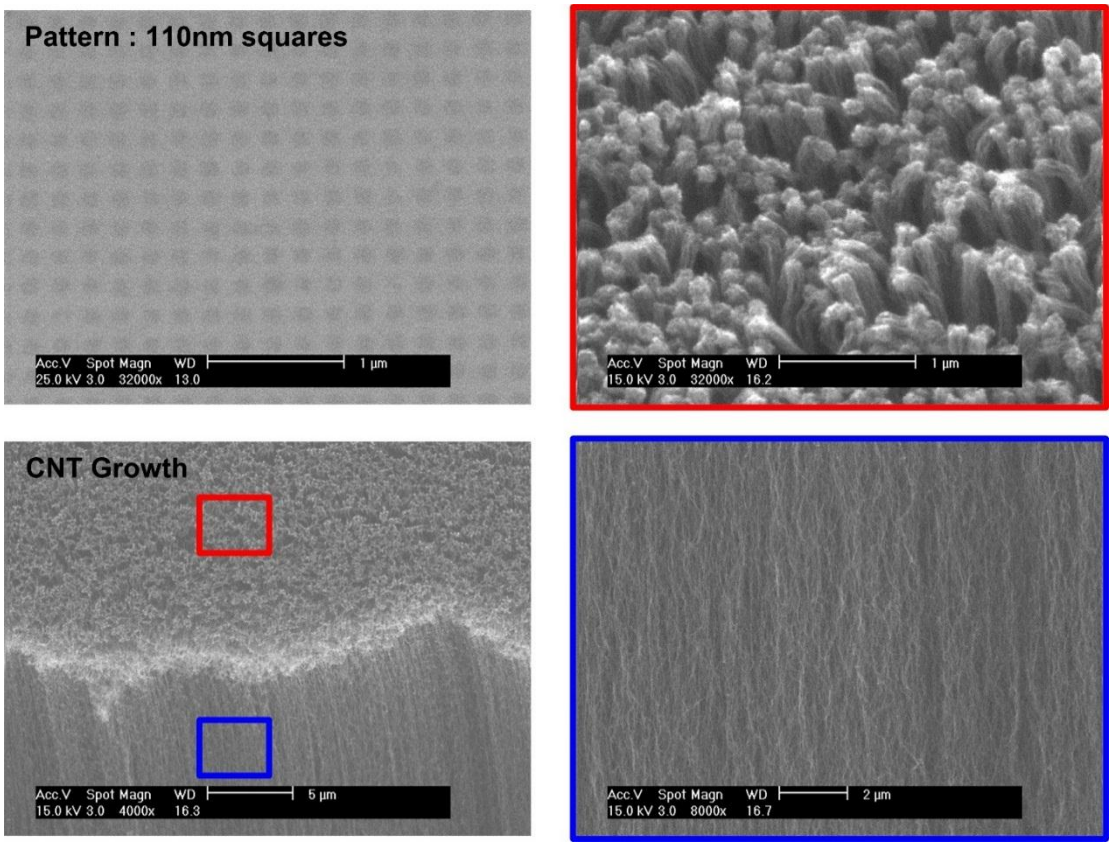

Figure 8.4 CNT nanopillars patterned via nanoimprint lithography.

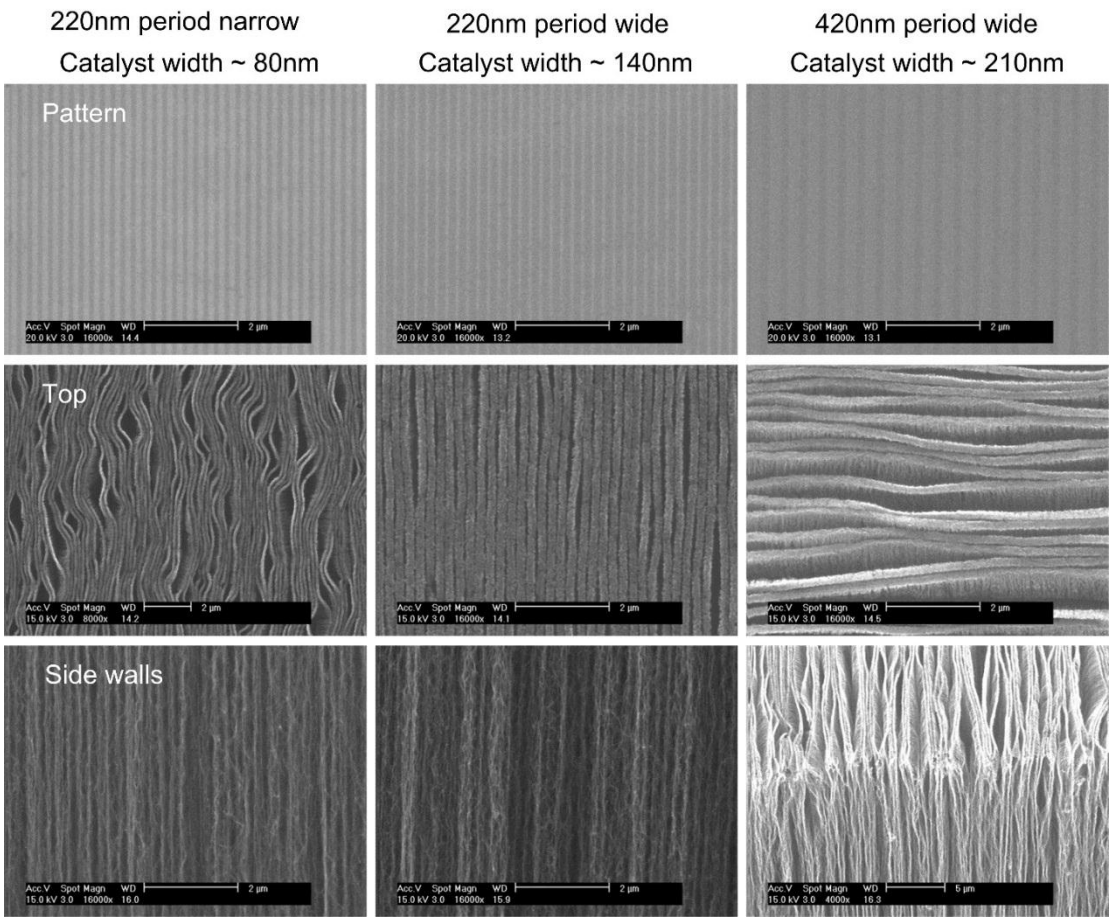

Figure 8.5 CNT nanowalls patterned via nanoimprint lithography.

BIBLIOGRAPHY

1. Fleck, N.A., V.S. Deshpande, and M.F. Ashby, *Micro-architectured materials: past, present and future.* Proceedings of the Royal Society A: Mathematical, Physical and Engineering Science, 2010. **466**(2121): p. 2495-2516.

2. Lee, J.-H., J.P. Singer, and E.L. Thomas, *Micro-/Nanostructured Mechanical Metamaterials.* Advanced Materials, 2012. **24**(36): p. 4782-4810.

3. Reibold, M., et al., *Materials: Carbon nanotubes in an ancient Damascus sabre.* Nature, 2006. **444**(7117): p. 286-286.

4. Qi, M., et al., *A three-dimensional optical photonic crystal with designed point defects.* Nature, 2004. **429**(6991): p. 538-542.

5. Lin, S.Y., et al., *A three-dimensional photonic crystal operating at infrared wavelengths.* Nature, 1998. **394**(6690): p. 251-253.

6. Schaedler, T.A., et al., *Ultralight Metallic Microlattices.* Science, 2011. **334**(6058): p. 962-965.

7. Lee, J.H., et al., *Two-Polymer Microtransfer Molding for Highly Layered Microstructures.* Advanced Materials, 2005. **17**(20): p. 2481-2485.

8. Zhao, X.-M., Y. Xia, and G.M. Whitesides, *Fabrication of three-dimensional micro-structures: Microtransfer molding.* Advanced Materials, 1996. **8**(10): p. 837-840.

9. Brett, M.J. and M.M. Hawkeye, *New Materials at a Glance.* Science, 2008. **319**(5867): p. 1192-1193.

10. Campbell, M., et al., *Fabrication of photonic crystals for the visible spectrum by holographic lithography.* Nature, 2000. **404**(6773): p. 53-56.

11. Duoss, E.B., M. Twardowski, and J.A. Lewis, *Sol-Gel Inks for Direct-Write Assembly of Functional Oxides.* Advanced Materials, 2007. **19**(21): p. 3485-3489.

12. Hayward, R.C., D.A. Saville, and I.A. Aksay, *Electrophoretic assembly of colloidal crystals with optically tunable micropatterns.* Nature, 2000. **404**(6773): p. 56-59.

13. Terrones, M., et al., *Controlled production of aligned-nanotube bundles.* Nature, 1997. **388**(6637): p. 52-55.

14. Fan, S.S., et al., *Self-oriented regular arrays of carbon nanotubes and their field emission properties.* Science, 1999. **283**(5401): p. 512-514.

15. De Volder, M., et al., *Diverse 3-D Microarchitectures Made by Capillary Forming of Carbon Nanotubes.* Advanced Materials, 2010. **22**(39): p. 4384-4389.

16. Pendry, J.B., et al., *Extremely Low Frequency Plasmons in Metallic Mesostructures.* Physical Review Letters, 1996. **76**(25): p. 4773-4776.

17. Pendry, J.B., et al., *Magnetism from conductors and enhanced nonlinear phenomena.* Microwave Theory and Techniques, IEEE Transactions on, 1999. **47**(11): p. 2075-2084.

18. Smith, D.R., et al., *Composite Medium with Simultaneously Negative Permeability and Permittivity.* Physical Review Letters, 2000. **84**(18): p. 4184-4187.

19. Kushwaha, M.S., et al., *Theory of acoustic band structure of periodic elastic composites.* Physical Review B, 1994. **49**(4): p. 2313-2322.

20. Montero de Espinosa, F.R., E. Jiménez, and M. Torres, *Ultrasonic Band Gap in a Periodic Two-Dimensional Composite.* Physical Review Letters, 1998. **80**(6): p. 1208-1211.

21. Sánchez-Pérez, J.V., et al., *Sound Attenuation by a Two-Dimensional Array of Rigid Cylinders.* Physical Review Letters, 1998. **80**(24): p. 5325-5328.

22. Robertson, W.M. and J.F. Rudy, *Measurement of acoustic stop bands in two-dimensional periodic scattering arrays.* The Journal of the Acoustical Society of America, 1998. **104**(2): p. 694-699.

23. Yang, S., et al., *Focusing of Sound in a 3-D Phononic Crystal.* Physical Review Letters, 2004. **93**(2): p. 024301.

24. Liu, Z., et al., *Locally Resonant Sonic Materials.* Science, 2000. **289**(5485): p. 1734-1736.

25. Li, B., L. Wang, and G. Casati, *Thermal Diode: Rectification of Heat Flux.* Physical Review Letters, 2004. **93**(18): p. 184301.

26. Zhang, S., L. Yin, and N. Fang, *Focusing Ultrasound with an Acoustic Metamaterial Network.* Physical Review Letters, 2009. **102**(19): p. 194301.

27. Zhang, S., C. Xia, and N. Fang, *Broadband Acoustic Cloak for Ultrasound Waves.* Physical Review Letters, 2011. **106**(2): p. 024301.

28. Xu, B., et al., *Making Negative Poisson's Ratio Microstructures by Soft Lithography.* Advanced Materials, 1999. **11**(14): p. 1186-1189.

29. Onda, T., et al., *Super-Water-Repellent Fractal Surfaces.* Langmuir, 1996. **12**(9): p. 2125-2127.

30. Wong, T.-S., et al., *Bioinspired self-repairing slippery surfaces with pressure-stable omniphobicity.* Nature, 2011. **477**(7365): p. 443-447.

31. Eichenfield, M., et al., *Optomechanical crystals.* Nature, 2009. **462**(7269): p. 78-82.

32. Tawfick, S., et al., *Engineering of Micro- and Nanostructured Surfaces with Anisotropic Geometries and Properties.* Advanced Materials, 2012. **24**(13): p. 1628-1674.

33. Takahashi, S., et al., *Direct creation of three-dimensional photonic crystals by a top-down approach.* Nat Mater, 2009. **8**(9): p. 721-725.

34. Hui, F., et al., *Fabrication of slantingly-aligned silicon nanowire arrays for solar cell applications.* Nanotechnology, 2008. **19**(25): p. 255703.

35. Hawkeye, M.M. and M.J. Brett, *Glancing angle deposition: Fabrication, properties, and applications of micro- and nanostructured thin films.* Journal of Vacuum Science & Technology A, 2007. **25**(5): p. 1317-1335.

36. Gansel, J.K., et al., *Gold Helix Photonic Metamaterial as Broadband Circular Polarizer.* Science, 2009. **325**(5947): p. 1513-1515.

37. Chu, K.-H., R. Xiao, and E.N. Wang, *Uni-directional liquid spreading on asymmetric nanostructured surfaces.* Nat Mater, 2010. **9**(5): p. 413-417.

38. Pokroy, B., et al., *Self-Organization of a Mesoscale Bristle into Ordered, Hierarchical Helical Assemblies.* Science, 2009. **323**(5911): p. 237-240.

39. Yoon, H., et al., *Adhesion hysteresis of Janus nanopillars fabricated by nanomolding and oblique metal deposition.* Nano Today, 2009. **4**(5): p. 385-392.

40. Kang, S.H., et al., *Meniscus Lithography: Evaporation-Induced Self-Organization of Pillar Arrays into Moire Patterns.* Physical Review Letters, 2011. **107**(17): p. 177802.

41. Tawfick, S., A.J. Hart, and M. De Volder, *Capillary bending of Janus carbon nanotube micropillars.* Nanoscale, 2012. **4**(13): p. 3852-3856.

42. Park, S.J., et al., *Precise control of elastocapillary densification of nanostructures via low-pressure condensation.* Journal of Micromechanics and Microengineering, 2014. **24**(6): p. 065019.

43. Whitesides, G.M. and B. Grzybowski, *Self-Assembly at All Scales.* Science, 2002. **295**(5564): p. 2418-2421.

44. Grzelczak, M., et al., *Directed Self-Assembly of Nanoparticles.* ACS Nano, 2010. **4**(7): p. 3591-3605.

45. Xia, D. and S.R.J. Brueck, *A Facile Approach to Directed Assembly of Patterns of Nanoparticles Using Interference Lithography and Spin Coating.* Nano Letters, 2004. **4**(7): p. 1295-1299.

46. Beroz, J., et al., *Four degree of freedom liquid dispenser for direct write capillary self-assembly with sub-nanoliter precision.* Review of Scientific Instruments, 2012. **83**(1): p. -.

47. Jacobsen, A.J., W. Barvosa-Carter, and S. Nutt, *Micro-scale Truss Structures formed from Self-Propagating Photopolymer Waveguides.* Advanced Materials, 2007. **19**(22): p. 3892-3896.

48. Haske, W., et al., *65 nm feature sizes using visible wavelength 3-D multiphoton lithography.* Optics Express, 2007. **15**(6): p. 3426-3436.

49. Bückmann, T., et al., *Tailored 3-D Mechanical Metamaterials Made by Dip-in Direct-Laser-Writing Optical Lithography.* Advanced Materials, 2012. **24**(20): p. 2710-2714.

50. Burckel, D.B., et al., *Lithographically Defined Porous Carbon Electrodes.* Small, 2009. **5**(24): p. 2792-2796.

51. De Volder, M.F.L., et al., *Hierarchical Carbon Nanowire Microarchitectures Made by Plasma-Assisted Pyrolysis of Photoresist.* ACS Nano, 2011. **5**(8): p. 6593-6600.

52. Hart, A.J. and A.H. Slocum, *Rapid Growth and Flow-Mediated Nucleation of Millimeter-Scale Aligned Carbon Nanotube Structures from a Thin-Film Catalyst.* The Journal of Physical Chemistry B, 2006. **110**(16): p. 8250-8257.

53. Tian, B., et al., *Single-crystalline kinked semiconductor nanowire superstructures.* Nat Nano, 2009. **4**(12): p. 824-829.

54. Bierman, M.J., et al., *Dislocation-Driven Nanowire Growth and Eshelby Twist.* Science, 2008. **320**(5879): p. 1060-1063.

55. Wang, L., et al., *High yield synthesis and lithography of silica-based nanospring mats.* Nanotechnology, 2006. **17**(11): p. S298.

56. Aoki, K., et al., *Microassembly of semiconductor three-dimensional photonic crystals.* Nat Mater, 2003. **2**(2): p. 117-121.

57. Xia, Y., et al., *Replica molding using polymeric materials: A practical step toward nanomanufacturing.* Advanced Materials, 1997. **9**(2): p. 147-149.

58. Copic, D., et al., *Fabrication, Densification, and Replica Molding of 3-D Carbon Nanotube Microstructures.* 2012(65): p. e3980.

59. Chou, S.Y., P.R. Krauss, and P.J. Renstrom, *Imprint of sub-25 nm vias and trenches in polymers.* Applied Physics Letters, 1995. **67**(21): p. 3114-3116.

60. Chou, S.Y., P.R. Krauss, and P.J. Renstrom, *Nanoimprint lithography.* Journal of Vacuum Science & Technology B, 1996. **14**(6): p. 4129-4133.

61. Iijima, S., *Helical Microtubules of Graphitic Carbon.* Nature, 1991. **354**(6348): p. 56-58.

62. Zhao, X., et al., *Smallest Carbon Nanotube Is 3Å in Diameter.* Physical Review Letters, 2004. **92**(12): p. 125502.

63. Guan, L., K. Suenaga, and S. Iijima, *Smallest Carbon Nanotube Assigned with Atomic Resolution Accuracy.* Nano Letters, 2008. **8**(2): p. 459-462.

64. Hayashi, T., et al., *Smallest freestanding single-walled carbon nanotube.* Nano Letters, 2003. **3**(7): p. 887-889.

65. Truong, V., et al. *Multi-walled carbon nanotubes of 200 nm diameter and*

carbon micro-balloons. in *Nanoscience and Nanotechnology (ICONN), 2010 International Conference on*. 2010.

66. Wang, X., et al., *Fabrication of Ultralong and Electrically Uniform Single-Walled Carbon Nanotubes on Clean Substrates.* Nano Letters, 2009. **9**(9): p. 3137-3141.

67. Meshot, E., et al., *Engineering Vertically Aligned Carbon Nanotube Growth by Decoupled Thermal Treatment of Precursor and Catalyst.* ACS NANO, 2009. **3**(9): p. 2477-2486.

68. Treacy, M.M.J., T.W. Ebbesen, and J.M. Gibson, *Exceptionally high Young's modulus observed for individual carbon nanotubes.* Nature, 1996. **381**(6584): p. 678-680.

69. Yakobson, B.I., C.J. Brabec, and J. Bernholc, *Nanomechanics of carbon tubes: Instabilities beyond linear response.* Physical Review Letters, 1996. **76**(14): p. 2511-2514.

70. Byszewski, P., et al., *Fullerene and nanotube synthesis. Plasma spectroscopy studies.* Journal of Physics and Chemistry of Solids, 1997. **58**(11): p. 1679-1683.

71. Ruoff, R.S. and D.C. Lorents, *MECHANICAL AND THERMAL-PROPERTIES OF CARBON NANOTUBES.* Carbon, 1995. **33**(7): p. 925-930.

72. Demczyk, B.G., et al., *Direct mechanical measurement of the tensile strength and elastic modulus of multiwalled carbon nanotubes.* Materials Science and Engineering: A, 2002. **334**(1–2): p. 173-178.

73. Yu, M.-F., et al., *Strength and Breaking Mechanism of Multiwalled Carbon Nanotubes Under Tensile Load.* Science, 2000. **287**(5453): p. 637-640.

74. Ruoff, R.S., et al., *Radial deformation of carbon nanotubes by van der Waals forces.* Nature, 1993. **364**(6437): p. 514-516.

75. Yu, M.-F., T. Kowalewski, and R.S. Ruoff, *Investigation of the Radial Deformability of Individual Carbon Nanotubes under Controlled Indentation Force.* Physical Review Letters, 2000. **85**(7): p. 1456-1459.

76. Palaci, I., et al., *Radial Elasticity of Multiwalled Carbon Nanotubes.* Physical Review Letters, 2005. **94**(17): p. 175502.

77. Minary-Jolandan, M. and M.-F. Yu, *Reversible radial deformation up to the complete flattening of carbon nanotubes in nanoindentation.* Journal of Applied Physics, 2008. **103**(7): p. -.

78. Pop, E., et al., *Thermal Conductance of an Individual Single-Wall Carbon Nanotube above Room Temperature.* Nano Letters, 2005. **6**(1): p. 96-100.

79. Sinha, S., et al., *Off-axis Thermal Properties of Carbon Nanotube Films.* Journal of Nanoparticle Research, 2005. **7**(6): p. 651-657.

80. Blase, X., et al., *Hybridization effects and metallicity in small radius carbon nanotubes.* Physical Review Letters, 1994. **72**(12): p. 1878-1881.

81. Kane, C.L. and E.J. Mele, *Size, Shape, and Low Energy Electronic Structure of Carbon Nanotubes.* Physical Review Letters, 1997. **78**(10): p. 1932-1935.

82. Kleiner, A. and S. Eggert, *Curvature, hybridization, and STM images of carbon nanotubes.* Physical Review B, 2001. **64**(11): p. 113402.

83. Kleiner, A. and S. Eggert, *Band gaps of primary metallic carbon nanotubes.* Physical Review B, 2001. **63**(7): p. 073408.

84. Ouyang, M., et al., *Energy Gaps in "Metallic" Single-Walled Carbon Nanotubes.* Science, 2001. **292**(5517): p. 702-705.

85. Ouyang, M., J.-L. Huang, and C.M. Lieber, *SCANNING TUNNELING MICROSCOPY STUDIES OF THE ONE-DIMENSIONAL ELECTRONIC PROPERTIES OF SINGLE-WALLED CARBON NANOTUBES.* Annual Review of Physical Chemistry, 2002. **53**(1): p. 201-220.

86. Ouyang, M., J.-L. Huang, and C.M. Lieber, *Fundamental Electronic Properties and Applications of Single-Walled Carbon Nanotubes.* Accounts of Chemical Research, 2002. **35**(12): p. 1018-1025.

87. Gülseren, O., T. Yildirim, and S. Ciraci, *Systematic ab initio study of curvature effects in carbon nanotubes.* Physical Review B, 2002. **65**(15): p. 153405.

88. Zólyomi, V. and J. Kürti, *First-principles calculations for the electronic band structures of small diametersingle-wall carbon nanotubes.* Physical Review B, 2004. **70**(8): p. 085403.

89. Hong, S. and S. Myung, *Nanotube electronics - A flexible approach to mobility.* Nature Nanotechnology, 2007. **2**(4): p. 207-208.

90. Tang, Z.K., et al., *Superconductivity in 4 Angstrom Single-Walled Carbon Nanotubes.* Science, 2001. **292**(5526): p. 2462-2465.

91. Takesue, I., et al., *Superconductivity in entirely end-bonded multiwalled carbon nanotubes.* Physical Review Letters, 2006. **96**(5): p. 057001.

92. Lortz, R., et al., *Superconducting characteristics of 4-Å carbon nanotube–zeolite composite.* Proceedings of the National Academy of Sciences, 2009. **106**(18): p. 7299-7303.

93. Mizuno, K., et al., *A black body absorber from vertically aligned single-walled carbon nanotubes.* Proceedings of the National Academy of Sciences, 2009. **106**(15): p. 6044-6047.

94. Yang, Z.-P., et al., *Experimental Observation of an Extremely Dark Material Made By a Low-Density Nanotube Array.* Nano Letters, 2008. **8**(2): p. 446-451.

95. Lu, X. and Z. Chen, *Curved Pi-Conjugation, Aromaticity, and the Related Chemistry of Small Fullerenes (<C60) and Single-Walled Carbon Nanotubes.* Chemical Reviews, 2005. **105**(10): p. 3643-3696.

96. Mickelson, E.T., et al., *Solvation of Fluorinated Single-Wall Carbon Nanotubes in Alcohol Solvents.* The Journal of Physical Chemistry B, 1999. **103**(21): p.

4318-4322.

97. Georgakilas, V., et al., *Purification of HiPCO Carbon Nanotubes via Organic Functionalization.* Journal of the American Chemical Society, 2002. **124**(48): p. 14318-14319.

98. Czerw, R., et al., *Identification of Electron Donor States in N-Doped Carbon Nanotubes.* Nano Letters, 2001. **1**(9): p. 457-460.

99. Terrones, M., et al., *N-doping and coalescence of carbon nanotubes: synthesis and electronic properties.* Applied Physics A, 2002. **74**(3): p. 355-361.

100. Ren, Z.F., et al., *Synthesis of Large Arrays of Well-Aligned Carbon Nanotubes on Glass.* Science, 1998. **282**(5391): p. 1105-1107.

101. Wirth, C.T., et al., *Diffusion- and Reaction-Limited Growth of Carbon Nanotube Forests.* ACS Nano, 2009. **3**(11): p. 3560-3566.

102. Sugime, H., et al., *Low temperature growth of ultra-high mass density carbon nanotube forests on conductive supports.* Applied Physics Letters, 2013. **103**(7): p. -.

103. Cao, A.Y., et al., *Super-compressible foamlike carbon nanotube films.* Science, 2005. **310**(5752): p. 1307-1310.

104. Yaglioglu, O., et al., *Wide Range Control of Microstructure and Mechanical Properties of Carbon Nanotube Forests: A Comparison Between Fixed and Floating Catalyst CVD Techniques.* Advanced Functional Materials, 2012. **22**(23): p. 5028-5037.

105. Prasher, R.S., et al., *Turning Carbon Nanotubes from Exceptional Heat Conductors into Insulators.* Physical Review Letters, 2009. **102**(Copyright (C) 2010 The American Physical Society): p. 105901.

106. Coleman, J.N., et al., *Small but strong: A review of the mechanical properties of carbon nanotube–polymer composites.* Carbon, 2006. **44**(9): p. 1624-1652.

107. Nirmalraj, P.N., et al., *Electrical Connectivity in Single-Walled Carbon Nanotube Networks.* Nano Letters, 2009. **9**(11): p. 3890-3895.

108. Martyniuk, M., et al., *Stress in low-temperature plasma enhanced chemical vapour deposited silicon nitride thin films.* Smart Materials and Structures, 2006. **15**(1): p. S29.

109. Schweizer, S., et al., *Thermally actuated optical microscanner with large angle and low consumption.* Sensors and Actuators, A: Physical, 1999. **76**(1-3): p. 470-477.

110. Chang, C. and P. Chang, *Innovative micromachined microwave switch with very low insertion loss.* Sensors and Actuators, A: Physical, 2000. **79**(1): p. 71-75.

111. Kim, S.-H., J.G. Boyd, and S. Mani, *Mechanical behavior of mismatch strain-driven microcantilever.* Microelectronics Journal, 2007. **38**(3): p. 371-380.

112. Chalapat, K., et al., *Self-Organized Origami Structures via Ion-Induced Plastic*

Strain. Advanced Materials, 2013. **25**(1): p. 91-95.

113. Sam, E.D., et al., *Simultaneous growth of self-patterned carbon nanotube forests with dual height scales.* Nanoscale, 2012. **4**(12): p. 3746-3753.

114. Bedewy, M., B. Farmer, and A.J. Hart, *Synergetic Chemical Coupling Controls the Uniformity of Carbon Nanotube Microstructure Growth.* Acs Nano, 2014. **8**(6): p. 5799-5812.

115. Meshot, E.R., et al., *Engineering Vertically Aligned Carbon Nanotube Growth by Decoupled Thermal Treatment of Precursor and Catalyst.* Acs Nano, 2009. **3**(9): p. 2477-2486.

116. Bedewy, M., et al., *Population Growth Dynamics of Carbon Nanotubes.* ACS Nano, 2011. **5**(11): p. 8974-8989.

117. Wang, B.N., et al., *Quantitative characterization of the morphology of multiwall carbon nanotube films by small-angle X-ray scattering.* Journal of Physical Chemistry C, 2007. **111**(16): p. 5859-5865.

118. Xu, M., et al., *Alignment Control of Carbon Nanotube Forest from Random to Nearly Perfectly Aligned by Utilizing the Crowding Effect.* ACS Nano, 2012. **6**(7): p. 5837-5844.

119. Stone, A.J. and D.J. Wales, *Theoretical studies of icosahedral C60 and some related species.* Chemical Physics Letters, 1986. **128**(5–6): p. 501-503.

120. Jorio, A., et al., *Characterizing carbon nanotube samples with resonance Raman scattering.* New Journal of Physics, 2003. **5**(1): p. 139.

121. Pimenta, M.A., et al., *Studying disorder in graphite-based systems by Raman spectroscopy.* Physical Chemistry Chemical Physics, 2007. **9**(11): p. 1276-1290.

122. Dresselhaus, M.S., A. Jorio, and R. Saito, *Characterizing Graphene, Graphite, and Carbon Nanotubes by Raman Spectroscopy.* Annual Review of Condensed Matter Physics, 2010. **1**(1): p. 89-108.

123. Mingo, N., et al., *Phonon transmission through defects in carbon nanotubes from first principles.* Physical Review B, 2008. **77**(3): p. 033418.

124. Fan, Y., B.R. Goldsmith, and P.G. Collins, *Identifying and counting point defects in carbon nanotubes.* Nat Mater, 2005. **4**(12): p. 906-911.

125. Picher, M., et al., *Influence of the growth conditions on the defect density of single-walled carbon nanotubes.* Carbon, 2012. **50**(7): p. 2407-2416.

126. Meshot, E.R., et al., *High-Speed in Situ X-ray Scattering of Carbon Nanotube Film Nucleation and Self-Organization.* ACS Nano, 2012. **6**(6): p. 5091-5101.

127. Kukovitsky, E.F., et al., *Correlation between metal catalyst particle size and carbon nanotube growth.* Chemical Physics Letters, 2002. **355**(5–6): p. 497-503.

128. Nerushev, O.A., et al., *Particle size dependence and model for iron-catalyzed growth of carbon nanotubes by thermal chemical vapor deposition.* Journal of Applied Physics, 2003. **93**(7): p. 4185-4190.

129. Wang, Y., et al., *Comparison study of catalyst nanoparticle formation and carbon nanotube growth: Support effect.* Journal of Applied Physics, 2007. **101**(12): p. -.

130. Liao, X.Z., et al., *Effect of catalyst composition on carbon nanotube growth.* Applied Physics Letters, 2003. **82**(16): p. 2694-2696.

131. Kpetsu, J.-B., et al., *Influence of Ni Catalyst Layer and TiN Diffusion Barrier on Carbon Nanotube Growth Rate.* Nanoscale Research Letters, 2010. **5**(3): p. 539 - 544.

132. de los Arcos, T., et al., *The Influence of Catalyst Chemical State and Morphology on Carbon Nanotube Growth.* The Journal of Physical Chemistry B, 2004. **108**(23): p. 7728-7734.

133. Bedewy, M., E.R. Meshot, and A.J. Hart, *Diameter-dependent kinetics of activation and deactivation in carbon nanotube population growth.* Carbon, 2012. **50**(14): p. 5106-5116.

134. Kim, S.M., et al., *Evolution in Catalyst Morphology Leads to Carbon Nanotube Growth Termination.* Journal of Physical Chemistry Letters, 2010. **1**(6): p. 918-922.

135. Park, S.J., et al., *Measurement of carbon nanotube microstructure relative density by optical attenuation and observation of size-dependent variations.* Physical Chemistry Chemical Physics, 2013. **15**(27): p. 11511-11519.

136. Maschmann, M.R., et al., *Continuum analysis of carbon nanotube array buckling enabled by anisotropic elastic measurements and modeling.* Carbon, 2014. **66**(0): p. 377-386.

137. Gao, Y., et al., *Impact of nanotube density and alignment on the elastic modulus near the top and base surfaces of aligned multi-walled carbon nanotube films.* Carbon, 2012. **50**(10): p. 3789-3798.

138. Tong, T., et al., *Height independent compressive modulus of vertically aligned carbon nanotube arrays.* Nano Letters, 2008. **8**(2): p. 511-515.

139. Ge, L., et al., *Cooperative Adhesion and Friction of Compliant Nanohairs.* Nano Letters, 2010. **10**(11): p. 4509-4513.

140. Timoshenko, S., *Analysis of bi-metal thermostats.* J. Opt. Soc. Am., 1925. **11**(3): p. 233-255.

141. Maschmann, M.R., et al., *Continuum analysis of carbon nanotube array buckling enabled by anisotropic elastic measurements and modeling.* Carbon, 2014. **66**: p. 377-386.

142. Bao, Q., H. Zhang, and C. Pan, *Simulation for growth of multi-walled carbon nanotubes in electric field.* Computational Materials Science, 2007. **39**(3): p. 616-626.

143. Belytschko, T. and T. Black, *Elastic crack growth in finite elements with minimal remeshing.* International Journal for Numerical Methods in

Engineering, 1999. **45**(5): p. 601-620.

144. Cox, B. and Q. Yang, *In Quest of Virtual Tests for Structural Composites.* Science, 2006. **314**(5802): p. 1102-1107.

145. Fayant, P., et al., *Finite Element Model of Polar Growth in Pollen Tubes.* The Plant Cell Online, 2010. **22**(8): p. 2579-2593.

146. Maschmann, M.R., et al., *Visualizing Strain Evolution and Coordinated Buckling within CNT Arrays by In Situ Digital Image Correlation.* Advanced Functional Materials, 2012. **22**(22).

147. Deck, C.P., et al., *Mechanical behavior of ultralong multiwalled carbon nanotube mats.* Journal of Applied Physics, 2007. **101**(2): p. 023512.

148. Tawfick, S., et al., *Mechanics of Capillary Forming of Aligned Carbon Nanotube Assemblies.* Langmuir, 2013. **29**(17): p. 5190-5198.

149. Won, Y., et al., *Zipping, entanglement, and the elastic modulus of aligned single-walled carbon nanotube films.* Proceedings of the National Academy of Sciences, 2013. **110**(51): p. 20426-20430.

150. Hall, L.J., et al., *Sign change of Poisson's ratio for carbon nanotube sheets.* Science, 2008. **320**(5875): p. 504-507.

151. Futaba, D.N., et al., *Shape-engineerable and highly densely packed single-walled carbon nanotubes and their application as super-capacitor electrodes.* Nature Materials, 2006. **5**(12): p. 987-994.

152. Puurunen, R.L., *Surface chemistry of atomic layer deposition: A case study for the trimethylaluminum/water process.* Journal of Applied Physics, 2005. **97**(12): p. -.

153. Devine, C.K., et al., *Fiber Containment for Improved Laboratory Handling and Uniform Nanocoating of Milligram Quantities of Carbon Nanotubes by Atomic Layer Deposition.* Langmuir, 2011. **27**(23): p. 14497-14507.

154. George, S.M., *Atomic Layer Deposition: An Overview.* Chemical Reviews, 2009. **110**(1): p. 111-131.

155. Farmer, D.B. and R.G. Gordon, *Atomic Layer Deposition on Suspended Single-Walled Carbon Nanotubes via Gas-Phase Noncovalent Functionalization.* Nano Letters, 2006. **6**(4): p. 699-703.

156. Farmer, D.B. and R.G. Gordon, *ALD of High- κ Dielectrics on Suspended Functionalized SWNTs.* Electrochemical and Solid-State Letters, 2005. **8**(4): p. G89-G91.

157. Cavanagh, A.S., et al., *Atomic layer deposition on gram quantities of multi-walled carbon nanotubes.* Nanotechnology, 2009. **20**(25): p. 255602.

158. Bedewy, M., et al., *Collective Mechanism for the Evolution and Self-Termination of Vertically Aligned Carbon Nanotube Growth.* Journal of Physical Chemistry C, 2009. **113**(48): p. 20576-20582.

159. Worsley, M.A., et al., *Mechanically robust and electrically conductive carbon nanotube foams.* Applied Physics Letters, 2009. **94**(7).

160. Andrews, E., W. Sanders, and L.J. Gibson, *Compressive and tensile behaviour of aluminum foams.* Materials Science and Engineering: A, 1999. **270**(2): p. 113-124.

161. Cebeci, H., et al., *Multifunctional properties of high volume fraction aligned carbon nanotube polymer composites with controlled morphology.* Composites Science and Technology, 2009. **69**(15-16): p. 2649-2656.

162. Gibson, L.J. and M.F. Ashby, *The Mechanics of Three-Dimensional Cellular Materials.* Proceedings of the Royal Society, 1982. **382**(1782): p. 43-59.

163. *Hexweb Honeycomb Attributes and Properties*, in *http://www.hexcel.com/Resources/DataSheets/Brochure-Data-Sheets/Honeycomb_Attributes_and_Properties.pdf*.

164. Zou, J., et al., *Ultralight Multiwalled Carbon Nanotube Aerogel.* Acs Nano, 2010. **4**(12).

165. Tillotson, T.M. and L.W. Hrubesh, *TRANSPARENT ULTRALOW-DENSITY SILICA AEROGELS PREPARED BY A 2-STEP SOL-GEL PROCESS.* Journal of Non-Crystalline Solids, 1992. **145**(1-3).

166. Schaedler, T.A., et al., *Ultralight Metallic Microlattices.* Science, 2011. **334**(6058).

167. Gibson, L.J. and M.F. Ashby, *Cellular Solids*1999: Cambridge University Press. 510.

168. Garcia, E.J., B.L. Wardle, and A. John Hart, *Joining prepreg composite interfaces with aligned carbon nanotubes.* Composites Part A: Applied Science and Manufacturing, 2008. **39**(6): p. 1065-1070.

169. Abadi, P.P.S.S., et al., *Deformation response of conformally coated carbon nanotube forests.* Nanotechnology, 2013. **24**(47): p. 475707.

170. Krishnan, A., et al., *Young's modulus of single-walled nanotubes.* Physical Review B, 1998. **58**(20): p. 14013-14019.

171. Xie, S., et al., *Mechanical and physical properties on carbon nanotube.* Journal of Physics and Chemistry of Solids, 2000. **61**(7): p. 1153-1158.

172. Hill, F.A., et al., *Storing elastic energy in carbon nanotubes.* Journal of Micromechanics and Microengineering, 2009. **19**(9).

173. Chang, C.-C., et al., *A New Lower Limit for the Ultimate Breaking Strain of Carbon Nanotubes.* Acs Nano, 2010. **4**(9): p. 5095-5100.

174. Falvo, M.R., et al., *Bending and buckling of carbon nanotubes under large strain.* Nature, 1997. **389**(6651): p. 582-584.

175. Zhao, Q., M.B. Nardelli, and J. Bernholc, *Ultimate strength of carbon nanotubes: A theoretical study.* Physical Review B, 2002. **65**(14): p. 144105.

176. Brodt, M. and R.S. Lakes, *Composite Materials Which Exhibit High Stiffness and High Viscoelastic Damping.* Journal of Composite Materials, 1995. **29**(14): p. 1823-1833.

177. Lakes, R., *Materials with structural hierarchy.* Nature, 1993. **361**(6412): p. 511-515.

178. Tai, K., et al., *Nanoscale heterogeneity promotes energy dissipation in bone.* Nat Mater, 2007. **6**(6): p. 454-462.

179. White, A.A., S.M. Best, and I.A. Kinloch, *Hydroxyapatite–Carbon Nanotube Composites for Biomedical Applications: A Review.* International Journal of Applied Ceramic Technology, 2007. **4**(1): p. 1-13.

180. Lakes, R.S., *High Damping Composite Materials: Effect of Structural Hierarchy.* Journal of Composite Materials, 2002. **36**(3): p. 287-297.

181. Breuer, O. and U. Sundararaj, *Big returns from small fibers: A review of polymer/carbon nanotube composites.* Polymer Composites, 2004. **25**(6): p. 630-645.

182. Van Lier, G., et al., *Ab initio study of the elastic properties of single-walled carbon nanotubes and graphene.* Chemical Physics Letters, 2000. **326**(1–2): p. 181-185.

183. Manevitch, O.L. and G.C. Rutledge, *Elastic Properties of a Single Lamella of Montmorillonite by Molecular Dynamics Simulation.* The Journal of Physical Chemistry B, 2003. **108**(4): p. 1428-1435.

184. Šturcová, A., G.R. Davies, and S.J. Eichhorn, *Elastic Modulus and Stress-Transfer Properties of Tunicate Cellulose Whiskers.* Biomacromolecules, 2005. **6**(2): p. 1055-1061.

185. Sigmund, O., *Tailoring materials with prescribed elastic properties.* Mechanics of Materials, 1995. **20**(4): p. 351-368.

186. Sigmund, O., *A new class of extremal composites.* Journal of the Mechanics and Physics of Solids, 2000. **48**(2): p. 397-428.

187. Chen, C.P. and R.S. Lakes, *Analysis of high-loss viscoelastic composites.* Journal of Materials Science, 1993. **28**(16): p. 4299-4304.

188. Chen, C.P. and R.S. Lakes, *Viscoelastic behaviour of composite materials with conventional- or negative-Poisson's-ratio foam as one phase.* Journal of Materials Science, 1993. **28**(16): p. 4288-4298.

189. Gibiansky, L.V. and R. Lakes, *Bounds on the complex bulk and shear moduli of a two-dimensional two-phase viscoelastic composite.* Mechanics of Materials, 1997. **25**(2): p. 79-95.

190. Meaud, J., et al., *Analysis and optimal design of layered composites with high stiffness and high damping.* International Journal of Solids and Structures, 2013. **50**(9): p. 1342-1353.

191. Lakes, R.S., et al., *Extreme damping in composite materials with negative-stiffness inclusions.* Nature, 2001. **410**(6828): p. 565-567.

192. Liu, L., Y. Zhou, and S. Pan, *Experimental and analysis of the mechanical behaviors of multi-walled nanotubes/polyurethane nanoweb-reinforced epoxy composites.* Journal of Reinforced Plastics and Composites, 2013. **32**(11): p. 823-834.

193. Carey, B.J., et al., *Foam-Like Behavior in Compliant, Continuously Reinforced Nanocomposites.* Advanced Functional Materials, 2013. **23**(23): p. 3002-3007.

194. Podsiadlo, P., et al., *Ultrastrong and Stiff Layered Polymer Nanocomposites.* Science, 2007. **318**(5847): p. 80-83.

195. Martz, E.O., R.S. Lakes, and J.B. Park, *Hysteresis behaviour and specific damping capacity of negative Poisson's ratio foams.* Cellular polymers, 1996. **15**(5): p. 349-364.

196. Wenzel, R.N., *Resistance of solid surfaces to wetting by water.* Industrial & Engineering Chemistry, 1936. **28**(8): p. 988-994.

197. Cassie, A.B.D. and S. Baxter, *Wettability of porous surfaces.* Transactions of the Faraday Society, 1944. **40**(0): p. 546-551.

198. Bico, J., U. Thiele, and D. Quéré, *Wetting of textured surfaces.* Colloids and Surfaces A: Physicochemical and Engineering Aspects, 2002. **206**(1–3): p. 41-46.

199. Lafuma, A. and D. Quere, *Superhydrophobic states.* Nat Mater, 2003. **2**(7): p. 457-460.

200. Liu, K. and L. Jiang, *Bio-inspired design of multiscale structures for function integration.* Nano Today, 2011. **6**(2): p. 155-175.

201. Wagner, T., C. Neinhuis, and W. Barthlott, *Wettability and Contaminability of Insect Wings as a Function of Their Surface Sculptures.* Acta Zoologica, 1996. **77**(3): p. 213-225.

202. Barthlott, W. and C. Neinhuis, *Purity of the sacred lotus, or escape from contamination in biological surfaces.* Planta, 1997. **202**(1): p. 1-8.

203. Sun, T., et al., *Bioinspired Surfaces with Special Wettability.* Accounts of Chemical Research, 2005. **38**(8): p. 644-652.

204. Hansen, W.R. and K. Autumn, *Evidence for self-cleaning in gecko setae.* Proceedings of the National Academy of Sciences of the United States of America, 2005. **102**(2): p. 385-389.

205. Feng, L., et al., *Petal Effect: A Superhydrophobic State with High Adhesive Force.* Langmuir, 2008. **24**(8): p. 4114-4119.

206. Liu, M., et al., *Bioinspired Design of a Superoleophobic and Low Adhesive Water/Solid Interface.* Advanced Materials, 2009. **21**(6): p. 665-669.

207. Chang, F.-M., et al., *High contact angle hysteresis of superhydrophobic surfaces:*

Hydrophobic defects. Applied Physics Letters, 2009. **95**(6): p. -.

208. Dean, B. and B. Bhushan, *Shark-skin surfaces for fluid-drag reduction in turbulent flow: a review.* Philosophical Transactions of the Royal Society A: Mathematical, Physical and Engineering Sciences, 2010. **368**(1929): p. 4775-4806.

209. Barthlott, W., et al., *The Salvinia Paradox: Superhydrophobic Surfaces with Hydrophilic Pins for Air Retention Under Water.* Advanced Materials, 2010. **22**(21): p. 2325-2328.

210. Zheng, Y., X. Gao, and L. Jiang, *Directional adhesion of superhydrophobic butterfly wings.* Soft Matter, 2007. **3**(2): p. 178-182.

211. Bhushan, B. and E.K. Her, *Fabrication of Superhydrophobic Surfaces with High and Low Adhesion Inspired from Rose Petal.* Langmuir, 2010. **26**(11): p. 8207-8217.

212. Bixler, G.D. and B. Bhushan, *Bioinspired rice leaf and butterfly wing surface structures combining shark skin and lotus effects.* Soft Matter, 2012. **8**(44): p. 11271-11284.

213. Guo, P., et al., *Generation of hierarchical micro-structures for anisotropic wetting by elliptical vibration cutting.* CIRP Annals - Manufacturing Technology, 2014(0).

214. Malvadkar, N.A., et al., *An engineered anisotropic nanofilm with unidirectional wetting properties.* Nat Mater, 2010. **9**(12): p. 1023-1028.

215. Liu, H., J. Zhai, and L. Jiang, *Wetting and anti-wetting on aligned carbon nanotube films.* Soft Matter, 2006. **2**(10): p. 811-821.

216. Budynas, R.G. and K.J. Nisbett, *Shigley's Mechanical Engineering Design*. 9 ed2010: McGraw-Hill

217. Paxson, A.T. and K.K. Varanasi, *Self-similarity of contact line depinning from textured surfaces.* Nat Commun, 2013. **4**: p. 1492.

218. Park, S., et al., *Precise Control of Elastocapillary Densification of nanostructures via Low-Pressure Condensation.* Journal of Micromechanics and Microengineering, 2014. **24**.

219. Chiodarelli, N., et al., *Integration and electrical characterization of carbon nanotube via interconnects.* Microelectronic Engineering, 2011. **88**(5): p. 837-843.